

**Università degli Studi di Napoli “Federico II”
SCUOLA POLITECNICA E DELLE SCIENZE DI BASE**

**DEPARTMENT OF INDUSTRIAL ENGINEERING
Aerospace Sector**

**PhD Dissertation
XXIX Course**

**Synthetic Jet Actuators
for Flow Control**

Matteo Chiatto

Supervisors:

Luigi de Luca

Olivier Chazot

Roberto Verzicco

Coordinator:

Michele Grassi

April 2017

Contact information:

Matteo Chiatto

Università degli Studi di Napoli “Federico II”

Department of Industrial Engineering

P.le Tecchio 80, 80125, Naples

Italy

email: matteo.chiatto@unina.it

Abstract

Among the various active flow control techniques, Synthetic Jet (SJ) actuators represent a very promising technology due to their short response time, high jet velocity and absence of traditional piping, that matches the requirements of reduced size and low weight. Therefore, understanding in depth the basic physical aspects driving the operation of these actuators is a key point. A practical tool, employed for design and manufacturing purposes, consists in the definition of a low-order model, lumped element model (LEM), which is able to predict the dynamic response of the actuator in a relatively quick way and with reasonable fidelity and accuracy.

The research activity focused by the present author has tried to tackle different aspects to achieve various goals. A major task has concerned the development of LEMs to predict the behavior of two types of actuators: piezo-driven SJ and Plasma Synthetic Jet (PSJ) actuators. These models share the same philosophy: they represent valuable tools useful not only for design purposes, but also to obtain useful insights on the devices performances. A second crucial task has consisted in the design, manufacturing and characterization of various prototypes, which have been used to validate LEMs results. As an additional task of the research activity, applications both in automotive and aerospace fields have been considered.

As regards the piezo-driven synthetic jets, the main activity was concerned with the extension of an already available lumped-element model in order to: derive a non-dimensional form of the governing equations; identify the main design quantities; estimate the device performances; shed light on the actuator energy efficiency with reference to the different stages involved in the operation process. Several issues have been faced including the tech-

nology required for bonding the piezo-element over the metallic shim (so as to realize the so-called diaphragm), the design and manufacturing of the experimental mock-up, the production of the different parts of the device, the post-processing analysis. A very interesting application of the piezo-driven SJ technology, which can have outcomes in the automotive sector, has regarded the manipulation of a continuous water spray. Experimental data, taken within a chamber test rig at two injection pressures, for different SJ positions, have been acquired. Starting from the flow field velocity distributions, detected with Particle Image Velocimetry (PIV), the effective influence region of the jet on the spray has been computed through a T-Test algorithm and corroborated by a vorticity analysis.

Another innovative LEM, able to predict the temporal evolution of the main fluid-dynamic variables involved, has been developed for PSJ actuators. It is fully based on the gasdynamics equations, it includes viscous losses as well as radiative and convective heat transfer mechanisms at walls, and it considers real gas effect for air. OpenFOAM numerical computations have been carried out to perform a first calibration of the lumped model through the determination of key fitting parameters. Results for both single pulse mode and repetitive working regimes have been analyzed, providing insights on the major actuation characteristics. To validate the LEM model, a home-made PSJ actuator has been designed and manufactured. The overall experimental mock-up has been also designed, together with the control electrical system. Experimental measurements of the jet velocity, obtained with Hot-wire anemometer and Pitot tube, have completed the actuator characterization and have allowed the model validation.

To Margherita

Contents

Abstract	iii
List of Figures	xi
List of Tables	xix
1 Introduction	1
1.1 Flow control	1
1.2 Classification	3
1.3 Actuator types	4
1.4 Thesis layout	10
I Piezo-driven Synthetic Jet Actuators	13
2 Piezo-driven synthetic jet actuators: LEM	15
2.1 Introduction	15
2.2 Lumped Element Models	19
2.2.1 Fluid dynamic LEM	20
2.2.2 Analytical stationary solution	28
2.2.3 Transduction approach	34
2.3 Dimensionless equations	38
2.4 Comparison of LEM results	40
3 Piezo-driven synthetic jet actuators: performances	49
3.1 Performances	49
3.1.1 Effect of coupling of the oscillators	49

3.1.2	Effect of the voltage	57
3.1.3	Effect of the orifice length	59
3.2	Efficiency of piezo-driven devices	61
4	Influence of a piezo-driven SJ on a water spray behavior	71
4.1	Introduction	71
4.2	Experimental Apparatus and Procedure	73
4.2.1	Experimental mock-up	73
4.2.2	Synthetic jet actuator	75
4.2.3	Statistical analysis	78
4.3	Results and Discussion	79
4.3.1	Spray velocity field	80
4.3.2	Vorticity analysis	85
	List of Symbols	93
II	Plasma Synthetic Jet Actuators	97
5	Plasma synthetic jet actuators	99
5.1	Introduction	99
5.2	Physical model	101
5.2.1	Energy deposition	102
5.2.2	Discharge and Refresh phases	104
5.3	LEM Results	107
5.3.1	Multidimensional CFD Simulation Set-up	107
5.3.2	LEM calibration and analysis of single cycle	109
5.3.3	Analysis of periodic behavior	111
5.3.4	Frequency response	113
5.4	Comparison with literature models	114
5.4.1	Comparison with Zong's work	114
5.4.2	Comparison with Sary's work	117
6	PSJ experimental characterization	121
6.1	PSJ actuator	121
6.1.1	House-made PSJ actuator	122

6.1.2	Power supply system	123
6.1.3	Operating Cycle	124
6.2	Experimental measurements	127
6.2.1	Pitot tube	127
6.2.2	Hot-wire Anemometer	129
6.2.3	Tuning of the lumped model	132
	List of Symbols	137
7	Conclusions and future work	139
	Appendices	143
A	PSJ governing equations	145
B	Technical drawings	147
	References	151
	Acknowledgments	163

List of Figures

1.1	Interrelation between flow control goals, reprinted from [2].	2
1.2	A classification of different flow-control approaches, reprinted from [6].	5
2.1	Typical synthetic jet device driven by a piezoelectric element. left) top view with orifice; right) bottom view with metallic shim and piezodisk.	16
2.2	Phase-averaged flow field with saddle point (white spot) generated by a SJ actuator, reprinted from [37].	17
2.3	Sketch of a typical synthetic jet device driven by a piezoelectric element.	21
2.4	Aluminum shim diaphragm deflections detected by laser vibrometer. a) fundamental mode (0,1) for actuation frequency $f = 1555$ Hz; b) mode (2,2) for $f = 5370$ Hz. Applied voltage is $V_{ac} = 6$ V.	22
2.5	Plan view of SJ response as a function of the dimensionless chamber height H/d_o for fixed orifice length and voltage. Reprinted from [59].	26
2.6	Forced damped spring-mass schematic of SJ actuator.	29
2.7	Amplification factor of jet peak velocity for decoupled oscillators ($CF = 0$) and $\omega = \omega_w$, Equation (2.29). Continuous red line is for $\zeta_{U_{inc}} = 1$, dotted-dashed blue line for $\zeta_{U_{inc}} = 0.1$, dashed black line for $\zeta_{U_{inc}} = 0.01$	32

2.8	Computed phase angles for case 1 device of Gallas et al. [46]. Blue line refers to jet velocity - diaphragm velocity responses; red line to jet velocity - cavity pressure responses. Reprinted from [54].	34
2.9	Electro-mechanical analogy.	36
2.10	Comparison of experimental data and LEMs results of peak jet velocity for two actuators, reprinted from [54]. Blue markers are experimental data from Gallas et al. [46], blue line represents LEM by Gallas et al. [46], red line LEM by Sharma [54]. Left frame is for case 1, right for case 2.	42
2.11	Numerical, analytical and experimental comparison of average exit flow velocity for a Brass actuator (a, $H/d_o = 0.75$, $V_{ac} = 50V$) and for an Aluminum actuator (b, $H/d_o = 0.8$, $V_{ac} = 50V$).	45
2.12	Experimental mock-up with Pitot tube.	47
3.1	Frequency response of saddle point velocity for the Brass actuator at $V_a = 35V$; black dotted line refers to $H/d_o = 0.5$, magenta dash-dotted line to $H/d_o = 1$, blue dashed line to $H/d_o = 1.5$, red solid line to $H/d_o = 2.5$. The straight line refers to Equation (2.47).	50
3.2	Frequency response of saddle point velocity for the Aluminum actuator at $V_a = 35V$; black dotted line refers to $H/d_o = 0.5$, magenta dash-dotted line to $H/d_o = 1$, blue dashed line to $H/d_o = 1.5$, red solid line to $H/d_o = 2.5$. The straight line refers to Equation (2.47).	51
3.3	Spatially and temporally average <i>momentum velocity</i> for various cavity heights. Blue square markers are for $H = 20$ mm, red circles for $H = 40$ mm and black diamonds for $H = 60$ mm. Reprinted from [64].	52
3.4	Frequency response of diaphragm peak velocity for the Brass actuator a) and the Aluminum device b); black dotted line is for $K = 0.14$, red solid line $K = 1.14$, blue dashed line $K = 3.14$, magenta dash-dotted line $K = 5.14$	54

3.5	Frequency response of average jet velocity for the Brass actuator a) and the Aluminum device b); black dotted line is for $K = 0.14$, red solid line $K = 1.14$, blue dashed line $K = 3.14$, magenta dash-dotted line $K = 5.14$	55
3.6	Frequency response of acoustic damping coefficient (ADC) for the Brass actuator a) and the Aluminum device b); black dotted line is for $K = 0.14$, red solid line $K = 1.14$, blue dashed line $K = 3.14$, magenta dash-dotted line $K = 5.14$	56
3.7	SJ peak velocity response as a function of excitation frequency at resonant frequencies ($h/d_o = 2.1$ and $H/d_o = 0.56$). Blue data points are for diaphragm resonance, red data for acoustic resonance. Reprinted from [66].	58
3.8	Electric–fluid energy conversion efficiency as a function of excitation frequency. Blue line is for $V_{ac} = 90V$, red line for $V_{ac} = 250V$ ($h/d_0 = 2.1$ and $H/d_0 = 0.56$). Reprinted from [66].	59
3.9	Frequency response of saddle point velocity for the Brass actuator at different equivalent length; red solid line refers to $l_e/d = 1$, blue dashed line to $l_e/d = 2$ and black dotted line to $l_e/d = 3$	61
3.10	Frequency response of saddle point flow velocity for the Aluminum actuator at different equivalent length; red solid line refers to $l_e/d = 1$, blue dashed line to $l_e/d = 2$ and black dotted line to $l_e/d = 3$	62
4.1	PIV and injection system experimental apparatus (left) - Hole misting nozzle sketch (right).	73
4.2	Relative positions between the nozzle and the synthetic jet actuator.	75
4.3	Exploded 3D view of the Brass synthetic jet actuator.	76
4.4	Frequency response of the Brass SJ actuator.	77
4.5	Case 1: Spray velocity field ($P_{inj} = 5\text{ MPa}$, $h = 0\text{ mm}$).	81
4.6	Velocity profiles (Case 1): longitudinal axis (left) and transverse axis (right).	81
4.7	Case 2: Spray velocity field ($P_{inj} = 10\text{ MPa}$, $h = 0\text{ mm}$).	83

4.8	Velocity profiles (Case 2): longitudinal axis (left) and transverse axis (right).	83
4.9	Case 3: Spray velocity field ($P_{inj} = 5$ MPa, $h = 5$ mm).	84
4.10	Velocity profiles (Case 3): longitudinal axis (left) and transverse axis (right).	84
4.11	Case 4: Spray velocity field ($P_{inj} = 5$ MPa, $h = 5$ mm).	85
4.12	Velocity profiles (Case 4): longitudinal axis (left) and transverse axis (right).	85
4.13	Case 5: Spray velocity field ($P_{inj} = 5$ MPa, $h = 10$ mm).	86
4.14	Velocity profiles (Case 5): longitudinal axis (left) and transverse axis (right).	86
4.15	Case 6: Spray velocity field ($P_{inj} = 10$ MPa, $h = 10$ mm).	87
4.16	Velocity profiles (Case 6): longitudinal axis (left) and transverse axis (right).	87
4.17	No SJ actuation, 5 MPa: velocity field (left), vorticity field (right).	88
4.18	Case 1 (5 MPa, $h = 0$ mm): velocity field (left), vorticity field (right).	89
4.19	Case 5 (5 MPa, $h = 10$ mm): velocity field (left), vorticity field (right).	89
4.20	No SJ actuation, 10 MPa: velocity field (left), vorticity field (right).	90
4.21	Case 2 (10 MPa, $h = 0$ mm): velocity field (left), vorticity field (right).	90
4.22	Case 6 (10 MPa, $h = 10$ mm): velocity field (left), vorticity field (right).	91
4.23	Case 1 (5 MPa, $h = 0$ mm): velocity vector fields (left), vorticity field (right) in the impact region.	91
4.24	Case 2 (10 MPa, $h = 0$ mm): velocity vector fields (left), vorticity field (right) in the impact region.	92
5.1	Different phases of the PSJ operating cycle.	100
5.2	Sketch of the actuator with the geometric variables.	102
5.3	Mesh representation for the wedge used in the numerical simulation.	108

5.4	Time variation of thermo-fluid-dynamic quantities during the start-up cycle computed with OpenFOAM. (left) Jet exit velocity and mean cavity pressure; (right) mean cavity mass and temperature.	109
5.5	Comparison of results of LEM model (red) and OpenFOAM code (blue). (a) Mean cavity pressure, (b) exit velocity, (c) mean cavity temperature and (d) mean cavity mass.	110
5.6	Evolution of the main thermo-fluid-dynamic parameters of the actuator over the first 25 cycles.	112
5.7	Variation of maximum peak velocity with discharge frequency.	113
5.8	Evolution of main thermodynamic quantities over the first 25 cycles. Present model in red, Zong et al. [88] model in blue.	115
5.9	Evolution of the exit velocity for 24 th and 25 th actuation cycles. Present model in red, Zong et al. [88] model in blue.	116
5.10	Variation of maximum cavity temperature with discharge frequency. Present model is in red, Zong et al. [88] in blue (analytical) and in black (experimental).	117
5.11	Maximum peak velocity with respect the electrodes distance for different initial capacitor voltages. Blue solid line is for V=1000 V, red one for V=1500 V, Zong et al. [98]. Star markers refer to the present model.	118
5.12	Jet discharge duration with respect the electrodes distance for different initial capacitor voltages. Blue solid line is for V=1000 V, red one for V=1500 V, Zong et al. [98]. Star markers refer to the present model.	118
5.13	Evolution of thermodynamic parameters over the first 25 cycles. Present model is in red, Sary et al. [85] computations are in blue.	119
6.1	Picture of the main parts of the actuator. Bottom part on the left, top part on the right.	121
6.2	CAD reconstruction of the house-made PSJ actuator (left), detail of the electrodes location (right).	122
6.3	The power supply system: the red box contains the sustain circuit, while the blue the trigger one.	123

6.4	Front view of the power supply system. The top box contains the trigger circuit, the bottom one includes the sustain circuit.	125
6.5	The power supply system: the red box contains the sustain circuit, while the blue the trigger one.	125
6.6	PSJ signals. Blue line represents the trigger signal, red line the sustain one.	126
6.7	Actuator operating electrical phases. Device bottom part only (top row) and whole device (bottom row).	128
6.8	PSJ actuator with the Pitot probe.	129
6.9	Velocity profiles in the radial direction for different energy discharges. Blue markers are the results for $E_d = 1.2$ mJ, red ones for $E_d = 2.1$ mJ and black ones for $E_d = 3.4$ mJ.	130
6.10	Temperature field acquired with the Flir SC6000 infrared camera ($f = 500$ Hz, duty cycle of 5%).	131
6.11	Calibration Curve, (E, U).	133
6.12	PSJ actuator with the Hot-wire anemometer probe.	133
6.13	Variation of the mean jet velocity (Pitot tube measurements) with energy discharges for different actuation frequency. Black solid line refers to $f = 1000$ Hz, blue dotted line to $f = 750$ Hz, red dashed line $f = 500$ Hz, black dash-dot line to $f = 250$ Hz. Star markers represent experimental data.	134
6.14	Variation of the mean jet velocity (Hot-wire measurements) with energy discharges for different duty cycle (DC) values. Black solid line refers to $DC = 5\%$, red dotted line to $DC = 10\%$ and blue dashed line to $DC = 15\%$. Star markers represent experimental data.	135
B.1	Technical drawing: isometric view. Bottom part (left), top part (right).	147
B.2	Technical drawing: front view. Bottom part (left), top part (right).	148
B.3	Technical drawing: top view. Bottom part (left), top part (right).	148
B.4	Technical drawing: section A-A of the bottom part.	149
B.5	Technical drawing: section B-B of the bottom part.	149

B.6 Technical drawing: section A-A of the top part. 149

List of Tables

2.1	Typical effort and flow variables.	35
2.2	Basic dimensionless variables of the problem.	40
2.3	Features of the devices studied by Gallas et al. [46].	44
2.4	Features of the piezo-driven SJ devices experimentally tested.	46
3.1	Efficiencies of Brass actuator at modified resonance structural frequency. $CF=0.06$	68
3.2	Efficiencies of Aluminum actuator at modified resonance Helmholtz frequency. $CF=1.88$	68
4.1	PIV operating conditions.	76
4.2	Synthetic jet actuator characteristics.	77
4.3	Estimated values for the momentum coefficient, C_{μ}^*	80
6.1	Actuator geometrical variables.	122
6.2	Hot-wire probe (55P11) characteristics.	132
6.3	Coefficients of the (E, U) calibration curve.	132

Chapter 1

Introduction

1.1 Flow control

The ability to control a flow field, manipulating its structure, is one of the most important topics in fluid dynamics. It consists in a process or a mechanism able to modify the natural behavior of the flow over a surface, or in a particular environment, inducing a certain desired change. An efficient flow control system, indeed, can have a positive outcome not only on the efficiency of different vehicles, reducing the fuel consumption, but also on the improvement of many industrial processes which involve fluid flows.

Nowadays, a huge number of flow control mechanisms are available both for external boundary layers and internal flows. The choice of the control strategy depends on the particular goal to be achieved. Usually, these methods aim to improve aircraft performances and to stabilize or to mix airflow in order to avoid unsteadiness, which generates unwanted vibrations, noise and energy losses, Moreau [1]. These results are, generally, related to three main phenomena: laminar-turbulent transition, separation and turbulence. In more detail, a delay in laminar-to-turbulence transition can positively impact on skin friction drag, reducing its values of an order of magnitude, leading to longer ranges and reduced fuel costs; on the other hand, an early transition can enhance heat transfer mechanisms and improve the performances of mixers. The separation control allows, for instance, reduction of the parasitic cruise drag and the improvement of conventional

high lift devices, affecting the aircraft dimensions and take-off and landing distance. Finally, an enhancement in turbulence can lead to a better flow mixing, while its decrease can have a significantly effect on noise reduction. A survey of the interrelation between flow control goals can be found in Gad-el-Hak, [2] and is reported in Figure 1.1.

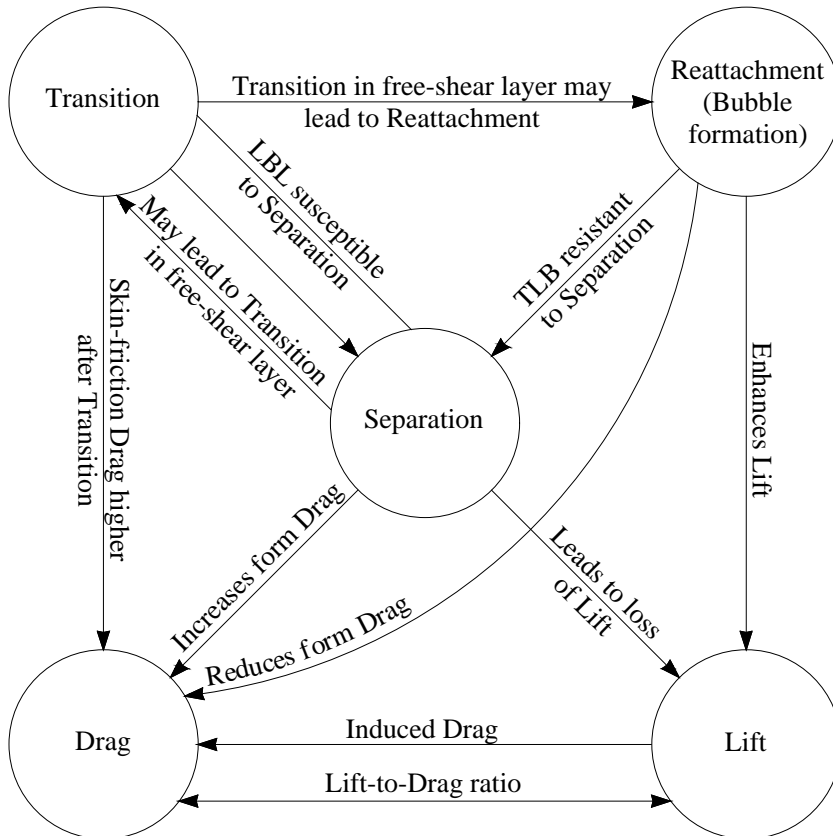


Figure 1.1: Interrelation between flow control goals, reprinted from [2].

The choice of a control method must be done very carefully, because the attempt to achieve a specific goal may adversely effect on others. For this reason, the final decision will be the result of a trade-off process aimed to maximize the effect of a particular design goal and to reduce the consequences on the other objectives.

1.2 Classification

Flow control approaches can be categorized differently depending on the specific applications. One of the most frequent classification of flow-control methods considers the devices as *active* or *passive*, depending on the energy consumption and the control loop presence. The operating modes of a passive control device do not require any external power supply or control loop mechanism; whereas an active approach demands an energy expenditure. Classical examples of passive flow control devices are represented by the vortex generators (Lin [3]) and the riblets (García-Mayoral and Jiménez [4]).

Any active control approach is strictly related to the installation of an actuator to interact with the system to be controlled. An actuator can be defined as a transducer which converts an electrical signal to a desired physical quantity, Cattafesta [5]; it is, generally, an entire subsystem added with the aim to influence the system with electrically controlled disturbances. Following the work of MacMynowski [6], this class can be further divided in *open-loop* and *closed-loop* devices.

An open-loop strategy may use data from the system which are not influenced by the operation control, so no information is available to determine how well the control is working. On the other hand, a closed-loop control system predicts a sensor to be used to modify the output of the actuator, which in turns affects the sensor through the dynamic of the plant. With this in mind, open-loop approaches include: the so-called predetermined control, being energy consumption applications not related to any sensor measurements and so to any particular state of the flow; the purely scheduled (pre-defined variation of the actuation as function of some system parameters), and the purely forward systems, in which a canceling signal is introduced based on an upstream measurement of the disturbance to be canceled.

Another distinction should be made between *feedforward* and *feedback* approaches. Both of them depend on the sensor measurements, but the basic idea is completely different. In the feedforward strategy, information does not depend essentially on the effect of the control device on the overall system, and it aims to inform the controller with an advance knowledge

of the disturbances. For instance, within a feedforward control strategy of a flow field, pressure and velocity measurements can be acquired at a certain upstream location and used, with an appropriate control law, to trigger an actuator, which affects the flow field at a downstream position. On the other hand, within a feedback strategy the controlled variables must be measured, fed back and compared with reference input. This means that the sensor measurements are directly related to the performances of the actuator. A closed-loop control system is strictly related to a feedback approach. Considering again the previous example, the output of an actuator can be adjusted using velocity and pressure measurements acquired at a downstream position, in such a way that the actuator response can be constantly modified to obtain the desired flow characteristics. A very interesting work on the closed-loop control problem has been done by Dadfar et al. [7].

Finally, flow control closed-loop systems can be further subdivided with respect to the timescale. When the control commands are quickly adjusted with a timescale comparable to the dynamics of the system, the control strategy is defined *dynamic*; whereas when the adjustments are carried out very slowly with respect to the dynamics of the flow, then the control system is called *quasy-steady*.

A general classification of the flow-control strategies is reported in Figure 1.2. It's worth noting that, although this categorization is widely accepted in the academic world, the sectors boundaries (of the previous classification) are not particularly strong, leading to possible overlaps and so small subjective variations. From this point on, only the active flow control methods will be considered.

1.3 Actuator types

In the last few years, active flow control (AFC) methods have gained much interest in several industrial applications, especially in the aerospace field, due to their ability to manipulate the flow and modify its structure, leading to favorable economic and environmental outcomes. A valuable classification of flow control actuators was presented by Cattafesta and Sheplak [5],

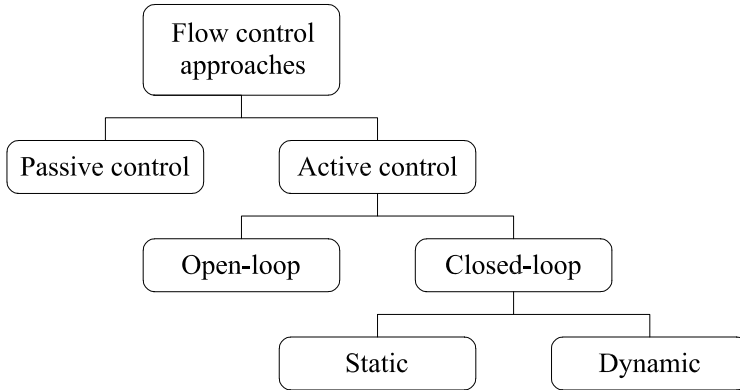


Figure 1.2: A classification of different flow-control approaches, reprinted from [6].

where the devices have been organized according to their functions.

A first class of actuators, widely used and studied, comprises the *fluidic* type, which are characterized by fluid injection and/or suction phases. In the following, the main types of fluidic actuators are briefly reviewed.

- Among them, synthetic jet (SJ) actuators have undoubtedly a prevalent role. They consist of a relatively small cavity, sealed from one side by an elastic vibrating diaphragm, and linked, from the other, to the external environment through a slot or an orifice. They produce a jet through alternating ejection and suction phases, with a null average mass flow rate during an operation cycle (zero-net mass-flux, ZNMF), whilst a non-zero average momentum rate, Glezer and Amitay [8]. These devices will be presented in detail in the Part I of the present work, focusing here only on their benefits and disadvantages. SJ actuators require very low power consumption, their actuation frequency can range from few to several KHz and they use only the working fluid without any external mass source. The main disadvantages are related to a maximum velocity around 100 m/s, mechanical failure due to fatigue mechanism and noise problems.
- On the other hand, all the other devices in this category require an ex-

ternal fluid source for their operating conditions. They can be pulsed jets, characterized ideally by on or off phases and controlled using a square wave with an adjustable duty cycle. They have been extensively used in different applications, especially aerospace (Magil and McManus [9]) and automotive (Joseph [10]) fields, producing very high velocities, with either fast time response or high bandwidth. They can be generated with the use of fast valves (Becker et al. [11]), with a restricted range of waveforms due to their particular design, and can reach very low dimensions (Choi et al. [12]).

- A very interesting type of fluidic actuator is the so-called powered resonance tube, or Hartmann whistle. It consists of an air under-expanded jet directed to a cylindrical resonator tube open at one and closed at the other. The periodic flow in and out of the resonator tube, and its interaction with the incoming jet produces a strong acoustic field with a variable frequency and amplitude, Raman and Srinivasan [13]. The main advantage of these actuators is that their high-frequency excitations can be used to control high-speed flows; however, they do not have a fast time response and the disturbances amplitude is barely adjustable.
- Moreover, another very fascinating class of devices is represented by the combustion-driven actuators. These devices exploit the chemical energy of a gaseous fuel/oxidizer mixture to produce a high momentum jet, Matalanis [14]. The operating cycle starts with a spark to ignite the mixture within the combustor, creating a high pressure burst and a subsequent jet emanating from one or more exhausts orifices. The operating frequency can be controlled by varying the flow rate of the mixer and the ignition frequency. Although they are able to produce vary large perturbations in high-speed flows, these devices are limited to relatively low frequencies, requiring the addition of an external reactant flow.
- The last class of actuators taken into consideration here is concerned with the fluidic oscillators. These devices generate a pulsed jet, when supplied by a pressured fluid, with a controllable frequency and no

moving parts, Raghu [15]. Their basic principles are represented by the Coanda effect and/or the fluidic interaction. They are capable of producing large disturbances, with an independent control of frequency and velocity; however, they are not ZNMF and require some adjustable techniques for a feedback control.

A second class of actuators consists in *moving objects/surfaces* to be installed within the domain, whose main goal is to induce local fluid motion. In the last decades, moving bodies have been extensively applied in aerospace field, from the ribbon oscillator used in the first flat plate experiments (Schbauer and Skramstad [16]) to the modern morphing surfaces. The most common actuators are the piezoelectric composite flaps and electroactive dimples.

- The piezoelectric flap actuators can introduce spanwise or streamwise vortical perturbations into the flow depending on the geometry and orientation of the vibrating tip with respect to the local freestream flow, Cattafesta and Sheplak [5]. The application of an ac voltage across the piezoceramic induces an asymmetric alternating mechanical strain in the composite beam cross section due to the piezoelectric effect. This ac strain results in oscillatory bending of the beam, which then interacts with the flow. Both unimorph, with a piezoceramic on one side of the shim, and bimorph configurations, with a piezoceramic bonded symmetrically to both sides of the shim, are possible.
- Electroactive polymers (EAPs) have been successfully used for turbulent boundary-layers control due to their light weight and their ability to dynamically modify the surface of the airfoil, remaining flush-mounted when unactuated. Electroactive polymer actuators can create time-dependent dimples that actuate from a flush to depressed position at a certain frequency and amplitude. They consist of an elastomer sandwiched between compliant electrodes. When an electric potential is applied across the electrodes, the electrostatic pressure acts. Due to the mechanical compression the elastomer film contracts in the thickness direction and expands in the film plane ones. The dimples thus produce unsteady surface depressions which interact with the near-

wall turbulent structure. The elastomer film moves back to its original position when it is short-circuited. Note that the dimple amplitude can be controlled by the actuation frequency, input voltage, material selection, and manufacturing techniques to create motion appropriate to a wide range of flow conditions, DeMauro [17].

The last category of actuators includes the *plasma* actuators. The plasma technology is relatively recent and these actuators have gained much interest for their very short response time, low weight and lack of any moving parts. The most common actuators are the surface corona and the single dielectric barrier discharge (DBD) actuators; other very interesting devices are the sliding discharge, the arc filament and the plasma synthetic jet (PSJ) (or sparkjets) actuators, Moreau [1].

- In the case of a surface corona discharge actuator, the device consists of two wire electrodes placed inside a groove at the wall surface between which a dc high voltage is applied, Moreau et al. [18]. In ambient air, a corona discharge is formed around the lowest diameter electrode (usually the positive one) and an electric wind is formed tangentially to the wall. The electric wind accelerates the airflow tangentially, modifying the velocity profile within the boundary layer, and therefore manipulating its structure. Under certain favorable conditions the plasma may extend to the second electrode. It is possible also to use an ac high voltage rather than a dc excitation, but, apart from reproducing a pulsed electric wind, no particular advantages are expected. The electric wind produced by these devices can be of several m/s, but it is limited by stability discharge problems. An evolution of this technology is represented by the DBD actuators.
- The stability discharge problems of the previous technology can be prevented by placing a dielectric barrier between the electrodes gap, which stops the electric current and prevents spark formation. This is the case of the dielectric barrier discharge (DBD) actuators, Massines et al. [19] and Kriegseis et al. [20]. Due to the dielectric presence, a dc high voltage cannot be used, so these devices are frequently excited by ac or pulsed high voltage (1 – 30 kV) and frequency ranging from

50 Hz to 500 kHz. The main advantage of this technology is that it directly converts electric energy into kinetic one without moving parts. These devices have a very short response time, allowing control at high frequencies. On the other hand, one of the main disadvantages is related to their very low efficiency in the energy conversion process. Furthermore, they could also modify the gas properties at the wall, such as density and viscosity.

- The sliding discharge devices are composed of two electrodes, one flush-mounted on the wall surface of a dielectric material and another planar on the other side. It represents a combination of an ac DBD to generate a local barrier discharge and a dc component to induce the formation of extended stable plasma sheets between the two electrodes of the same side, Moreau et al. [21]. The device presents a more stable behavior than a classical DBD actuator, with increased body forces.
- The localized arc filament plasma actuators produce rapid localized heating of the flow by high-current filaments, generating shock waves and so perturbing high-pressure transonic and supersonic flows, Yugulis et al. [22]. Rapidly heated regions near the surfaces, in fact, may act similarly to a physical geometry alteration in the flow, such as tabs and cutouts. Repetitive pulsing of the discharge would be analogous to periodic insertion and removal of these obstacles, and could be used to excite flow instabilities.
- A plasma synthetic jet actuator, or Sparkjet, is a device developed originally at the Johns Hopkins University [23, 24] at the beginning of the century. It is mainly composed of 2 or 3 electrodes embedded in a small cavity linked to the external environment through an orifice. The operating cycle begins with an electrical discharge between the electrodes, which increases sharply pressure and temperature inside the cavity. The high-pressure air exhausts through the orifice, converting the increased air internal energy into kinetic one. In the end, fresh air is drawn back inside the cavity, refilling the device for the next pulse. After a limited number of cycles the device reaches a periodic behavior, generating a plasma synthetic jet. These kind of

devices will be deeply investigated in the Part II of this work.

1.4 Thesis layout

Based on the brief review presented in the previous section, it is evident that active flow control plays a fundamental role in fluid mechanics, not only for the innovation in the academic world, but also for its tremendous potential, in terms of economic impact for industrial applications. Among all available AFC methods, synthetic jet actuators seem to be a very promising technology due to their short response time, high jet velocity and absence of traditional piping, that matches the modern requirements of reduced size and low weight. In fact, they can produce non-zero average momentum rate, with a null average mass flow rate during an operating cycle. Therefore, understanding in depth the basic physical aspects driving the operation of these actuators is a key point.

The fluid dynamic behavior of the actuators could be clearly obtained by means of numerical simulations (RANS, LES and DNS), that, except for particular cases, they are not ready for practical engineering calculations. Another very useful tool, employed for design and manufacturing purposes, consists in the definition of a low-order model, which is able to predict the dynamic response of the actuator in a relatively quick way and with reasonable fidelity and accuracy. Within this latter class of modeling, lumped element models (LEMs) represent a very practical tool to obtain the time variation of all thermodynamic variables inside the cavity as well as the jet velocity at the orifice, as functions of the operating frequency. The way in which the author exploits this idea is directed to the implementation of different lumped models for both devices (piezo-driven SJ and PSJ actuators), they have been validated against experimental data obtained using home-made actuators.

This research activity tries to tackle different aspects to achieve various goals. A major task concerned the development of LEMs to predict the behavior of two types of actuators: piezo-driven SJ and Plasma Synthetic Jet (PSJ) actuators. These models share the same philosophy: they represent valuable tools useful not only for design purposes, but also to obtain useful

insights on the devices performances.

A second crucial task consists in the design, manufacturing and characterization of various prototypes, which have been used to validate LEMs results. Several operational problems have been faced throughout the three-year activity, going from the bond required for the piezo/membrane coupling in the piezo-driven actuators, to the power supply system in the PSJ case. As an additional task of the research activity, applications both in automotive and aerospace fields have been considered.

The objectives of this work can be summarized as: development of lumped element models for piezo-driven and plasma synthetic jet actuators and models validation through experimental data obtained using different house-made prototypes. The work is essentially divided in two parts: the first is dedicated to piezo-driven SJ actuators, while the second to the PSJ devices.

The second chapter faces the development of various lumped-element models as practical tools for design and manufacturing purposes. It provides an overview on this topic, analyzing the actuator performance by varying typical geometric parameters and facing the different nature (and the intrinsic links) of existing literature LEMs models.

The third chapter is dedicated to the analysis of the major device performances (basically the frequency response in terms of jet velocity), as functions of the main parameters that influence the oscillators coupling, the supply voltage and the effective orifice length. It contains, also, the analysis of the device efficiency, based on a physical model directly related to the energy equations of the two coupled oscillators.

The fourth chapter regards the influence of a SJ actuator on the behavior of a continuous water spray. Experimental data, carried out under atmospheric conditions within a chamber test rig at two injection pressures and for different SJ positions, are reported. Starting from the flow field velocity distributions, computed with Particle Image Velocimetry (PIV), the effective influence region of the device on the spray is computed through a T-Test algorithm and corroborated by a vorticity analysis.

In the fifth chapter a different type of actuator is introduced: the plasma synthetic jet actuator. Taking advantage of all the know-how acquired for

the previous technology, an innovative lumped-element model, able to predict the temporal evolution of the main fluid-dynamic variables of the device, is presented. The model is fully based on the gasdynamics equations, includes viscous losses as well as radiative and convective heat transfer mechanisms at walls, and models the air as a real gas. Numerical computations have been carried out, by the OpenFOAM code, to perform a first calibration of the lumped model through the determination of key fitting parameters. Results for both single pulse mode and repetitive working regimes are reported, providing insights on the major actuation characteristics.

Finally, the sixth chapter contains a description of the PSJ home-designed actuator, developed to validate the model presented in the previous Chapter. A detailed explanation of the experimental mock-up is carried out, together with details on the control electrical system. Experimental measurements of the jet velocity complete the actuator characterization and the model validation. Finally, the sixth chapter contains a description of the PSJ home-designed actuator, developed to validate the model presented in the previous Chapter. A detailed explanation of the experimental mock-up is carried out, together with details on the control electrical system. Experimental measurements of the jet velocity complete the actuator characterization and the model validation.

Part I

Piezo-driven Synthetic Jet Actuators

Chapter 2

Piezo-driven synthetic jet actuators: LEM

2.1 Introduction

It has been many years since Synthetic Jet (SJ) actuators have been used for active flow control, particularly for aerospace applications. These devices are able to manipulate the flow, to modify its structure and allow a favorable variation of the aerodynamic forces on aircrafts (Glezer and Amitay [8], Cattafesta and Sheplak [5], Smith and Glezer [25]). Their application field is extremely wide, including flow control (e.g., Glezer [26] and, more recently, Van Buren et al. [27]), mixing enhancement (Wang and Menon [28], Tamburello and Amitay [29]), heat transfer from small surfaces (Pavlova and Amitay [30], Chaudari et al. [31]), spray vectoring (Pavlova et al. [32], Marchitto et al. [33]), micropropulsion (Finley and Mohseni [34], Parviz et al. [35]), active control for MAV (Otani et al. [36]), and many others.

As depicted in Figure 2.1, a synthetic jet is an electromechanical device consisting of a relatively small cavity, which is sealed from one side by an elastic vibrating diaphragm, and from the other one it is linked to the external environment through a slot or an orifice. This work will refer to nominally axisymmetric devices only, with round orifice. The oscillation of the diaphragm (wall), which is generally constituted by a thin metallic shim on which a piezo-ceramic element is glued, produces periodic cavity volume

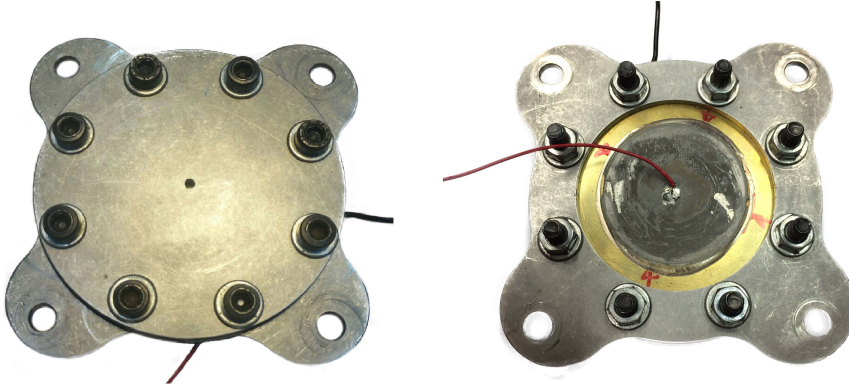


Figure 2.1: Typical synthetic jet device driven by a piezoelectric element. left) top view with orifice; right) bottom view with metallic shim and piezodisk.

changes, with corresponding pressure variations, that cause subsequent alternation of ejection and suction phases of fluid across the orifice. During the expulsion phase a vortex ring forms near the orifice exit which, under favorable operating conditions, convects downstream by its self-induced velocity towards the far field. A few cycles are required for the formation of a train of vortex rings that interact with each other and break up due to the viscous dissipation, eventually “synthesizing” a turbulent jet always directed downstream. In more detail, during the suction phase a stagnation point is formed, located about one orifice diameter away from the orifice itself, known also as “saddle point”. This point which separates the near field region, where the flow is directed towards the cavity, from the far field where the jet is established; a representation of this point is reported in Figure 2.2, extracted from the work of Greco et al. [37]. A major characteristic of this jet is that the average mass flow rate during an operation cycle is null, whilst a non-zero average momentum rate is produced. Furthermore, its generation does not require any continuous fluid supply, because it is synthesized directly from the surrounding fluid, see e.g. Smith and Glezer [38] and Cater and Soria [39].

Synthetic jets have been extensively studied both from experimental and numerical points of view. Hot-wire Anemometry, Laser Doppler Velocimetry

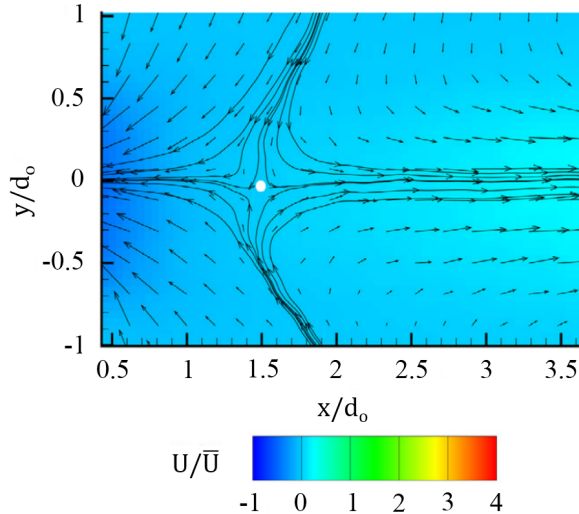


Figure 2.2: Phase-averaged flow field with saddle point (white spot) generated by a SJ actuator, reprinted from [37].

(LDV) and Particle Image Velocimetry (PIV) are only some of the several measurement techniques applied to determine the flow field generated by these devices, see Mohseni and Mittal [40]. On the other hand, many CFD simulations have been conducted, spanning the first RANS and the very recent LES and DNS computations, to achieve further details of the flow fields inside the cavity as well as near the orifice, both in quiescent and cross-flow conditions (e.g., Rumsey et al. [41], Dandois et al. [42], Lardeau and Leschziner [43]). Another very useful tool, employed for design and manufacturing purposes, consists in the definition of a low-order model, able to predict the dynamic response of the actuator in relatively quick way and with reasonable fidelity and accuracy.

Within this latter class of modeling, Lumped Element Models (LEMs) represent a very practical tool to obtain the time variation of all thermodynamic variables inside the cavity as well as the jet velocity issuing from the orifice, as functions of the operating frequency. One of the earliest lumped modeling applications to synthetic jets has been presented by McCormick [44], who developed a simplified electro-acoustic model predicting the velocity performance of a SJ actuator driven by a loudspeaker acoustic forcing.

The extension of this model to a piezoelectric-driven device (constituted of a thin piezo-ceramic disk glued on a metallic shim) has been carried out by Prasad [45] and further studied by Gallas et al. [46], who modeled the individual components of the actuator as elements of an equivalent electrical circuit, including a very detailed description of the behavior of the composite oscillating diaphragm. The model was validated against experimental measurements of the orifice exit velocity. Following the electroacoustic approach, many other lumped models have been realized, which take into account more and more effects about the piezoelectric element (Prasad et al. [47], Persoons [48]), minor losses (Tang and Zhong [49]), electromagnetic driver (Agashe et al. [50], Sawant et al. [51]) and double cavity (Luo et al. [52], Arunajatesan [53]).

Later on, a physical model directly based on fluid-dynamics equations has been presented by Sharma [54], who considered the oscillating wall as a single-degree-of-freedom mechanical system, while the cavity-orifice arrangement is basically described by suited forms of continuity and Bernoulli's unsteady equations. This last model inspired the work of de Luca et al. [55], who provided additional analytical and numerical insights on the frequency response of SJ actuators driven by piezoelectric thin elements (among others, the prediction of the coupled resonance frequencies and the conditions to maximize the peak velocity). To sum up, lumped element models can be clustered in two categories: the former based on an equivalent electrical circuit; the latter fully based on fluid-dynamics equations. In both cases, the device is considered as a coupled mechanical-acoustic resonator with two degrees of freedom, exhibiting two resonance frequencies near the uncoupled Helmholtz and diaphragm structural resonance frequencies.

Based on the experience of the present author, this chapter aims at presenting a comprehensive review covering the development and the evolution of LEM modeling for the design and the performance evaluation of synthetic jet actuators. It provides an overview on this topic, analyzing the actuator performance by varying typical geometric parameters and facing the different nature (and the intrinsic links) of existing literature LEMs models. The innovative contribution can be found not only in the results reported but also on the new formulations and further insights presented below.

With this in mind, the paragraph 2.2 deals with the description of different lumped models that have been developed to characterize SJ devices. A careful description of these models appears to be mandatory to emphasize their strength but also their limitations. The paragraph 2.3 is dedicated to the dimensionless form of the relevant governing equations; while the results produced by the two basic LEM approaches, the one fully based on the fluid dynamics equations, and the other one obtained within the so called equivalent electric circuit framework, are presented in paragraph 2.4.

2.2 Lumped Element Models

A lumped element model is a low order model which, under certain assumptions, allows to describe the behavior of a physical system through a finite number of components (lumped elements) properly connected to each other. In general, the typical size of each component is small relative to a characteristic wavelength. This simplification decouples temporal and spatial variations, since the component is considered as being concentrated at a nodal point, and thus the partial differential equations of the distributed system are reduced to a set of coupled ordinary differential equations in time. The lumped modeling is a practical tool for design and manufacturing intents, and provides the dynamic response of a complex system in a relatively short computation time with a sufficient level of accuracy. Within the present context, with reference to the cavity flow which undergoes alternate compression and expansion phases due to the wall oscillations, the internal pressure can be considered uniform at any given time instant if the wavelength of the pressure oscillations is much larger than a typical dimension of the actuator cavity, Sharma [54]. In other terms, the basic assumption is that the crossing time of an acoustic perturbation generated by the elastic diaphragm, traveling from the diaphragm to the opposite (rigid) cavity walls, is much smaller than the actuation period; in this case, the acoustic perturbation generated at a (moving) boundary is instantaneously imposed to the whole control volume (namely, the cavity). The lumped assumption may of course become invalid at very high frequencies.

Most previous LEM contributions on SJ devices are based on the electric

circuits analogy (McCormick [44], Prasad et al. [45], Gallas et al. [46] and Persoons [48]). Due to their intrinsic nature, these models yield the system stationary (periodic) solution, and focus their attention on the evaluation of the impedances of the various circuit components. On the contrary, fluid dynamics based LEMs generally result in an initial value problem of ordinary differential equations and the solution is obtained numerically by integrating in time the governing equations with, for instance, Runge-Kutta type methods (Sharma [54] and de Luca et al. [55]); however, it will be shown in paragraph 2.2.2 how the stationary solution can be directly obtained by enforcing analytical *modal* solutions to the problem. In this chapter the fluid dynamics approach is mostly discussed; it will be presented hereafter through the formulations described by Sharma [54] and de Luca et al. [55]; then, once defined the two-coupled-oscillator mechanical layout, the mass-inductance electro-mechanical analogy is applied to obtain the equivalent electric circuit and the relevant impedances.

2.2.1 Fluid dynamic LEM

A modeling directly based on fluid mechanics equations was presented originally by Sharma [54] and extended by de Luca et al. [55] later on. The model is able to predict cavity pressure fluctuations, flow velocity at the orifice exit section, average displacement and velocity of diaphragm, as well as phase-lag relationships between the different variables. As anticipated in the previous paragraph, the three basic elements of the actuator are modeled: the oscillating diaphragm, the cavity and the orifice. In Figure 2.3 is reported a sketch of a piezo-driven SJ device.

The dynamics of the diaphragm is described through the equation of motion of a one-degree-of-freedom forced-damped spring-mass system:

$$\ddot{x}_w + 2\zeta_w\omega_w\dot{x}_w + \omega_w^2x_w = \omega_w^2\Delta x_w \sin \omega t - \frac{p_i A_w}{m_{wt}} \quad (2.1)$$

where $x_w(t)$ is the diaphragm (average) displacement at a generic time instant t , ζ_w is the actual damping ratio of the diaphragm, ω_w its natural frequency, Δx_w is the average linear diaphragm displacement due to the application of a certain voltage to the piezo-element, ω is the operating fre-

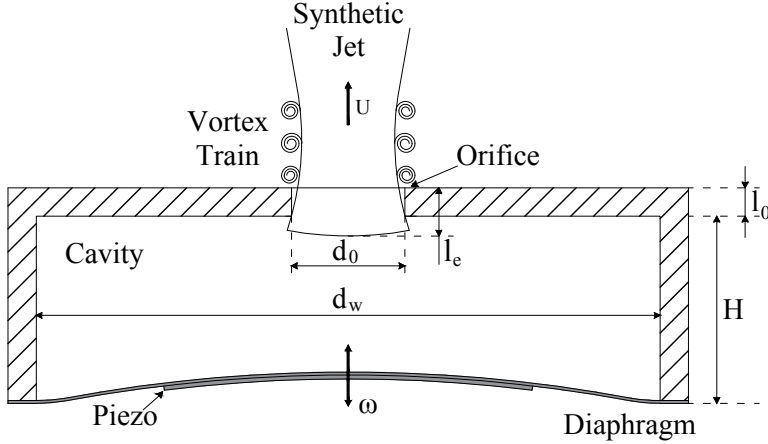


Figure 2.3: Sketch of a typical synthetic jet device driven by a piezoelectric element.

quency, and the dot superscript stands for time derivative. Furthermore, p_i represents the cavity (internal) differential pressure, A_w is the diaphragm surface area and m_{wt} is the diaphragm total mass, including shim, piezo-element and air added mass. The structural frequency of the composite diaphragm is defined as:

$$\omega_w = \sqrt{\frac{k_w}{m_{wt}}} \quad (2.2)$$

which represents the uncoupled (first mode) natural frequency of the structural oscillator, where k_w is the diaphragm equivalent spring stiffness. This latter is evaluated as:

$$k_w = m_w \left(2\pi \tilde{f}_w \right)^2 \quad (2.3)$$

where \tilde{f}_w is the frequency of the principal vibration mode of a rigidly clamped disk, assumed equal to the first fundamental mode of the shim only (Rathnasingham and Breuer [56] and Kinsler et al. [57]), that is the structural element actually clamped, while m_w is the diaphragm mass including both shim and piezo-ceramic disk. Higher modes also can be excited at relatively high frequencies, as depicted in Figure 2.4, where the diaphragm deflection detected by a Polytec laser scanning vibrometer PSV400-H4 is reported for operation frequencies f of 1555 Hz and 5370 Hz, respectively,

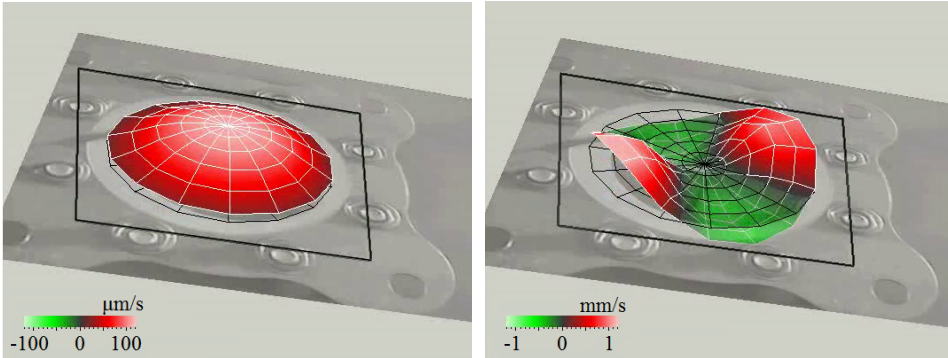


Figure 2.4: Aluminum shim diaphragm deflections detected by laser vibrometer. a) fundamental mode (0,1) for actuation frequency $f = 1555$ Hz; b) mode (2,2) for $f = 5370$ Hz. Applied voltage is $V_{ac} = 6$ V.

and very low voltage, $V_{ac} = 6$ V. The device has an aluminum shim with a diameter of 42 mm, while the chamber is 3 mm in height. Note that the presence of higher-order structural modes is not desirable because the distorted shim shape vibrating at natural frequencies higher than its fundamental one produces little net displacement of the surrounding air.

The electro-dynamic force (applied to the diaphragm by the piezoelectric element) is modeled as $F = F_o \sin \omega t$, with F_o being the force magnitude:

$$F_o = \frac{k_w d_a V_{ac}}{A_w} = k_w \Delta x_w \quad (2.4)$$

where the average linear displacement Δx_w is expressed as the cavity volume variation $\Delta V = d_a V_{ac}$ divided by the wall area, and V_{ac} represents the applied voltage. It is important to note that, despite what is shown by Equation (2.4), the dependence of the dynamic deflection of the piezo-element on the driving voltage is not linear, but the slope of the curve deflection-voltage decreases with increasing voltage, and it is a function of the operating frequency, as investigated by Krishnan and Mohseni [58]. This behavior of the piezo-materials influences the performances of the actuators, as will be shown in paragraph 3.1.2. The effective acoustic piezoelectric coefficient d_a is defined as the ratio of the volume variation to the applied voltage, when

the driving differential pressure across the piezo-element is null, Prasad [45],

$$d_a = \left. \frac{\Delta V}{V_{ac}} \right|_{p=0} \quad (2.5)$$

The determination of d_a could not be trivial since it requires the knowledge of the transverse displacement distribution of the composite diaphragm, as outlined by Prasad [45] and Prasad et al. [47]; a more convenient procedure consists in determining the acoustic compliance of the diaphragm C_w as:

$$C_w = \left. \frac{\Delta V}{p} \right|_{V_{ac}=0} \quad (2.6)$$

and to relate it to d_a through the electroacoustic transduction coefficient Φ_a :

$$d_a = C_w \Phi_a \quad (2.7)$$

The acoustic compliance is then determined from piezo-ceramic properties:

$$C_w = \frac{\pi d_{pc}^6 (1 - \nu_{pc}^2)}{1024 E_{pc} t h_{pc}^3} \quad (2.8)$$

with th_{pc} , d_{pc} , E_{pc} , and ν_{pc} being the thickness, the diameter, Young's modulus, and Poisson's ratio of the piezo-ceramic respectively. From their physical definitions, the relationship between the stiffness and the compliance is easily obtained:

$$C_w = \frac{A_w^2}{k_w} \quad (2.9)$$

Because of the difficulties in determining the electro-mechanical properties of the composite diaphragm, in practical applications the modeling described above considers the electroacoustic transduction coefficient Φ_a as a fitting parameter to be determined by comparisons between numerical and experimental data.

The second equation of the model is represented by the conservation of mass inside the cavity under the assumption of zero-dimensional system. By relating the density and pressure variations by means of an isentropic compression/expansion transformation, the continuity equation can be for-

mulated as:

$$\frac{V_c}{\gamma p_a} \frac{dp_i}{dt} - A_w \dot{x}_w = -A_o U \quad (2.10)$$

where $V_c = A_w H$ is the cavity volume (with H being the cavity height), A_o is the orifice area, γ is the specific heat ratio of air, p_a is the external ambient pressure and U is the instantaneous flow velocity through the orifice, namely the jet velocity.

Finally, the model is completed with the unsteady Bernoulli's equation, applied between a point inside the cavity, where the flow velocity is practically null and a point just outside the cavity, which represents the location where the pressure matches the unperturbed external ambient value:

$$\ddot{U} + \frac{K}{l_e} |U| \dot{U} + \omega_H^2 U = \frac{A_w}{A_o} \omega_H^2 \dot{x}_w \quad (2.11)$$

In Equation (2.11), K is the head loss coefficient, including the inviscid contribution (equal to unity) due to the kinetic energy recovery at ambient pressure, minor (entrance/exit) losses, and distributed losses due to friction inside the orifice duct. The distance between the two points of application of the Bernoulli's equation is referred to as the modified (effective) length of the orifice, l_e . More details and typical values for K can be found in Sharma [54] and de Luca et al.[55]. The Helmholtz frequency is defined as:

$$\omega_H = \sqrt{\frac{\gamma A_o^2 p_a / V_c}{\rho_a l_e A_o}} = \sqrt{\frac{k_a}{m_a}} \quad (2.12)$$

with k_a and m_a being the equivalent stiffness of the air inside the cavity and the effective mass of the air at the orifice.

By taking the time derivative of Equation (2.1), and eliminating the pressure derivative by means of Equation (2.10), it is possible to obtain:

$$\ddot{V}_w + 2\zeta_w \omega_w \dot{V}_w + (\omega_w^2 + \omega_{wc}^2) V_w = \frac{A_o}{A_w} \omega_{wc}^2 U + (\omega \Delta x_w) \omega_w^2 \cos \omega t \quad (2.13)$$

which has to be coupled with Equation (2.11). $V_w = \dot{x}_w$ denotes the diaphragm velocity. Following Sharma [54], the frequency ω_{wc} represents the natural frequency of the pneumatic spring made of the air enclosed within

the cavity volume, V_c , and the oscillating diaphragm of mass m_w :

$$\omega_{wc} = \sqrt{\frac{\gamma A_w^2 p_a / V_c}{m_{wt}}} = \sqrt{\frac{\gamma A_w p_a}{m_{wt} H}} \quad (2.14)$$

To sum up, the actuator behavior is modeled by the dynamics of two mutually coupled oscillators: the first one, describing the diaphragm motion, Equation (2.13), is characterized by the uncoupled natural frequency ω_w , while the second one, the acoustic oscillator, Equation (2.11), describing the dynamics of the mass of air at the orifice, m_a , through its velocity U , is characterized by its natural frequency ω_H . An external forcing due to the supply power also acts on the diaphragm dynamics.

Making the further assumption of absence of damping effects (the practical validity of such an assumption has been discussed deeply in previous papers), for temporal behavior of the free oscillations $\sim e^{j\omega_n t}$, a closed-form analytical evaluation of the natural coupled (or modified) frequencies is obtained:

$$\omega_n^2 \equiv \omega_{1,2}^2 = \frac{(\omega_w^2 + \omega_{wc}^2 + \omega_H^2) \pm \sqrt{(\omega_w^2 + \omega_{wc}^2 + \omega_H^2)^2 - 4\omega_H^2 \omega_w^2}}{2} \quad (2.15)$$

The natural coupled frequencies in the totally undamped case are often also expressed conveniently in Hz, namely:

$$f_{1,2} = \frac{\omega_{1,2}}{2\pi} \quad (2.16)$$

Despite the seemingly strong simplification, predictions based on the previous relationship are in several circumstances in very good agreement with data obtained by experimental measurements, de Luca et al. [55]. In some applications, a desirable operating condition is represented by a relatively high plateau of fluid ejection velocity over a rather wide range of frequencies. This condition can be attained by designing the devices so as to have the two frequencies ω_1 and ω_2 close to each other. In fact, upon inspection of Equation (2.15), one argues that when $\omega_w \ll \omega_H$, the distance between

the frequencies is a function of the cavity height:

$$|\omega_1^2 - \omega_2^2| \cong \frac{1}{H/d_o} \quad (2.17)$$

On the other hand, if $\omega_w \gg \omega_H$, then:

$$|\omega_1^2 - \omega_2^2| \cong \text{const} \quad (2.18)$$

The above findings were obtained experimentally by Gomes et al. [59], who carried out extensive measurements to characterize piezo-driven devices of the same kind of those studied theoretically in this paper. Figure 2.5 shows the variations of the coupled structural frequency (black line) and of the Helmholtz one (orange line) as functions of the dimensionless chamber height.

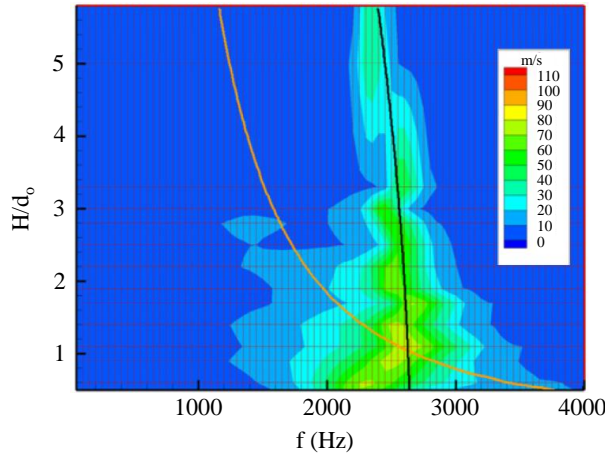


Figure 2.5: Plan view of SJ response as a function of the dimensionless chamber height H/d_o for fixed orifice length and voltage. Reprinted from [59].

These results will be further discussed in paragraph 3.1 in connection with comparisons with experimental findings.

It is interesting to observe that some experimentalists, including the present author, do not measure the jet velocity at the orifice section, but about one-diameter downstream of the exit, i.e. approximately at the stag-

nation point (named also saddle point), by means of a rather simple Pitot tube. To understand the correlation between the saddle point velocity and the orifice (centerline) peak velocity, it is convenient to recall some characteristic quantities of the device. Since the jet formation is related to the ability of the vortex ring produced in the ejection phase to escape during the ingestion phase, a parameter characterizing the jet strength is the so called stroke length \bar{L} , namely the integral of the spatially averaged velocity at the orifice exit over the cycle ejection phase only:

$$\bar{L} = \int_0^{T/2} U(t) dt \quad (2.19)$$

where T is the actuation period. A proper reference velocity is introduced via the relation $\bar{U} = \bar{L}/T$ or, in other terms, as:

$$\bar{U} = \frac{1}{T} \int_0^{T/2} U(t) dt \quad (2.20)$$

which is usually referred to as stroke length velocity. According to classic literature findings (Smith and Glezer (1998) [38] and Smith and Glezer (2002) [25]), the saddle point velocity, U_e , is roughly ≈ 1.1 times the stroke length velocity, which in turn, for sinusoidal time variation of the exit velocity, is related to its peak value by $\bar{U} = U_{\max}/\pi$. Thus, to compare experimental measurements to numerical computations of the peak value U_{\max} , the following relationship is used:

$$U_e = 1.1 \frac{U_{\max}}{\pi} \quad (2.21)$$

The frequency response of SJ actuator is presented very often in terms of saddle point velocity, as will be hereafter reported when discussing overall data of literature.

It is worth to observe that in the fluid dynamic LEM approach the time dependent governing equations constitute an initial value problem to be integrated numerically by means of more or less standard numerical schemes such as Runge-Kutta methods. Details about the numerical procedure are reported in Sharma [54] and de Luca et al. [55]. Here, the numerical simu-

lations are carried out in MATLAB environment with *ode45* routine. Initial conditions of $x_w = 0$, $V_w = 0$, $p_i = 0$ and $U = 0$ are assumed in the computations. It has been observed that the quasi-steady oscillatory solution is generally reached in about 20-30 cycles. Typical values of the electroacoustic transduction coefficient Φ_a that best fit the continuous numerical curves to the velocity measurements range from 40 to 150 Pa/V, depending on the actuator under consideration. Such values are compatible with physical values reported by Gallas et al. [46] and Prasad et al. [47].

2.2.2 Analytical stationary solution

It has been already observed that the LEM modeling based on the electric circuit analogy yields basically the periodic stationary solution. The LEM electric analogy will be treated in the next section. Hereafter, an analytical *modal* approach to obtain the stationary solution of the jet velocity will be described, starting from the LEM fluid dynamics equations. Note that, in spite of the presence of the nonlinear damping term in the acoustic oscillator model, Equation (2.11), the *modal* approach is successful because the non-linearity is represented by the modulus of the unknown U . The following development represents an original reformulation of the previous one reported in de Luca et al. (2016) [60], including a specific evaluation of the magnification factor in resonance conditions, as well as some asymptotic estimates.

The dynamic model constituted by Equations (2.11) and (2.13) can be conveniently rewritten as:

$$\begin{bmatrix} \ddot{V}_w \\ U \end{bmatrix} + \begin{bmatrix} 2\zeta_w\omega_w & 0 \\ 0 & \frac{K}{l_e}|U| \end{bmatrix} \begin{bmatrix} \dot{V}_w \\ U \end{bmatrix} + \begin{bmatrix} \frac{1}{m_{wt}} & 0 \\ 0 & \frac{1}{m_a} \end{bmatrix} \begin{bmatrix} V_w \\ U \end{bmatrix} = \begin{bmatrix} \frac{F_0}{m_{wt}}\omega \cos \omega t \\ 0 \end{bmatrix} \quad (2.22)$$

Equation (2.22) is representative of a canonical damped spring-mass oscillators system, with the peculiar feature of having a non-linear damping

factor. Note also that the *stiffness matrix* is explicitly shown, see Equations (2.12) and (2.14). A graphical representation of this system is provided in Figure 2.6, where $k'_w = \frac{\gamma p_a}{V_c} A_w^2$, $k_{wH} = k_{Hw} = \frac{\gamma p_a}{V_c} A_0 A_w$, and $k_H = \frac{\gamma p_a}{V_c} A_0^2$.

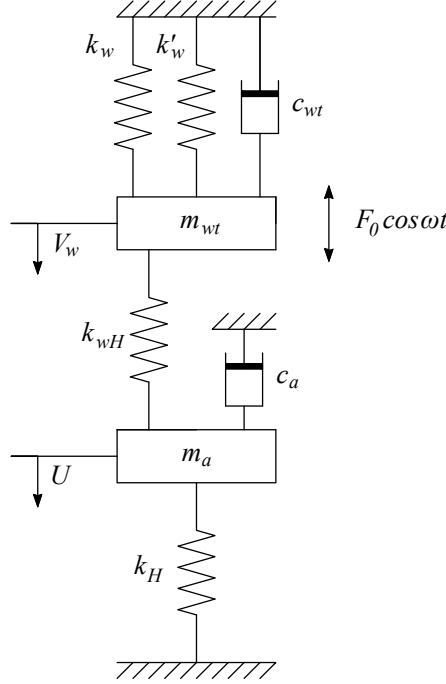


Figure 2.6: Forced damped spring-mass schematic of SJ actuator.

Steady-state solutions can be sought by introducing the *normal mode* assumption:

$$\begin{bmatrix} V_w \\ U \end{bmatrix} = \begin{bmatrix} \tilde{V}_w \\ \tilde{U} \end{bmatrix} e^{j\omega t} \quad (2.23)$$

where \tilde{V}_w and \tilde{U} are complex quantities. Also, $\frac{F_0}{m_{wt}} e^{j\omega t}$ is substituted to $\frac{F_0}{m_{wt}} \omega \cos \omega t$. It is worth to note that $|\tilde{U}| \equiv U_{\max}$.

The resulting algebraic, non-linear system can be implicitly solved to give the *amplification factor* of the maximum jet velocity with respect to the incompressible velocity, $U_{\text{inc}} = (A_w/A_0) \omega \Delta x_w$. Upon back-substitution of the undamped (coupled) resonance frequencies $\omega_{1,2}$, Equation (2.15), one

obtains:

$$\frac{U_{\max}}{U_{\text{inc}}} = \frac{1}{\sqrt{\left[2\zeta_w \frac{\omega}{\omega_w} \delta_H + 2\zeta_U \frac{\omega}{\omega_H} \delta_{CF}\right]^2 + \left[\delta_1 \delta_2 + 4\zeta_w \zeta_U \frac{\omega}{\omega_w} \frac{\omega}{\omega_H}\right]^2}} \quad (2.24)$$

where the known relationship $\omega_1 \omega_2 = \omega_H \omega_w$ has been acknowledged, $\delta_{(\cdot)} = \left(1 - \omega^2 / \omega_{(\cdot)}^2\right)$, $\delta_{CF} = (1 + CF - \omega^2 / \omega_w^2)$, and CF is defined as the *coupling factor* of the two oscillators:

$$CF = \frac{\omega_{wc}^2}{\omega_w^2} \quad (2.25)$$

Also, ζ_w and $\zeta_U = (U_{\max} K) / (2\omega_H l_e)$ are the non-dimensional structural and fluid dynamic (or acoustic) damping factors respectively. Furthermore, observe that the dimensionless frequency ω / ω_H can be related to the operation Strouhal number, which will be introduced in next paragraph 2.3. Since the Equation (2.24) is still implicit in U_{\max} , it has to be solved numerically to obtain the analytical stationary solution of the jet velocity as a function of the operating frequency ω . Some of these solutions will be reported in paragraph 2.4, when discussing comparisons of LEM results available for different tested devices.

Various simplified relationships can be derived starting from the basic Equation (2.24), which can be used to confirm the numerical predictions presented in paragraph 3.1. For instance, in the case of uncoupled oscillators ($CF = 0$), $\omega_1 \equiv \omega_H$ and $\omega_2 \equiv \omega_w$, thus Equation (2.24) becomes:

$$\frac{U_{\max}}{U_{\text{inc}}} \Big|^{CF=0} = \frac{1}{\sqrt{\left[2\zeta_w \frac{\omega}{\omega_w} \delta_H + 2\zeta_U \frac{\omega}{\omega_H} \delta_w\right]^2 + \left[\delta_H \delta_w + 4\zeta_w \zeta_U \frac{\omega}{\omega_w} \frac{\omega}{\omega_H}\right]^2}} \quad (2.26)$$

The amplification factor can be conveniently evaluated in correspondence of the resonance frequencies. In particular, when the system is driven at

$\omega = \omega_w$, one obtains:

$$\frac{U_{max}}{U_{inc}} \Big|_{\omega=\omega_w}^{CF=0} = \frac{1}{2\zeta_w \sqrt{\left(1 - \frac{\omega_w^2}{\omega_H^2}\right)^2 + \left(2\zeta_U \frac{\omega_w}{\omega_H}\right)^2}} \quad (2.27)$$

while a perfectly specular expression can be obtained when $\omega = \omega_H$

$$\frac{U_{max}}{U_{inc}} \Big|_{\omega=\omega_H}^{CF=0} = \frac{1}{2\zeta_U \sqrt{\left(1 - \frac{\omega_H^2}{\omega_w^2}\right)^2 + \left(2\zeta_w \frac{\omega_H}{\omega_w}\right)^2}} \quad (2.28)$$

Note that Equations (2.27) and (2.28) resemble very closely the canonical response of a damped spring-mass oscillator and that the ratio ω_H/ω_w can be related to the CF parameter introduced before. Equation (2.27) can be rearranged to give a compact closed-form expression for the amplification factor

$$\frac{U_{max}^2}{U_{inc}^2} \Big|_{\omega=\omega_w}^{CF=0} = \frac{-\zeta_w^2 (1 - \beta^2)^2 + \sqrt{\zeta_w^4 (1 - \beta^2)^4 + 4\zeta_w^2 \zeta_{U_{inc}}^2 \beta^2}}{8\zeta_w^2 \zeta_{U_{inc}}^2 \beta^2} \quad (2.29)$$

where $\beta = \frac{\omega_w}{\omega_H}$ and $\zeta_{U_{inc}} = \frac{KU_{inc}}{2\omega_H l_e}$. The amplification factor given in Equation (2.29) depends exclusively on three non-dimensional parameters: β , ζ_w , and $\zeta_{U_{inc}}$. Since the structural damping factor is typically equal to 0.03, the acoustic damping and the resonance frequencies ratio can be used as free design parameters to optimize the actuator response. In Figure 2.7, Equation (2.29) is plotted as a function of β for three values of $\zeta_{U_{inc}}$. Apparently, for very small coupling factors and in the (common) case of $\omega = \omega_w$, it is convenient to design the actuator so to have a small resonance frequencies ratio and (clearly) as small acoustic damping factors as possible. Also, Figure 2.7 shows that for the cases here analyzed, an actuator having β higher than about 4 is inconvenient since no amplification occurs. However, the above reasoning has to be augmented with efficiency considerations that will be made in paragraph 3.2.

Phase angles (with respect to the input supply) can also be computed.

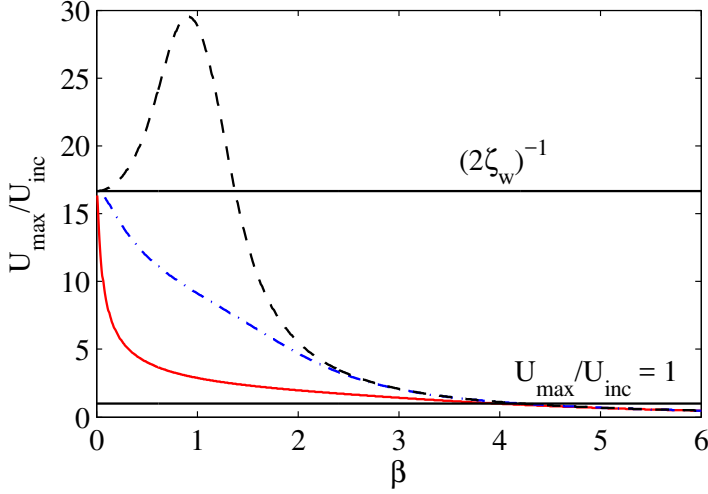


Figure 2.7: Amplification factor of jet peak velocity for decoupled oscillators ($CF = 0$) and $\omega = \omega_w$, Equation (2.29). Continuous red line is for $\zeta_{U_{inc}} = 1$, dotted-dashed blue line for $\zeta_{U_{inc}} = 0.1$, dashed black line for $\zeta_{U_{inc}} = 0.01$.

The diaphragm velocity phase angle ϕ_{V_w} reads:

$$\phi_{V_w} = \tan^{-1} \left[\frac{2\zeta_w \frac{\omega}{\omega_w} \delta_H^2 + 2\zeta_U \frac{\omega}{\omega_H} \delta_H \delta_{CF} + 2\zeta_U \frac{\omega}{\omega_H} \delta_1 \delta_2 + 8\zeta_w \zeta_U^2 \frac{\omega}{\omega_w} \frac{\omega^2}{\omega_H^2}}{\delta_1 \delta_2 \delta_H - 4\zeta_U^2 \frac{\omega^2}{\omega_H^2} \delta_{CF}} \right] \quad (2.30)$$

Additional insights can be obtained by again considering $CF = 0$,

$$\phi_{V_w}|^{CF=0} = \tan^{-1} \left[\frac{2\zeta_w \frac{\omega}{\omega_w} \delta_H^2 + 4\zeta_U \frac{\omega}{\omega_H} \delta_H \delta_w + 8\zeta_w \zeta_U^2 \frac{\omega}{\omega_w} \frac{\omega^2}{\omega_H^2}}{\delta_w \delta_H^2 - 4\zeta_U^2 \frac{\omega^2}{\omega_H^2} \delta_w} \right] \quad (2.31)$$

It is easy to check from Equation (2.31) that when the diaphragm is driven at the structural resonance frequency, i.e. $\omega = \omega_w$, the phase angle of the

diaphragm equals $\pi/2$,

$$\phi_{V_w}|_{\omega=\omega_w}^{CF=0} = \frac{\pi}{2} \quad (2.32)$$

For what concerns the phase angle of the jet velocity, its general expression reads

$$\phi_U = \tan^{-1} \left[\frac{2\zeta_w \frac{\omega}{\omega_w} \delta_H + 2\zeta_U \frac{\omega}{\omega_H} \delta_{CF}}{\delta_1 \delta_2 + 4\zeta_w \zeta_U \frac{\omega}{\omega_w} \frac{\omega}{\omega_H}} \right] \quad (2.33)$$

Again, under the hypothesis of decoupled oscillators, one has:

$$\phi_U|_{\omega=\omega_w}^{CF=0} = \tan^{-1} \left[\frac{2\zeta_w \frac{\omega}{\omega_w} \delta_H + 2\zeta_U \frac{\omega}{\omega_H} \delta_w}{\delta_w \delta_H + 4\zeta_w \zeta_U \frac{\omega}{\omega_w} \frac{\omega}{\omega_H}} \right] \quad (2.34)$$

The phase angle occurring when the system is driven at $\omega = \omega_w$ reads:

$$\phi_U|_{\omega=\omega_w}^{CF=0} = \tan^{-1} \left[\frac{1 - \beta^2}{2\zeta_U \beta} \right] \quad (2.35)$$

Upon inspection of Equations. (2.31)-(2.35), several considerations can be drawn for the common case in which the system is driven at the structural resonance frequency:

- if the structural resonance frequency equals the Helmholtz frequency (i.e., $\beta = 1$), there is a $\pi/2$ phase difference between the diaphragm and the jet,

$$[\phi_{V_w} - \phi_U]_{\omega=\omega_w}^{CF=0} = \frac{\pi}{2} \quad \beta = 1 \quad (2.36)$$

- if the structural frequency is much higher than the resonance frequency ($\beta \gg 1$), then:

$$\lim_{\beta \rightarrow +\infty} \phi_U|_{\omega=\omega_w}^{CF=0} = -\frac{\pi}{2} \quad (2.37)$$

and the diaphragm and the jet are out of phase by π

$$[\phi_{V_w} - \phi_U]_{\omega=\omega_w}^{CF=0} = \pi \quad \beta \gg 1 \quad (2.38)$$

- if the structural resonance frequency is very small ($\beta \ll 1$), then the compressible effects are negligible and the diaphragm and the jet are

in phase with each other:

$$[\phi_{V_w} - \phi_U]_{\omega=\omega_w}^{CF=0} = 0 \quad \beta \ll 1 \quad (2.39)$$

Similar considerations can be drawn for the general expressions given in Equations (2.30)-(2.33), for the limiting cases in which the system is driven at very low or very high frequencies, i.e., $\omega/\omega_H \ll 1$ or $\omega/\omega_H \gg 1$. The above results are in close qualitative agreement with the results obtained by Sharma [54] and reported in Figure 2.8.

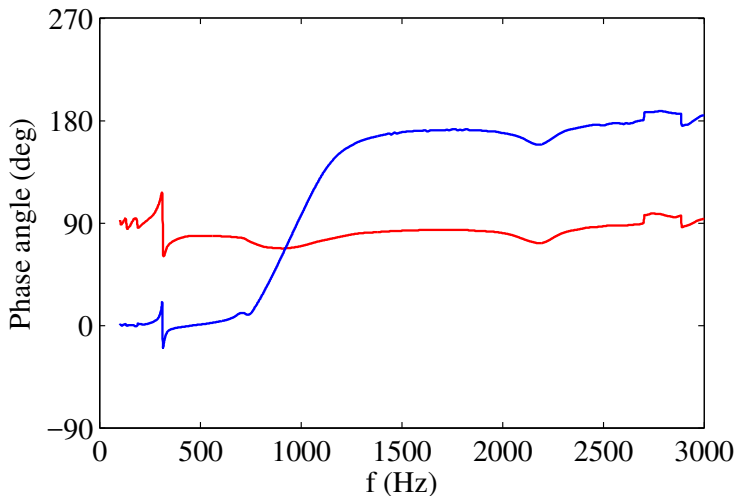


Figure 2.8: Computed phase angles for case 1 device of Gallas et al. [46]. Blue line refers to jet velocity - diaphragm velocity responses; red line to jet velocity - cavity pressure responses. Reprinted from [54].

2.2.3 Transduction approach

A useful tool to study the behavior of an actuator, once it has been represented into a lumped mechanical system (basically including the oscillating diaphragm, the cavity and the orifice), consists in using the electro-mechanical analogy. This method considers the construction of an equivalent circuit in which an inductor represents the lumped mass (essentially the diaphragm), a capacitor reproduces the effects of the compliance (represent-

ing the elasticity of both the diaphragm and air), and a resistor symbolizes the damper (representing the structural and fluidic dissipation causes). In LEM formulation, these basic elements are able to exchange energy among themselves. In general, different energy domains can be introduced, and for each one, an effort $e(t)$ and a flow $f(t)$ are conveniently defined, see Mohseni and Mittal [40] and Senturia [61]. The power flow from one element to the other is given by the product of the effort by the corresponding flow. A useful correspondence for SJ devices is listed in Table 2.1.

Energy domain	Effort, $e(t)$	Flow, $f(t)$
Mechanical	Force, F	Velocity, U
Mechanical	Pressure, p_i	Volumetric flow rate, Q
Electrical	Voltage, V_{ac}	Current, I

Table 2.1: Typical effort and flow variables.

A synthetic jet actuator is an electroacoustic device which involves different forms of energy, such as, electrical (input power), electrodynamical (stored in the diaphragm) and kinetic (of the air jet), Girfoglio et al. [62]. Following the work of Gallas [46], the changes between these different forms can be analyzed by using a two-port network where elements sharing a common effort (i.e. pressure or voltage) are connected in parallel, whereas those sharing a common flow (i.e. air volumetric flow rate or current) are connected in series. Therefore, the problem concerns the representation of these elements in the acoustic/fluidic domain and the determination of the corresponding electric impedances in the electric one. In LEM formulation, a device can be represented by two-coupled lumped mechanical systems (both of mass-spring-damper type), namely the diaphragm and the cavity/orifice, in which the kinetic energy is associated to a lumped mass m , the potential energy to a lumped spring of stiffness k (or compliance, $C = A^2/k$, according to Equation (2.9)) and the dissipation to a lumped dumper of coefficient c , as sketched in Figure 2.6. For the sake of clarity the reader is referred also to Equation (2.22). In case the SJ is realized with an electromechanical element, such as a piezoelectric thin disk, the equivalent electric circuit is depicted in Figure 2.9, which corresponds strictly to the

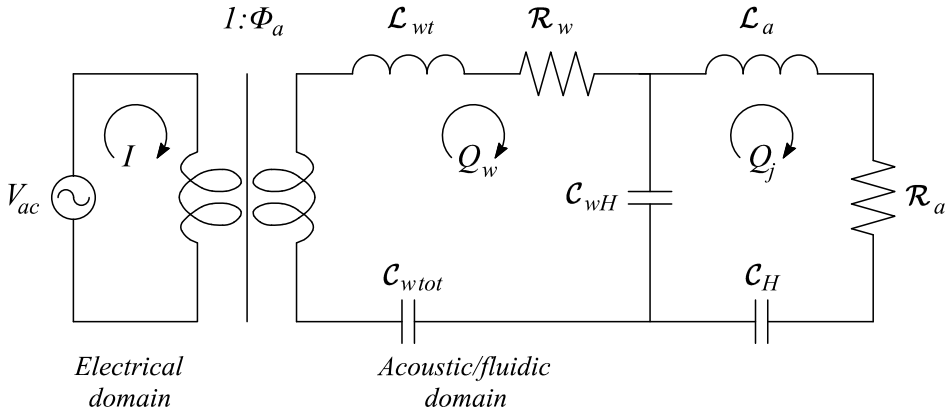


Figure 2.9: Electro-mechanical analogy.

mechanical system of Figure 2.6, where the transduction from the electrical to the acoustic/fluidic domain is represented through an ideal transformer, having the transformation ratio equal to the electroacoustic transduction coefficient, Φ_a . Within the framework of the mass-inductance analogy, the inductances \mathcal{L}_w and \mathcal{L}_a correspond to the diaphragm and orifice air masses, respectively, the capacitances \mathcal{C}_{wtot} , \mathcal{C}_{wH} and \mathcal{C}_H correspond to the total diaphragm stiffness (including both parallel structural and acoustic stiffnesses, k_w and k'_w , respectively), the coupling stiffness and the Helmholtz stiffness, respectively, and the resistances \mathcal{R}_w and \mathcal{R}_a correspond to the structural and fluidic damping factors, respectively.

In fact, for an ideal transformer with unit electrodynamic transduction efficiency, i.e. the Joule power provided to the piezo-element equals the electrodynamic power (detailed insights on the actuators energy efficiency will be discussed in paragraph 3.2), it holds:

$$V_{ac}I = F\dot{x}_w \quad (2.40)$$

which can be also written in terms of cavity pressure and wall volumetric flow rate $Q_w = \dot{x}_w A_w$

$$V_{ac}I = p_i Q_w \quad (2.41)$$

By taking into account that the driving force magnitude is expressed by Equation (2.4), and by considering the relationships given in Equations (2.7) and (2.9), one obtains finally

$$p_i/V_{ac} = \Phi_a \quad (2.42)$$

As already stated above, the solution to the electric LEM equations is usually expressed in terms of periodic stationary behavior of the actuator, where the ratio of the output air jet flow rate to the input voltage is given by the equivalent impedance. With reference to Figure 2.9, and following Gallas et al. [46], denoted with Z_w , Z_c , and Z_o the total impedances of the diaphragm, cavity, and orifice respectively, one obtains:

$$\frac{Q_j}{V_{ac}} = \frac{Z_c}{Z_w Z_o + Z_w Z_c + Z_c Z_o} \quad (2.43)$$

where Q_j is the volumetric flow rate of air issuing from the orifice (i.e., corresponding to the air jet velocity U). A major goal of the device design is to maximize the magnitude of the volumetric flow rate through the orifice per applied voltage, $|Q_j/V_{ac}|$. It has to be stressed that for the approach followed in the present paper the relevant impedances are directly related to the mechanical quantities defined, for instance, in Figure 2.6; however, within the equivalent circuit model analysis, such impedances are evaluated in a specific way component by component, as made by Gallas et al. [46] and Mohseni and Mittal [40]. The way in which the electric circuit LEMs evaluate the impedances makes these approaches different from the fluid dynamic-based LEMs.

Starting from Equation (2.43) it is possible in principle to calculate the coupled resonance frequencies of the system. This analysis has been performed by Gallas et al. [46], who developed a non-closed form procedure to obtain such frequencies, under the assumption of small damping effects, and compared the computed frequencies with experimental data, as well as with the corresponding uncoupled values. The approach of Gallas et al. [46] is based on the already mentioned relationship $\omega_1 \omega_2 = \omega_w \omega_H$, where ω_1 and ω_2 are the coupled natural frequencies. The reader is referred to the original paper to obtain more details. Note that the Equation (2.15),

in agreement with the constraint of Gallas et al. [46], predicts that the coupling effect augments the greatest uncoupled frequency and reduces the lowest one. Additional information about the evaluation of the two modified resonance frequencies can be found in Persoons [48], who employed a simplified heuristic argument and referred to loudspeaker-driven actuators.

2.3 Dimensionless equations

With the aim of providing further insights to the problem physics, the governing equations analyzed previously can be recast into a convenient dimensionless form.

The nondimensionalization process relies on the choice of proper reference scales for time, length and velocity; for the equation of dynamics of the acoustic oscillator, Equation (2.11), a convenient set of quantities is represented by the reciprocal of the operating frequency $1/\omega$, the cavity height H and the air speed of sound c , respectively. The nondimensional form of the equation is thus

$$St^2 \left(\frac{l_e}{H} \right) \frac{d^2 U^*}{dt^{*2}} + St (K|U^*|) \frac{dU^*}{dt^*} = V_w^* - \frac{A_o}{A_w} U^* \quad (2.44)$$

where the Strouhal number, defined as:

$$St = \frac{\omega H}{c} \quad (2.45)$$

can be re-written in function of other parameters:

$$St = \frac{\omega}{\omega_H} \frac{d_o}{d_w} \sqrt{\frac{H}{l_e}} \quad (2.46)$$

The condition $St \ll 1$ represents the case of acoustically thin cavity, for which the traveling time of a small pressure disturbance, over the distance H , is much smaller than the reference time $1/\omega$. From an operative point of view, the air inside the cavity behaves as an incompressible medium (i.e., the air stiffness is infinite), and Equation (2.44) in this case reduces to the (dimensional) relationship:

$$A_w V_w = A_o U \quad (2.47)$$

This means that the volume flow rate entering the cavity, as a consequence of the diaphragm displacement, equals the volume flow rate of air expelled through the orifice. On the other hand, Equation (2.1) shows that the diaphragm dynamics is decoupled from that of the acoustic oscillator, with the diaphragm being driven by the piezoelectric forcing only. One can easily verify this result by examining the electric circuit of Figure 2.9, for a null air capacitance (or null air elastic compliance). When $St \ll 1$, once the air velocity at the orifice has been obtained from Equation (2.47), the cavity pressure may be evaluated by using the unsteady form of the Bernoulli's equation. In the following, one will refer to Equation (2.47) as the *incompressible model* of operation.

It is also convenient to observe that, for small concentrated head losses, the driving differential pressure p_i has to be of the same order as the dynamic pressure at the orifice in the Bernoulli's equation, that allows the determination of a more appropriate scale velocity of the orifice jet, U_{ref} . Since, through the isentropic transformation of perfect gas, the pressure variation related to the orifice volume variation $A_o dx$, with dx being the axial variation scaling with l_e , scales with $\gamma \frac{p_o}{V_c} A_o l_e$, one finally obtains $U_{ref} = c \frac{d_o}{d_w} \sqrt{\frac{l_e}{H}}$. As a consequence, it is easy to verify that the Strouhal number is directly represented by the ratio $St = \frac{\omega}{\omega_H}$, namely formally by $St = \frac{\omega l_e}{U_{ref}}$.

Another relevant condition occurs for $St \gg 1$, which also corresponds to decoupled diaphragm dynamics. In this case the air stiffness is vanishing, the pressure field inside the cavity is practically unperturbed, and therefore the air jet velocity U is vanishing too. Again one can uncover this situation by taking a look at Figure 2.9. It worth noting that for this condition the lumped assumption is of course invalid, hence it has not been considered during the device performance evaluation (Chapter 3).

Equation (2.13) is made dimensionless with the introduction of different time and velocity scales; here, convenient choices are $1/\omega_w$ and $\omega \Delta x_w$, respectively. The non-dimensional form of such an equation is:

$$Re = \frac{\bar{U}d_o}{\nu} \quad S = \frac{\omega d_o^2}{\nu} \quad \frac{d_o}{d_w} \quad \frac{H}{d_o} \quad \frac{l_e}{H} \quad \frac{m_c}{m_{wt}} \quad CF = \frac{\omega_{wc}^2}{\omega_w^2} \quad St = \frac{\omega H}{c}$$

Table 2.2: Basic dimensionless variables of the problem.

$$\ddot{V}_w^* + 2\zeta_w \dot{V}_w^* + V_w^* + CF \left(V_w^* - \frac{A_o}{A_w} U^* \right) = \cos \omega t \quad (2.48)$$

where the coupling parameter CF has been introduced in Equation (2.25). Note that under the condition $CF \ll 1$ (which means that the air stiffness is negligible in comparison with the diaphragm stiffness) the diaphragm dynamics is decoupled from the acoustic oscillator one. In this case the jet velocity and the cavity pressure are determined via the continuity and the unsteady Bernoulli's equations. Furthermore, the modified structural and Helmholtz's frequencies tend to coincide with the corresponding uncoupled frequencies, as one may verify by inspecting Equation (2.15). It has to be also stressed that, in general, the coupling effects represented by the CF parameter refer to a certain device and may be neglected on the basis of design characteristics of the actuator, whatever is the operating condition. On the contrary, the conditions of decoupling occurring for $St \ll 1$ depend basically on the operating condition and may occur for any device.

The inclusion of the effects of the external viscous medium (air) leads to the introduction of the jet Reynolds and Stokes numbers (e.g., Smith and Glezer [25]), $Re = \frac{\bar{U}d_o}{\nu}$ and $S = \frac{\omega d_o^2}{\nu}$, as indicated in Table 2.2, which summarizes all the nondimensional parameters affecting the actuator operation (with d_o and d_w being the orifice diameter and the diaphragm diameter, respectively).

2.4 Comparison of LEM results

Very interesting comparisons of LEM results obtained by means of both the mechanical and electric approach were showed by Sharma [54], who computed the frequency response of the devices tested by Gallas et al. [46], and compared his results to the stationary solutions of the same work, obtained applying directly the method of the electrical impedances. Therefore, the

comparison is meaningful because the models of Sharma [54] and Gallas et al. [46] are quite different, but they were applied to the very same physical system. Figure 2.10 depicts the centerline maximum jet velocity (achieved during the periodic stationary operation phase) as a function of the operating frequency of two different actuators, named case 1 and case 2 of Gallas et al. [46], who made use of a Dantec two-component laser Doppler Velocimetry system to measure the peak centerline jet velocity U_{\max} . These authors took care of measuring the jet velocity at an axial station very close to the orifice, or in other terms, such that the ratio of the measurement location to the stroke length was much less than unity. As a consequence, they could compare directly the measured peak velocity to U_{\max} provided by LEM. Very interesting comparisons of LEM results obtained by means of both the mechanical and electric approach were showed by Sharma [54], who computed the frequency response of the devices tested by Gallas et al. [46], and compared his results to the stationary solutions of Gallas et al. [46], obtained applying directly the method of the electrical impedances. Therefore, the comparison is meaningful because the models of Sharma [54] and Gallas et al. [46] are quite different, but they were applied to the very same physical system. Figure 2.10 depicts the centerline maximum jet velocity (achieved during the periodic stationary operation phase) as a function of the operating frequency of two different actuators, named case 1 and case 2 of Gallas et al. [46], who made use of a Dantec two-component laser Doppler Velocimetry system to measure the peak centerline jet velocity U_{\max} . These authors took care of measuring the jet velocity at an axial station very close to the orifice, or in other terms, such that the ratio of the measurement location to the stroke length was much less than unity. As a consequence, they could compare directly the measured peak velocity to U_{\max} provided by LEM.

Note that both models well reproduce the experimental data concerned with the two resonance frequencies and the corresponding velocity peaks, although in the case of device 1 the numerical findings overestimate the experimental data points in between the two peak frequencies. For the case of device 2 two resonance frequencies are predicted by the electrical LEM, one near 350 Hz and the other one near 900 Hz. However, the lower peak is

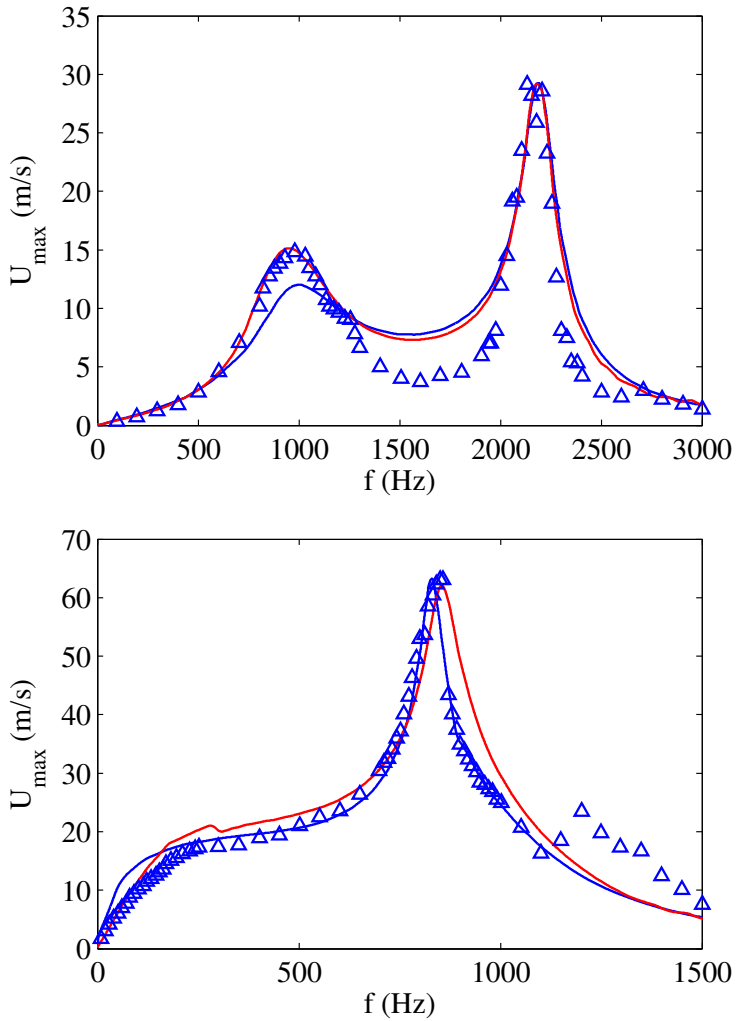


Figure 2.10: Comparison of experimental data and LEMs results of peak jet velocity for two actuators, reprinted from [54]. Blue markers are experimental data from Gallas et al. [46], blue line represents LEM by Gallas et al. [46], red line LEM by Sharma [54]. Left frame is for case 1, right for case 2.

heavily damped due to the nonlinear fluidic damping acting on the acoustic oscillator. The major geometrical and electro-mechanical characteristics of the devices designed by Gallas et al. [46] are shown in Table 2.3.

Figure 2.11 reports other comparisons for two house-made devices with the shim in brass, frame (a), and aluminum, frame (b), respectively. Each picture compares the experimental data with the findings obtained by means of the fully fluid dynamics modeling (where the stationary solution was obtained by integrating the governing equations for long times), as well as with the *modal* stationary solution, that is an equivalent form of the electric LEM approach. In this case, however, the impedances are obtained from the fluid dynamics approach.

The experimental mock-up is reported in Figure 2.12, showing in particular the Pitot tube (Kanomax mini Pitot tube, 1/8 in in diameter and 6 in in length) employed to measure the jet velocity. Exit jet velocities were measured in the external ambient at the saddle point, therefore in this study velocity experimental measurements U_e and LEM predictions of peak jet velocity U_{\max} were correlated to each other by means of the relationship of Equation (2.21). The Pitot tube was connected with a Mouser pressure transducer whose output signal was phase-locked to the device excitation signal over typically 20 periods to obtain an uncertainty estimate of the jet velocity within 5%, computed with the standard procedures suggested in specialized literature, Moffat [63]. The agreement between numerical and analytical solutions is fully satisfactory for the brass shim, while for the aluminum shim actuator one can note again an over-prediction of the theoretical results with respect to the experimental data at intermediate frequencies. The geometrical and electro-mechanical characteristics of the devices designed for this purpose are shown in Table 2.4.

	Case 1	Case 2
Geometry		
Shim diameter (mm)	23	37
Shim thickness (mm)	0.15	0.10
Piezo-electric diameter (mm)	20	25
Piezo-electric thickness (mm)	0.08	0.11
Cavity diameter (mm)	23	37
Cavity height (mm)	5.76	4.65
Orifice diameter (mm)	1.65	0.84
Orifice length (mm)	1.65	0.84
H/d_o	3.5	5.5
l_e/d_o	1	1
Shim		
Young's Module (Pa)	8.963×10^{10}	8.963×10^{10}
Poisson's Module	0.324	0.324
Density (Kg/m ³)	8700	8700
Piezo-electric		
Young's Module (Pa)	6.3×10^{10}	6.3×10^{10}
Poisson's Module	0.31	0.31
Density (Kg/m ³)	7700	7700
Frequency response		
f_w (Hz)	2114	632
f_1 (Hz)	2167	324
f_H (Hz)	941	452
f_2 (Hz)	918	880
CF	0.07	2.85

Table 2.3: Features of the devices studied by Gallas et al. [46].

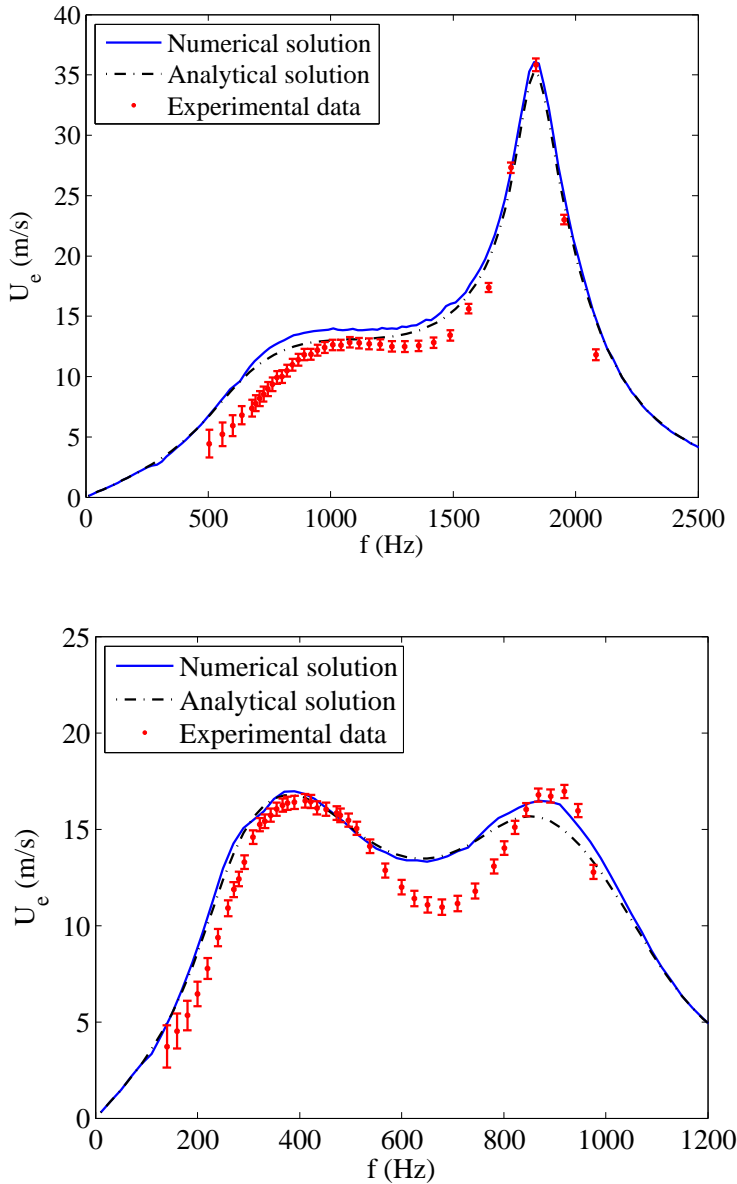


Figure 2.11: Numerical, analytical and experimental comparison of average exit flow velocity for a Brass actuator (a, $H/d_o = 0.75$, $V_{ac} = 50V$) and for an Aluminum actuator (b, $H/d_o = 0.8$, $V_{ac} = 50V$).

	Brass	Aluminum
Geometry		
Shim diameter (mm)	41	80
Shim thickness (mm)	0.4	0.25
Piezo-electric diameter (mm)	31.8	63.5
Piezo-electric thickness (mm)	0.191	0.191
Cavity diameter (mm)	41	80
Cavity height (mm)	1.5	4
Orifice diameter (mm)	2	5
Orifice length (mm)	2	2
H/d_o	0.75	0.8
l_e/d_o	1	0.4
Shim		
Young's Module (Pa)	9.7×10^{10}	7.31×10^{10}
Poisson's Module	0.36	0.31
Density (Kg/m ³)	8490	2780
Piezo-electric		
Young's Module (Pa)	6.6×10^{10}	6.6×10^{10}
Poisson's Module	0.31	0.31
Density (Kg/m ³)	8700	7800
Frequency response		
f_w (Hz)	1667	432
f_1 (Hz)	1877	344
f_h (Hz)	1004	752
f_2 (Hz)	891	945
CF	0.19	1.38

Table 2.4: Features of the piezo-driven SJ devices experimentally tested.



Figure 2.12: Experimental mock-up with Pitot tube.

Chapter 3

Piezo-driven synthetic jet actuators: performances

This Chapter is dedicated to the analysis of the major device performances (basically the frequency response in terms of jet velocity), as functions of the main parameters that influence the oscillators coupling, the supply voltage and the effective orifice length. The second paragraph, [3.2](#), contains the analysis of efficiency of SJ actuators, based on a physical model directly related to the energy equations of the two coupled oscillators.

3.1 Performances

The various physical modelings has been validated against experimental measurements and the relevant comparisons have been shown in the previous Chapter [2](#). LEM will be used hereafter to predict the influence of the coupling degree of the two oscillators (via the Strouhal number and the coupling factor CF), and of other parameters such as the supply voltage and the effective orifice length.

3.1.1 Effect of coupling of the oscillators

The effect of the Strouhal number can be appreciated by focusing the attention on particular operating conditions; for a given device the condition of $St \ll 1$, that is achieved for relatively low values of operation frequency,

corresponds to situations of acoustically thin resonant cavity, as before observed. This effect will be analyzed numerically with particular reference to the frequency response in terms of exit velocity of the three devices mentioned in the previous paragraphs.

The maximum exit velocity trends as functions of the operation frequency are depicted in Figures 3.1 and 3.2 for the devices tested, whose characteristics are listed in Table 2.4, and for various dimensionless cavity heights H/d_o . The supply voltage V_a is equal to 35 V in all these simulations.

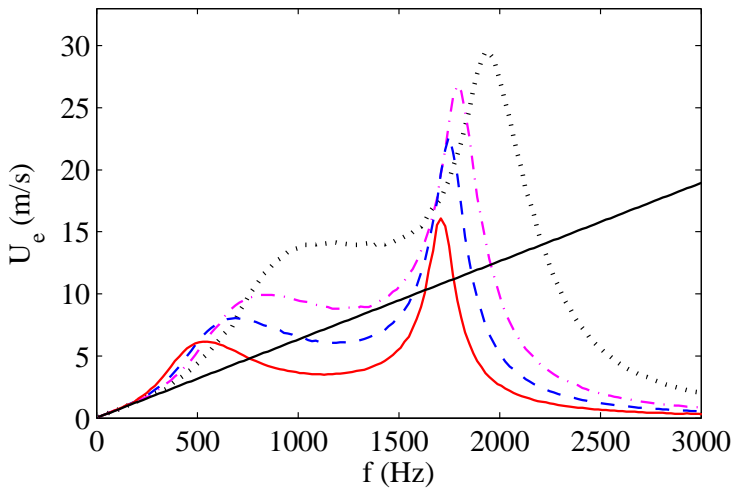


Figure 3.1: Frequency response of saddle point velocity for the Brass actuator at $V_a = 35\text{V}$; black dotted line refers to $H/d_o = 0.5$, magenta dash-dotted line to $H/d_o = 1$, blue dashed line to $H/d_o = 1.5$, red solid line to $H/d_o = 2.5$. The straight line refers to Equation (2.47).

For all the devices, two velocity peaks corresponding to the two resonance frequencies are clearly evident. For the brass device, both velocity peaks increase with decreasing cavity height. The distance between the two resonance frequencies slightly increases with increasing H/d_o , in agreement with experimental results of Gomes et al. [59] obtained for $l_o/d_o > 1$, reported in previous Figure 2.5. Note that the experimental findings of Gomes et al. [59] show also that the distance between the resonance frequencies

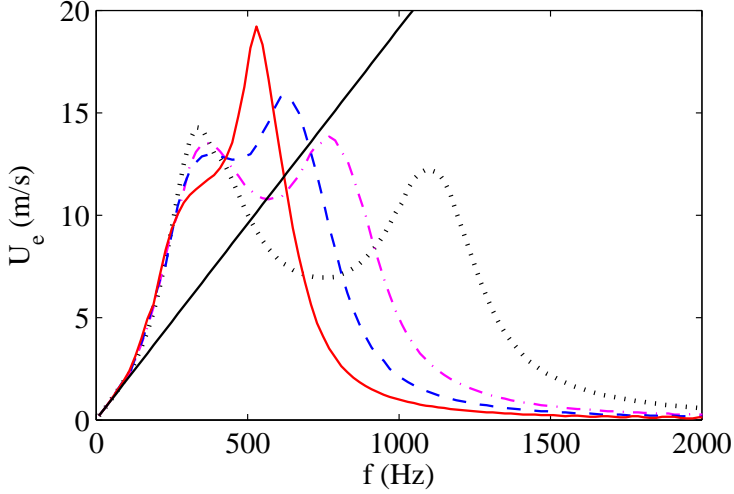


Figure 3.2: Frequency response of saddle point velocity for the Aluminum actuator at $V_a = 35\text{V}$; black dotted line refers to $H/d_o = 0.5$, magenta dash-dotted line to $H/d_o = 1$, blue dashed line to $H/d_o = 1.5$, red solid line to $H/d_o = 2.5$. The straight line refers to Equation (2.47).

becomes practically constant as H/d_0 further increases, in agreement with the Equation 2.18, valid in the case of $\omega_w \gg \omega_H$.

The straight lines present in the plots of Figures 3.1 and 3.2 refer to the linear dependence of the jet velocity upon the operating frequency given by the incompressible model described by the Equation (2.47). For both actuators it is clearly evident that such a simplified model closely agrees with the simulations of the complete model at low frequencies, with the frequencies range of such an agreement widening for the smaller cavity heights, as predicted by the theory for $St \ll 1$. Note also that for this range of frequencies the response in terms of jet velocity is the same whatever is the cavity height, thus confirming that the diaphragm dynamics is decoupled from the acoustic oscillator one.

In order to complete the discussion about the behavior of the aluminum device, note that the two nominal Helmholtz and structural frequencies, which for this actuator are reversed, are remarkably modified by the high coupling ratio. The jet velocity decreases with increasing the cavity height

at the structural resonance frequency, whereas it increases with increasing H/d_o at the Helmholtz resonance frequency, with the result that the maximum peak is reached at the Helmholtz frequency for the highest simulated cavity height. This particular finding agrees with Equation 2.17, that if $\omega_w \ll \omega_H$ then the distance between the two eigenvalues $|\omega_1^2 - \omega_2^2|/\omega_H^2$ does not depend on the cavity height H/d_o and therefore $|\omega_1^2 - \omega_2^2| \simeq 1/(H/d_o)$. The quasi-coincidence of the two resonance frequencies justifies that the maximum peak is reached for the highest cavity height. As already observed, this last result has been confirmed experimentally by Gil and Strzelczyk [64] for the case of loudspeaker driven actuators, as depicted in Figure 3.3. Note that these authors referred to a spatially- and temporally-averaged *momentum velocity* U_o .

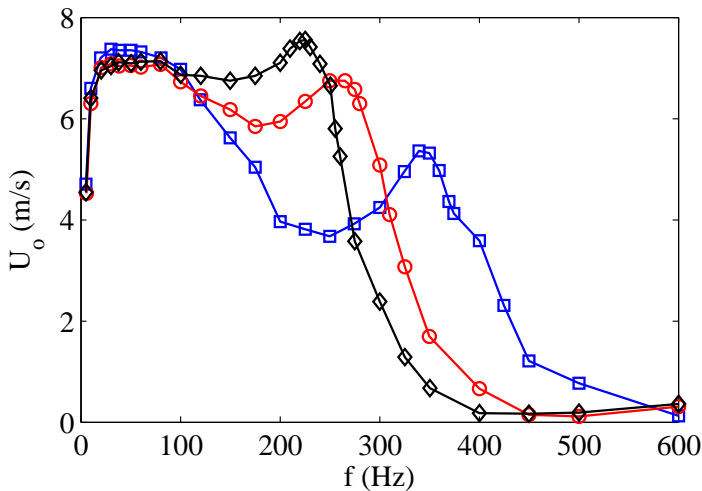


Figure 3.3: Spatially and temporally average *momentum velocity* for various cavity heights. Blue square markers are for $H = 20$ mm, red circles for $H = 40$ mm and black diamonds for $H = 60$ mm. Reprinted from [64].

In the previous paragraph 2.2.2 the magnification of the device response with respect to the so called incompressible solution has been analyzed theoretically, in connection with the role played by the simultaneous presence of damping effects, and in particular that of the nonlinear fluidic term.

By resorting to the classic linear theory of damped-driven harmonic

oscillators, under the simplified assumption of decoupled damping effects, it is possible to define the acoustic oscillator as *under-damped* or *over-damped* depending on whether the acoustics damping coefficient, $ADC = K \left(|\tilde{U}|/l_e \right) / (2\omega_h)$, is less than or greater than unity, respectively. Note that here ADC corresponds to the fluidic damping factor $\zeta_U = (U_{\max}K) / (2\omega_H l_e)$ previously introduced in paragraph 2.2.2. The under-damped case corresponds to the occurrence of resonance amplifications and therefore, if one extends such implications to the present nonlinear case, the jet should clearly form when driven at the Helmholtz frequency. Due to nonlinear effects, the jet velocity U should refer to a proper scaling value, namely to the average value, \tilde{U} , giving the equivalent amount of energy dissipated in a quarter of period by the variable damping coefficient. It is easy to verify that $\tilde{U} = U_{\max}/2$, with U_{\max} denoting the maximum value reached in the cycle. These predictions were qualitatively confirmed by the numerical simulations referring as usual to brass and aluminum actuators. For each device the diaphragm peak velocity, the average jet velocity, and ADC , were shown, as functions of the operating frequency, for various values of the head loss coefficient (mostly non-physical).

Here it should be stressed the crucial role played by the nonlinear flow damping on the amplitude of the oscillations, as is well recognized in the literature, e.g., by Gallas et al. [46] (who attributed to it the absence of the first resonance peak for their device of case 2, see the right frame of Figure 2.10), Persoons [48], Kooijman and Ouweltjes [65]. The diaphragm velocity and the jet velocity of the SJ devices, whose characteristics are reported in Table 2.4, have been represented in Figures 3.4-3.5, which were evaluated by means of the incompressible model of Equation (2.47). Remember that the incompressible model furnishes the reference value to be used to evaluate the amplification of the oscillations amplitude due to the resonance, as discussed in depth in paragraph 2.2.2, where both the structural and fluidic damping effects are simultaneously taken into account, within a generalized nondimensional context.

As far as the Brass device is concerned, Figure 3.4 a) confirms that, due to the vanishing coupling factor, the diaphragm dynamics is decoupled from the acoustic oscillator. In fact, the trends of the diaphragm velocity

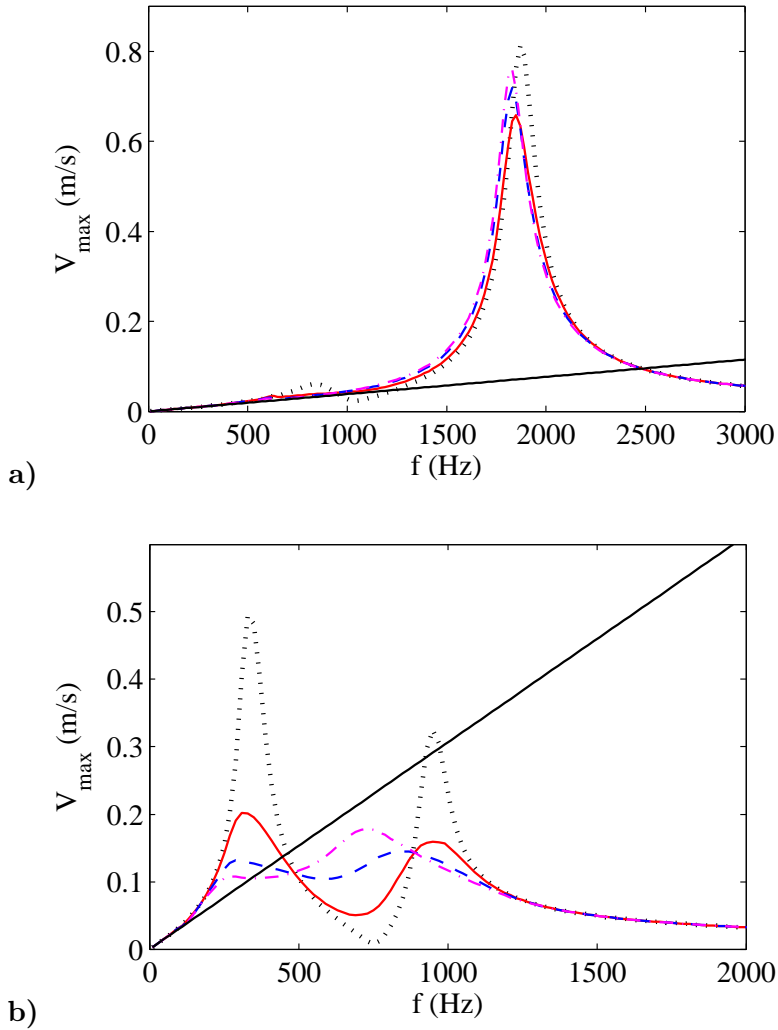


Figure 3.4: Frequency response of diaphragm peak velocity for the Brass actuator a) and the Aluminum device b); black dotted line is for $K = 0.14$, red solid line $K = 1.14$, blue dashed line $K = 3.14$, magenta dash-dotted line $K = 5.14$.

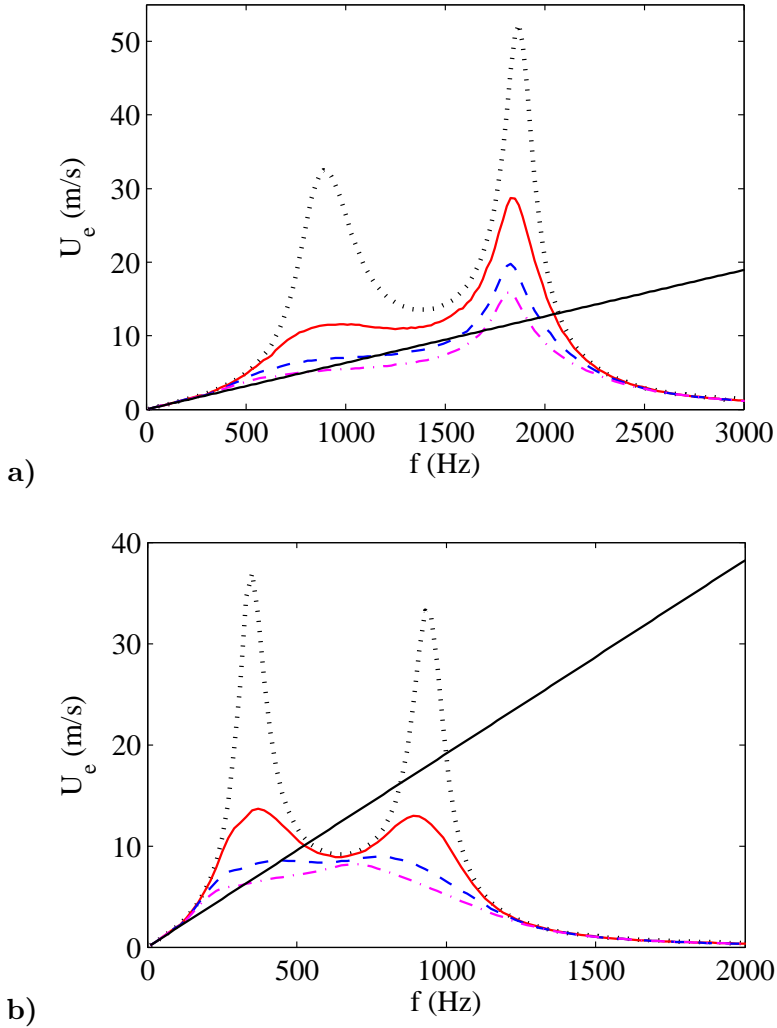


Figure 3.5: Frequency response of average jet velocity for the Brass actuator a) and the Aluminum device b); black dotted line is for $K = 0.14$, red solid line $K = 1.14$, blue dashed line $K = 3.14$, magenta dash-dotted line $K = 5.14$.

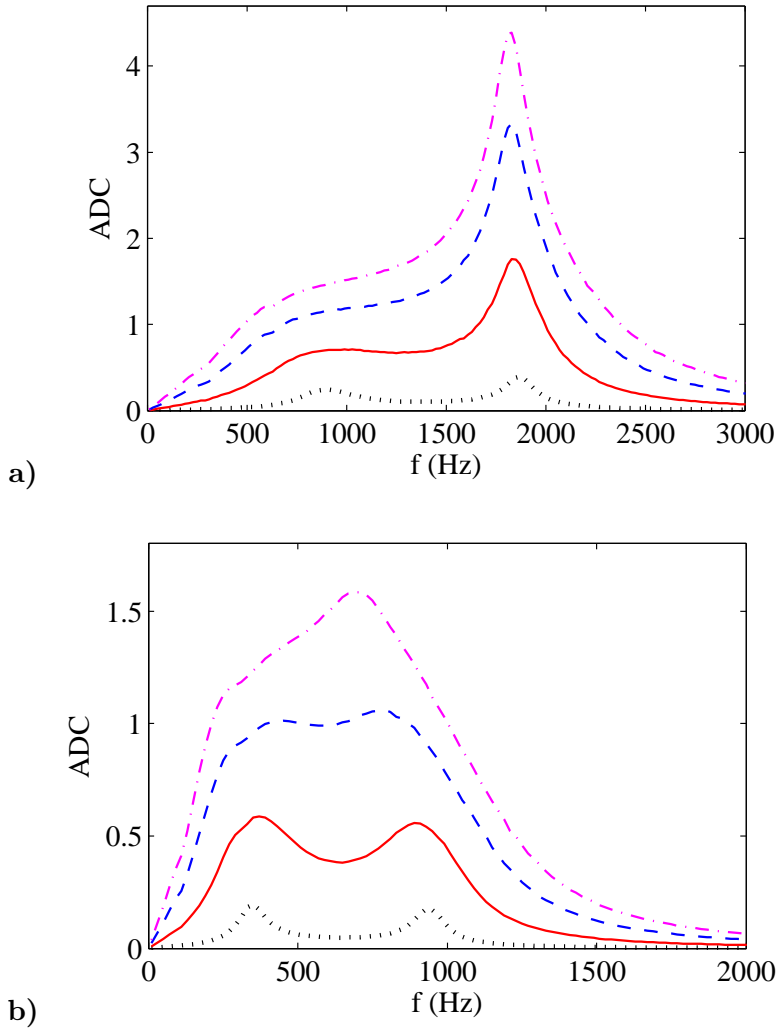


Figure 3.6: Frequency response of acoustic damping coefficient (ADC) for the Brass actuator a) and the Aluminum device b); black dotted line is for $K = 0.14$, red solid line $K = 1.14$, blue dashed line $K = 3.14$, magenta dash-dotted line $K = 5.14$.

are practically independent of the head loss coefficient, there is no resonance at the Helmholtz frequency (about 1000 Hz) and the incompressible model applies well up to frequencies not too greater than the Helmholtz frequency. Figure 3.5 a) shows that the acoustic oscillator is always forced by the diaphragm one, and exhibits two resonance peaks, at Helmholtz and structural frequencies. However, the amplification factor of the jet velocity oscillations, evaluated with reference to the incompressible solution of Equation (2.47), is remarkably greater than unity only for head loss coefficients equal to 1.14 and 0.14, which correspond to acoustic damping coefficients, Figure 3.6 c), well below 1 at the Helmholtz frequency.

The previous Figures 3.4-3.6 b), show that for the Aluminum device the oscillators are fully coupled, as one expects from the relatively high coupling factor $CF = 1.38$. In fact, the diaphragm velocity, Figure 3.4 b), exhibits two resonance peaks (remember that for this device the structural resonance frequency is less than the Helmholtz one). Both velocity resonance peaks are influenced by the non-linear damping coefficient and for values of $K = 3.14$ and $K = 5.14$ (with the corresponding values of the damping coefficient being equal to about 1 and greater than 1, respectively) the jet velocity does not present resonance peaks. Moreover, note that for $K = 3.14$ and $K = 5.14$ the Helmholtz resonance frequency moves remarkably towards lower values compared with the value of the almost undamped situation ($K = 0.14$).

3.1.2 Effect of the voltage

Based on the scaling relationships of the jet velocity shown in Section 2.2.2, for instance with reference to Equation (2.29), remembering that U_{inc} scales with Δx_w (which in turn is proportional to V_{ac} through Equation (2.4)), it is possible to argue that the jet velocity basically depends linearly on the supply voltage, apart from a weak nonlinear influence due to the fluidic damping term. Moreover, due again to the damping effects, as the voltage increases a corresponding reduction of the distance between the (coupled) resonance frequencies is observed in LEM simulations (not shown herein). This agrees with the experimental measurements reported by Crowther and Gomes [66], who studied the frequency response of SJ actuators by varying

the supply voltage. However, it has to be pointed out that for relatively high voltage values the benefit of higher velocities is remarkably reduced. It is believed that this behavior is due to the gradual saturation of the PZT material (as addressed also by Krishnan and Mohseni [58]). Hence, in practice the velocity amplitude does not exhibit a linear behavior with increasing the excitation amplitude, as depicted in Figure 3.7 reprinted from Crowther and Gomes [66]. On the other hand, these authors asserted also that measurements of the diaphragm peak displacement at a high excitation voltage ($V_{ac} = 250$ V) show that this is of the order of $75 \mu\text{m}$, which is well within the expected linear stiffness region of the diaphragm, so this is unlikely to contribute towards saturation. Therefore, they concluded that "there would be non-linear fluid dynamic losses due to compressibility and viscous effects as the flow discharges through the orifice".

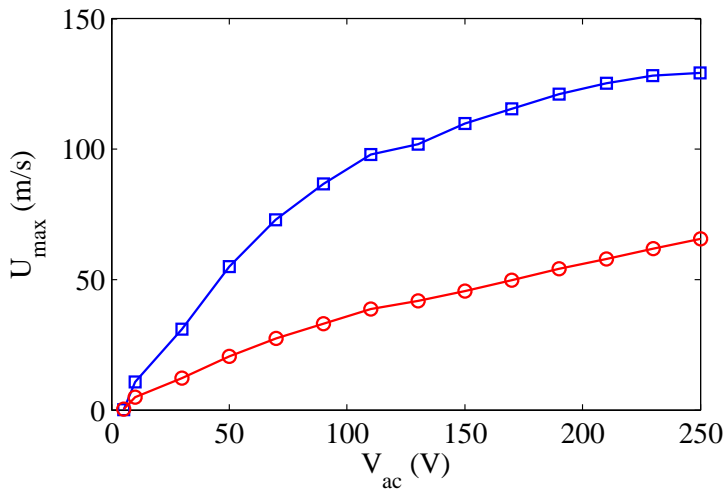


Figure 3.7: SJ peak velocity response as a function of excitation frequency at resonant frequencies ($h/d_o = 2.1$ and $H/d_o = 0.56$). Blue data points are for diaphragm resonance, red data for acoustic resonance. Reprinted from [66].

Crowther and Gomes [66] faced also the influence of the electric voltage on the energy efficiency, i.e. the ratio of the air kinetic energy issuing from the orifice to the input electric power, of SJ devices (which will be the

topic of the next Section). They found experimentally that as the peak-to-peak excitation amplitude increases above $120V$, the energy efficiency η remarkably reduces, decreasing to a value of 7 per cent at the peak velocity output condition, i.e. $V_{ac} = 250V$, as shown in Figure 3.8.

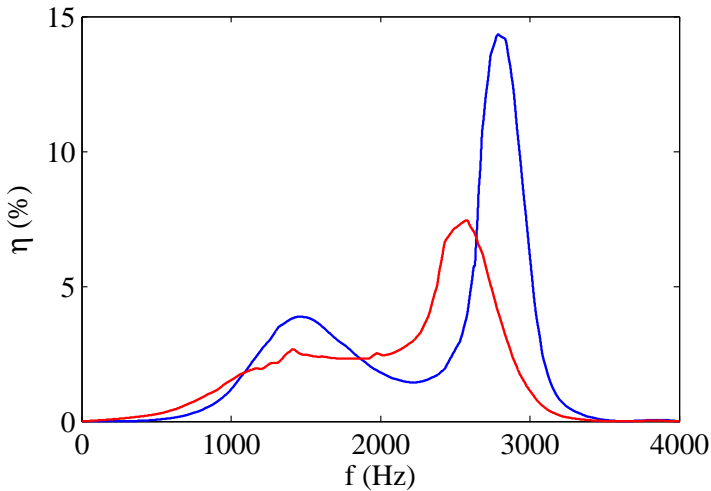


Figure 3.8: Electric–fluid energy conversion efficiency as a function of excitation frequency. Blue line is for $V_{ac} = 90V$, red line for $V_{ac} = 250V$ ($h/d_0 = 2.1$ and $H/d_0 = 0.56$). Reprinted from [66].

Gil and Strzelczyk [64] too described the effects of the supply voltage on the efficiency of the actuators, but their analysis refers to the case of loudspeaker-driven actuators and is restricted to very low values of voltage.

3.1.3 Effect of the orifice length

The effective orifice length, l_e , has a relatively strong effect, because it influences the magnitude of the jet velocity issuing from the orifice through the amount of the fluidic damping coefficient, and the nominal Helmholtz’s frequency, which is inversely proportional to the effective mass of the air at the orifice, $m_a = \rho_a l_e A_o$. The diaphragm structural frequency should be in principle independent of this parameter and therefore it should keep constant, apart from the influence of the coupled damping effects.

Gomes et al. [59] carried out an extensive experimental investigation

about the influence of the orifice nominal depth l_o . They claimed preliminarily that there are two effects acting on the flow traveling through the orifice which are of importance to understand how the velocity behaves with increasing the orifice length: firstly, the shorter the extension of the orifice, the bigger the effect of vena contracta on the volume flow rate will be. Secondly, the boundary layer displacement thickness grows with length, due to the shear action of the slow fluid near the wall on the faster flow in the core. This tends to slow down the core flow and hence to reduce the peak velocity. Therefore, there must be a compromise between these two phenomena such that an optimum can be reached. Gomes et al. [59] argued that the optimal length of orifice would be the summation of the length required to achieve marginally attached flow so as to minimize the vena contracta effect (i.e. $l_o/d_o \simeq 0.75$), plus the minimum length required for the flow to exit uniformly without curvature (about half exit diameter), resulting in a total orifice depth of around $l_o/d_o \simeq 1.25$. The major findings of their experimental measurements are summarized as follows: the actuator peak velocity reduces with increasing the orifice depth; the unsteadiness of magnitude and position of the diaphragm resonance peak gradually reduces with increasing the orifice depth. The entire decoupling of cavity resonance from diaphragm resonance is gradually offset to lower frequencies with increasing l_o/d_o . This effect supports the theoretical prediction of the inverse square proportionality between the Helmholtz frequency value and the orifice depth.

Figures 3.9 and 3.10 report the frequency response of the exit flow velocity for two of the actuators tested by de Luca et al. [60] and frequently reconsidered in this paper, for various values of nondimensional effective length l_e/d_o . It is worth to remind the reader that the effective length of the orifice corresponds to the distance between the locations of application of the Bernoulli equation and influences the volume of air mass of the Helmholtz oscillator. In both cases here examined, the structural frequency remains almost unchanged, while the Helmholtz's one attains lower values for higher effective orifice lengths; one should also remember that for the Brass actuator the Helmholtz's frequency corresponds to the first resonance peak, whilst for the aluminum device the situation is reversed. Furthermore,

it is interesting also to observe that the corresponding jet velocity slightly diminishes at the Helmholtz frequencies for the Brass actuator (in agreement with the findings of Gomes et al. [59]), but it increases for the case of aluminum. The peak velocity at structural resonance frequency decreases with increasing l_e/d_o for Aluminum actuator.

Gil and Strzelczyk [64] reported other experimental data on the effect of the orifice length, but their measurements refer to the case of loudspeaker-driven actuator.

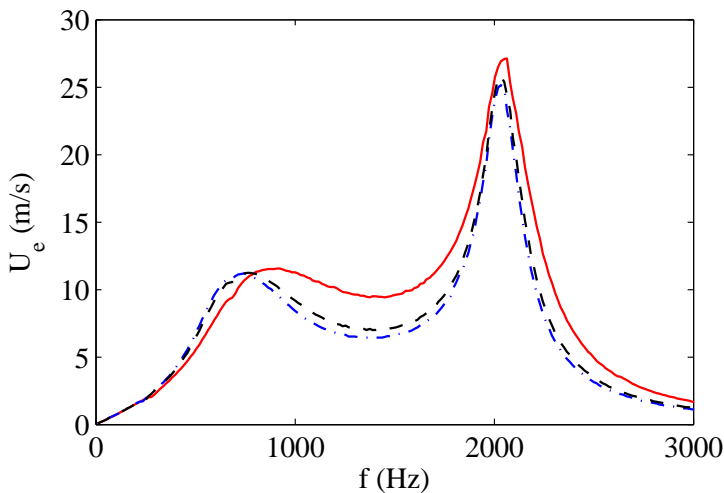


Figure 3.9: Frequency response of saddle point velocity for the Brass actuator at different equivalent length; red solid line refers to $l_e/d = 1$, blue dashed line to $l_e/d = 2$ and black dotted line to $l_e/d = 3$.

3.2 Efficiency of piezo-driven devices

Crowther and Gomes [66] studied the system costs associated with the application of flow control system to civil transport aircraft based, on the use of electrically powered synthetic jet actuators. They defined the efficiency of the actuator as fluid power (scaling with the cube of the exit velocity) divided by absorbed electrical power, and analyzed it as a function of the operating conditions and actuator geometry, which were chosen reasonably

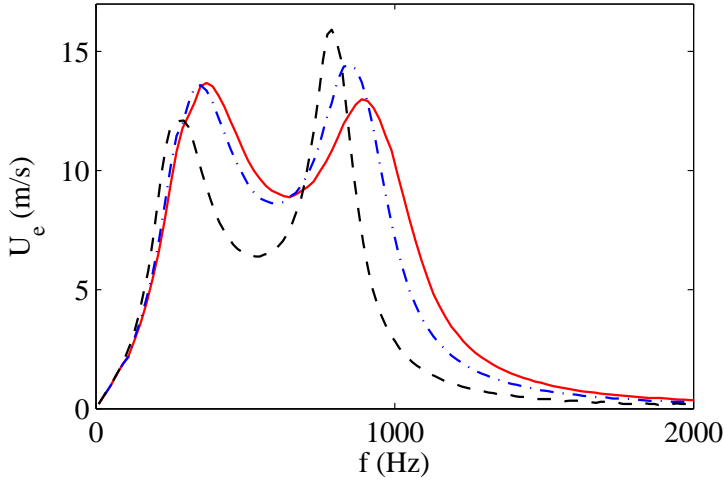


Figure 3.10: Frequency response of saddle point flow velocity for the Aluminum actuator at different equivalent length; red solid line refers to $l_e/d = 1$, blue dashed line to $l_e/d = 2$ and black dotted line to $l_e/d = 3$.

close to those expected for industrial applications. For this reason the experiments were carried out basically with a chamber depth to orifice diameter ratio equal to 0.56 and an orifice depth to diameter ratio equal to 2.1. By resorting to the energy balance principle, Crowther and Gomes [66] considered that the difference between the supplied electrical power and the gained fluid power was lost because of electrical impedance (ascribed to the piezo-electric actuator), mechanical impedance (related to the diaphragm dynamics) and acoustic impedance (due to the fluid-acoustic coupling of the flow within the cavity and through the orifice), however without accurately quantifying each term of the balance. They showed their experimental findings in terms of a map of the electric-fluidic conversion efficiency, where such an efficiency was reported as a function of excitation voltage amplitude (for peak-to-peak excitation voltage up to 250 V) and actuation frequency (up to 4000 Hz). They found that the efficiency attains a maximum equal to about 14% and noted that it did not correspond to the condition of maximum exit velocity because of the dielectric saturation effect (discussed in the previous paragraph) affecting the commercial piezo-electric patch (i.e.,

the piezo-element bonded to the Brass shim).

A more recent work, focusing specifically on the energy conversion efficiency of synthetic jets devices, was presented by Li et al. [67] who tried to express on an analytical basis every term contributing to the energy rate balance. They argued that once the synthetic jet has received electric energy input, due to the capacitance of the piezo-electric actuator, a part of the energy is stored as electric potential energy while the rest of the energy is converted to mechanical energy accompanied by energy dissipation. The mechanical energy includes vibration of piezo-electric actuators and kinetic energy of air flow. For piezo-electric actuators two forms of energy, i.e. strain energy and kinetic energy, are temporarily stored by the vibrating structure. Energy dissipation (namely energy loss) occurs in piezo-electric actuators due to the deflection dynamics, as well as in the air flow motion (i.e., the head losses) when traversing the jet orifice. The synthetic jet device efficiency is defined as the ratio of the kinetic power of the air flow to the input electric energy. The authors carried out experiments on two slot synthetic jets having orifice length of 4 mm and 15 mm, for two values of voltage amplitude (80 V and 100 V) and actuation frequency ranging from 200 Hz to 1100 Hz. Li et al. [67] found that the efficiency of energy conversion is dependent on the orifice size and on the operating conditions (namely, voltage and frequency) showing a peak (of about 40% for the 15 mm orifice) close to the mechanical resonance frequency of the actuator.

In the attempt of assessing a rigorous and comprehensive physical approach to the evaluation of the efficiency of piezo-electrically driven synthetic jet actuators, based on a rather detailed modeling of the actuator dynamics, it is presented a novel approach where the energy balance equation, properly averaged over the actuation period, is derived directly from the equations governing the dynamics of the actuator. The (instantaneous) energy balance equation of the actuator system can be obtained by summing the Equations of energy of the diaphragm (that takes into account both kinetic and elastic strain contributions) and of kinetic energy of the air mass through the orifice. Moreover, to characterize the actuator behavior over an operating cycle, it is convenient to apply the time average operator on

the resulting equation, defined as:

$$\bar{\varphi} = \frac{1}{T} \int_0^T \varphi dt \quad (3.1)$$

where φ is the generic time-dependent variable.

The energy balance equation averaged over an actuation cycle (i.e., over a time equal to the period T) is given by

$$\begin{aligned} \underbrace{\frac{1}{T} \int_0^T d(E_w + E_o)}_{\overline{\Delta E}} &= \underbrace{\frac{1}{T} \int_0^T F \dot{x}_w dt}_{\bar{P}_e} + \underbrace{\frac{1}{T} \int_0^T p_i (A_o U - A_w \dot{x}_w) dt}_{\bar{P}_m} \\ &- \underbrace{\frac{1}{T} \int_0^T c_{wt} \dot{x}_w^2 dt}_{\bar{D}_s} - \underbrace{\frac{1}{T} \int_0^T \frac{1}{2} (K-1) \rho_a A_o |U|^3 dt}_{\bar{D}_f} - \underbrace{\frac{1}{T} \int_0^T \frac{1}{2} \rho_a A_o |U|^3 dt}_{\bar{P}_k} \end{aligned} \quad (3.2)$$

An accurate description of the various contributions of Equation (3.2) is reported hereafter:

- $\overline{\Delta E}$ is the total energy variation. Note that this term is null because, for each cycle, there is no change for E_w and E_o , with E_w and E_o being the diaphragm energy and the kinetic energy of air issuing from the orifice, respectively. The diaphragm energy takes into account both kinetic and elastic strain contributions.
- \bar{P}_e is the electrodynamic power provided to the membrane by the applied voltage.
- \bar{P}_m is the mechanical power due to the work done by the differential pressure p_i which acts on the wall surface A_w and on the orifice surface A_o . By using the equation (2.10), it can be shown that this term is proportional to $\frac{1}{2}(p_i^2(T) - p_i^2(0))$ and, therefore, it does not give any contribution because p_i assumes the same value at the beginning and end of each cycle. One can reach the same result by observing that the pressure work is conservative by definition.
- \bar{D}_s is the power dissipation due to the structural damping effects of

the diaphragm. Note that, according to standard notations, $c_{wt} = 2m_{wt}\zeta_w\omega_w$.

- \bar{D}_f is the power dissipation due to the head loss of fluid dynamics type at the orifice.
- \bar{P}_k is the kinetic power of air flow at the orifice. Note explicitly that the kinetic power here refers by definition to the entire cycle, i.e. the suction phase included.

Then, by deleting $\overline{\Delta E}$ and \bar{P}_m terms, the Equation (3.2) becomes:

$$\bar{P}_e - \bar{D}_s - \bar{D}_f - \bar{P}_k = 0 \quad (3.3)$$

and, once defined the kinetic efficiency η_k as the ratio of the kinetic power of the exit flow \bar{P}_k to the electrodynamic power \bar{P}_e , one obtains:

$$\eta_k = \frac{\bar{P}_k}{\bar{P}_e} = 1 - \frac{\bar{D}_s + \bar{D}_f}{\bar{P}_e} \quad (3.4)$$

In practice, the global efficiency of an actuator has to quantify the amount of Joule power provided to the system \bar{P}_j that is actually converted in \bar{P}_e . This can be done by introducing the electrodynamic transduction efficiency η_e :

$$\eta_e = \frac{\bar{P}_e}{\bar{P}_j} \quad (3.5)$$

Hence, finally, one can define the (global) efficiency of the actuator η as the product of η_k by η_e

$$\eta = \eta_k \eta_e = \frac{\bar{P}_k}{\bar{P}_j} \quad (3.6)$$

where the external Joule power supply \bar{P}_j provided to the actuator is calculated as

$$\bar{P}_j = \frac{1}{T} \int_0^T VI dt \quad (3.7)$$

with $V = V_{ac} \sin \omega t$ being the applied voltage and I the electric current flowing through the piezo-electric element.

The rate of \bar{P}_j not turned into \bar{P}_e is converted into a variation of internal energy \dot{Q} of the air inside the cavity (heat generation per unit time), which

is transferred in part to the external ambient through a natural convection mechanism, and, in part, into enthalpy flow rate of the air leaving the orifice:

$$\bar{P}_j - \bar{P}_e = \dot{Q} \equiv hA_e\Delta T + \dot{m}_a c_p \Delta T \quad (3.8)$$

where h is the convective heat transfer coefficient by natural convection, A_e is the exchange surface (which depends on the relevant geometry of actuator), ΔT is the average-per-cycle temperature difference between the system and the colder surrounding external air, $\dot{m}_a = \rho_a \bar{U} A_o$ and remembering that \bar{U} is the average velocity associated to the stroke length (Equation 2.20), and c_p is the specific heat coefficient at constant pressure.

For the sake of simplicity it is assumed that the air inside the cavity is isothermal with the device case.

From Equation (3.8) one obtains also:

$$\eta_e = 1 - \frac{\dot{Q}}{\bar{P}_j} \quad (3.9)$$

Moreover, it is important to note that the energy conversion process from electrodynamic energy to flow kinetic energy depends intrinsically on the coupling degree between the two oscillators modeling the device behavior, i.e. the membrane and the Helmholtz one. From the dynamical point of view the coupling effect is represented by the internal pressure term acting as a forcing term on the Helmholtz oscillator; from the energy point of view, the coupling effect can be seen as a transfer of mechanical power (e.g, the work done by the internal pressure) to the Helmholtz oscillator, expressed by:

$$\bar{P}_{mH} = \frac{1}{T} \int_0^T p_i A_w \dot{x}_w dt \quad (3.10)$$

It is clearly evident that, although the net mechanical power due to the pressure work introduced in Equation (3.2) is null, \bar{P}_{mH} defined in the above equation is not, and it is convenient to split ideally the conversion process from electrodynamic energy to flow kinetic energy into two steps: the conversion of electrodynamic energy \bar{P}_e to mechanical power due to the pressure work (within the membrane oscillator), namely \bar{P}_{mH} , and the conversion of mechanical power to air flow kinetic energy (within the Helmholtz

oscillator). In equation terms, once introduced the *internal* efficiencies:

$$\eta^* = \frac{\bar{P}_{mH}}{\bar{P}_e} \quad (3.11)$$

$$\eta^{**} = \frac{\bar{P}_k}{\bar{P}_{mH}} \quad (3.12)$$

the kinetic efficiency of Equation (3.4) can be interpreted as:

$$\eta_k = \eta^* \eta^{**} \quad (3.13)$$

In discussing the results, it will see that, while η^{**} is generally very high, as perhaps expected η^* depends crucially on the coupling degree between the two oscillators. In the case of reduced coupling, η^* can be very low and it reduces dramatically also the kinetic efficiency of the device. Furthermore, note that a limited coupling degree does not imply a low air flow velocity; it means that a certain value of air jet velocity is obtained at the price of a very low energy efficiency.

The influence of the coupling degree of the oscillators on the kinetic energy efficiency will be hereafter discussed, by monitoring the internal efficiencies η^* and η^{**} defined by Equations (3.11) and (3.12). This will be made with the aid of Tables 3.1 and 3.2, where the relevant efficiencies are reported as functions of the applied voltage, for the brass and Aluminum actuators respectively. Note that for the first device the data refer to the modified resonance structural frequency (about 2200 Hz), whereas for the latter device the data refer to the modified resonance Helmholtz frequency (about 900 Hz).

As anticipated before, it is evident that, while η^{**} is generally very high for both the devices, η^* depends crucially on the coupling degree between the two oscillators. In the case of brass shim device having $CF=0.06$ the amount of mechanical power transferred from the diaphragm oscillator to the Helmholtz one is remarkably reduced, hence η^* is very low. Of course this reduces dramatically also the kinetic efficiency of the device and finally the global efficiency. For the other one the coupling parameter is $CF=1.88$ and the actuator exhibits significantly higher values of η^* .

$V_a(V)$	$\eta_k(\%)$	$\eta^{**}(\%)$	$\eta^*(\%)$
25	4.7	85.5	5.5
30	5.3	85.3	6.3
35	5.9	85	6.9
40	6.4	84.8	7.5
45	6.8	85.5	7.9
50	7.3	88.6	8.2
55	7.5	86.6	8.7
60	7.6	85.6	8.9
65	7.9	87.1	9.1
70	8.1	87.8	9.2
75	8.5	83.7	10.1

Table 3.1: Efficiencies of Brass actuator at modified resonance structural frequency. $CF=0.06$

$V_a(V)$	$\eta_k(\%)$	$\eta^{**}(\%)$	$\eta^*(\%)$
25	79.2	86.6	91.6
30	79.5	87.6	90.7
35	79.7	88.2	90.4
40	80.7	86.4	93.4
45	80.3	87.7	91.6
50	80.2	87.9	91.3
55	82.3	82.3	88.9
60	81.8	87.5	93.4
65	81.8	87.8	92.1
70	80.1	87.3	91.8
75	81	87.9	92.2

Table 3.2: Efficiencies of Aluminum actuator at modified resonance Helmholtz frequency. $CF=1.88$.

Finally, it should be observed that a low value of kinetic efficiency does not corresponds necessarily to a low value of air jet velocity at exit orifice, but it means that a certain air jet is achieved by a low energy conversion efficiency.

It is also possible to note that, for two cavities configurations which share the same diaphragm (introduced by Luo et al. [52]), computations show that for high coupling degree (which is the case of Aluminum actuator discussed in the present paper) the global kinetic efficiency remains almost the same as compared to the base single cavity configuration, and therefore the kinetic efficiency of the single cavity is halved.

Chapter 4

Influence of a piezo-driven SJ on a water spray behavior

4.1 Introduction

Spray-based technologies are largely employed in a wide variety of sectors, such as internal combustion engines (Zao et al. [68]), turbines (Alhazmy and Najjar [69]), fire control systems (Grant et al. [70]), as well as agriculture (Sunder and Panda [71]) and several manufacturing processes (Hascalik et al. [72]). The technological improvement has been mainly focused on pressure control (Lee and Park [73]), size and nozzle-hole number (Kim et al. [74]), tip penetration length and cone angle (Aleiferis et al. [75]). At the same time, the opportunity of directly managing spray formation and its characteristics has gained much interest among active flow control methods using different types of actuators, Cattafesta and Sheplak [5].

A first classification of spray control mechanisms was made by Photos and Longmire [76] depending on the way of interacting with a spray: direct, if a direct impact between the control mechanism and droplets occurs; indirect, if the interaction is produced by controlling the space and the size of fluid structures. Among them, synthetic jet actuators seem to be a promising technology for spray direct control, showing the potential to affect their global behavior as well as their characteristics at local level, Pavlova et al. [32].

Synthetic jet actuation has been used in jet vectoring. Smith and Glezer [25] studied the interaction between a rectangular air jet and a co-flowing synthetic jet. Tamburello and Amitay [29] used synthetic jets to control a particle-laden jet. They claimed that the jet effect on the particle motion was both direct (increasing momentum from the jet) and indirect (due to the spreading of the particles, caused by the vortical structures of the synthetic jet).

The interaction between spray droplets and large-scale eddies was first investigated experimentally by Bachalo et al. [77], obtaining accurate measurements of velocity and droplets size. Wang et al. [78] used a piezo-electric modulator, mounted within the nozzle, to introduce perturbations to the fluid inside the spray nozzle. They aimed to improve the break-up process and modify the characteristics of the spray. Pavlova et al. [32, 30] examined the effect of piezo-driven synthetic jet actuators on a water spray behavior. They obtained information about the main characteristics of the spray, such as the vectoring angle and the cone angle, for several values of the flow rate ratio and the synthetic jet momentum coefficient, and the enhancement of its cooling performances.

The SJ actuators have been extensively investigated in previous chapters 2 and 3. The effect of these devices on an air atomized spray was investigated by Pavlova et al. [32], quantified through a non-dimensional parameter: the momentum coefficient, defined as:

$$C_\mu = \frac{A_o \bar{U}^2}{A_s \bar{U}_{so}^2} \quad (4.1)$$

where A_o and A_s are the orifice area of the synthetic jet and the spray, respectively; whereas \bar{U}_{so} is the average air exit velocity at the spray orifice, and \bar{U} is the synthetic jet average orifice velocity, already defined in Equation (2.20).

This Chapter aims at presenting a very interesting application of SJ devices: an investigation on the effect of a SJ actuator on a continuous water spray behavior. The experimental apparatus, the methodologies applied and the characteristics of the actuator will be presented in paragraph 4.2. The paragraph 4.3 will be dedicated to the definition of a new momentum

coefficient, which takes into account the densities of the operating fluids, and results will be presented in terms of spray velocity and vorticity distribution fields.

4.2 Experimental Apparatus and Procedure

4.2.1 Experimental mock-up

The spray behavior has been characterized through an optical diagnostic technique. Considering the low droplets velocity, a statistical analysis has been applied to establish the spray regions effectively influenced by the SJ device. Particle Image Velocimetry (PIV) technique has allowed to measure spray velocity. Figure 4.1 shows the PIV experimental apparatus and the water injection system. The latter is composed of a high pressure pump used to supply water to a one-hole misting nozzle ($300\ \mu\text{m}$ in diameter), which injects the working fluid in a $4500\ \text{cm}^3$ quiescent optically accessible tank at ambient temperature and pressure. The injector works in continuous mode and its working regime is managed by a rubber ball connected to a spring; when the liquid pressure exceeds the elastic spring force, the ball moves allowing the liquid passage. For this reason the spray can be considered as continuous and stationary.

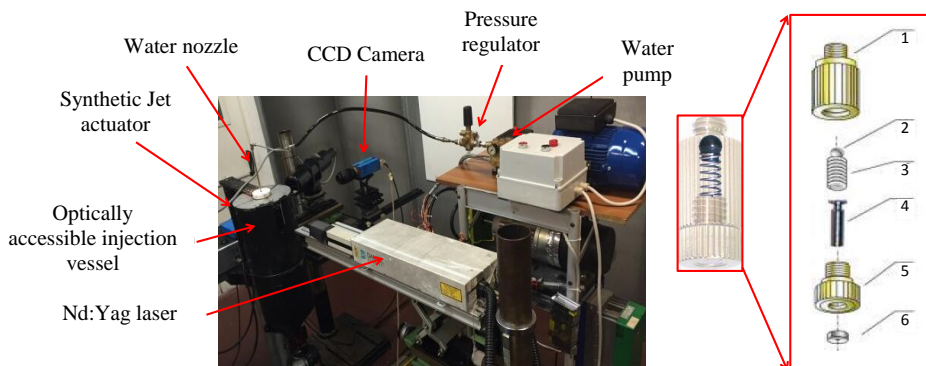


Figure 4.1: PIV and injection system experimental apparatus (left) - Hole misting nozzle sketch (right).

A twin head pulsed Nd:YAG laser (532 nm wavelength), has been synchronized with a CCD camera in order to perform PIV measurements. An appropriate optical path converts the laser beam in a sheet (0.2 mm of thickness and 60 mm of height) crossing the spray axis, coincident with the vessel one. The light scattered by the spray has been collected by the CCD camera, mounted perpendicularly to it. Images (2048 x 2048 pixel of resolution and $7.4 \times 7.4 \mu\text{m}$ of pixel size) have been acquired in double frame mode in order to record a pair of them for each trigger signal, with a frequency of 1 Hz, for a total of 300 couples of images. An adaptive correlation process has been applied to track the droplets clusters and to estimate their speed. This method uses an initial interrogation area (IA) having a size N times the final IA. Each intermediary result is used as information for the next IA of smaller size, until the smallest IA size is reached. A 32×32 pixels final IA has been reached starting by a size of 128×128 pixels. A local validation procedure has been applied in order to minimize false sample vectors and a 50% overlap of interrogation areas has been set to recover the loss of vector field resolution. Furthermore, the analysis has been completed by the Peak Height Validation criterion and the Local Neighborhood Validation method.

The previous analysis has been conducted without seeding, using the water droplets as tracer. The particles dimension depends on the injection pressure and has been computed using the Phase Doppler Anemometry (PDA) technique (not shown here). A higher injection pressure results in an enhanced atomization, producing particles with a smaller size: about $40 \mu\text{m}$ for the 5 MPa pressure case and $35 \mu\text{m}$ for 10 MPa in the impact region. Moreover, the particles size tends to increase going from the center to the edge of the spray, moving further away from the nozzle. In this case, the droplets dimension in the impact region is uniform enough to not compromise PIV measurements. Note that the seeding density and the camera resolution did not allow the use of Particle Tracking Velocimetry (PTV).

All the experiments have been conducted in the atmospheric chamber test rig with a drain at the bottom driven by a vacuum pump to remove the moisture. Further details about PIV equipment can be found in the work of Marchitto et al. [33]. Tests have been carried out under quiescent conditions

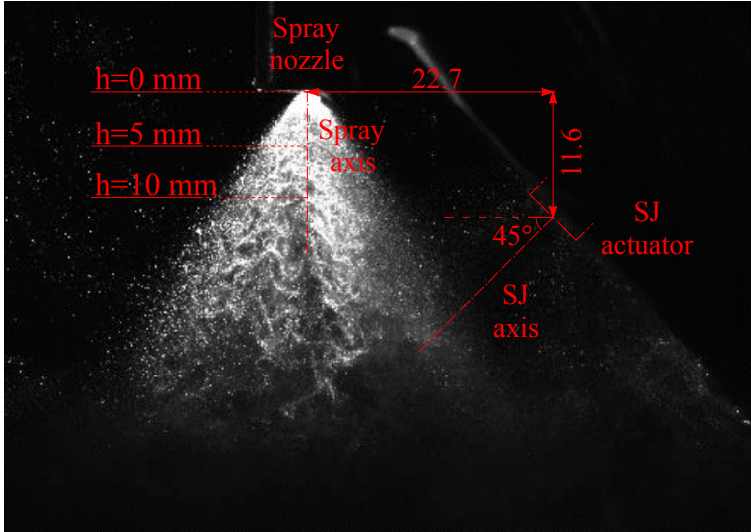


Figure 4.2: Relative positions between the nozzle and the synthetic jet actuator.

at two injection pressures, namely 5 MPa and 10 MPa, exploring the effect produced by the synthetic jet perturbations on the droplets velocity and size. The inclination of the synthetic jet axis has been set equal to 45° with respect to the nozzle axis direction, as shown in Figure 4.2, in a such a way the synthetic jet impacts perpendicularly to the water spray. The relative vertical distance of the SJ orifice with respect to the water nozzle has been varied from a maximum of 11.6 mm, corresponding to a conventional position of spray nozzle $h = 0$ mm, down to 1.6 mm ($h = 10$ mm) with a step of 5 mm. PIV Measurements have been carried out for all the combinations of selected injection pressures and spray nozzle/ SJ orifice relative positions, summarized in Table 4.1, each of them being repeated for ON and OFF control, for a total of 12 tests.

4.2.2 Synthetic jet actuator

The SJ actuator used in this application is similar to those already studied in previous chapters and its main characteristics are reported in Table 4.2. It is a modular structure device, Figure 4.3, with a brass membrane, allowing independent variations of cavity diameter, height and orifice diameter.

	Injection Pressure, P_i	Nozzle Height, h
Case 1	5 MPa	0 mm
Case 2	10 MPa	0 mm
Case 3	5 MPa	5 mm
Case 4	10 MPa	5 mm
Case 5	5 MPa	10 mm
Case 6	10 MPa	10 mm

Table 4.1: PIV operating conditions.

During its experimental characterization, the actuator has been electrically excited with a sine signal generated through a USB Instruments DS1M12 or “Stingray” (which can work simultaneously as both signal generator and data-acquisition system) and then transmitted to a linear gain amplifier (Piezo Linear Amplifier EPA-104). Jet exit velocities have been measured in the external ambient at the saddle point, located on the jet axis at one diameter away from the orifice exit section. The velocity measurements have been carried out with a standard Kanomax mini Pitot tube, 1/8 in in diameter and 6 in in length, connected with a Mouser sensor pressure transducer. The output signal has been phase-averaged over typically 20 periods to obtain an uncertainty estimate of the jet velocity within 5%, computed with the standard procedures suggested in specialized literature.

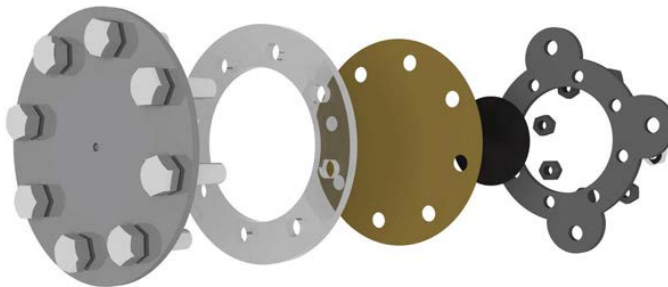


Figure 4.3: Exploded 3D view of the Brass synthetic jet actuator.

The device frequency response, in terms of saddle point velocity (U_e), is

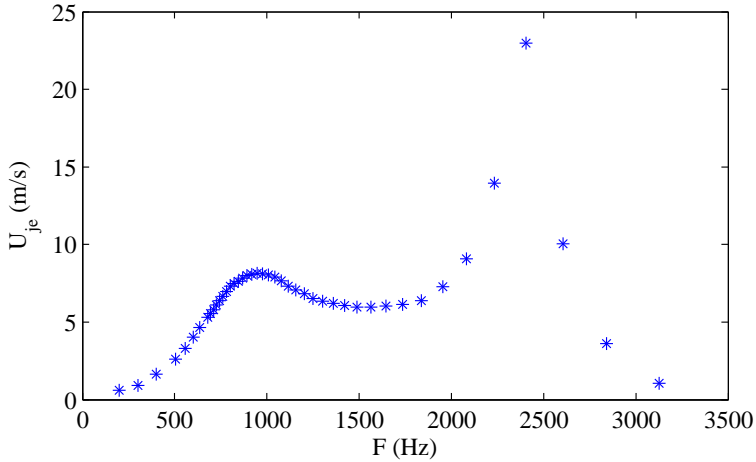


Figure 4.4: Frequency response of the Brass SJ actuator.

reported in Figure 4.4. It is worth to remind that this latter is different from the synthetic jet average orifice velocity (\bar{U}). As pointed out in paragraph 2.2.1, the saddle point velocity is roughly $\approx 1.1 U_{max}/\pi$, Equation (2.21). It is possible to note how the actuator exhibits two resonance frequencies, one near the uncoupled Helmholtz frequency and one in proximity of the diaphragm structural resonance frequency, with a maximum of about 22 m/s at $f = 2404$ Hz. With the aim to maximize the exit jet velocity and so the momentum coefficient, which is the main parameter for spray interaction, the actuation frequency has been chosen equal to the previous value.

Cavity diameter, d_w	35 mm
Cavity height, H	3 mm
Orifice length, l_o	2 mm
Orifice diameter, d_o	2 mm
Supply voltage, V_{ac}	70 V
Actuation frequency, f	2404 Hz

Table 4.2: Synthetic jet actuator characteristics.

4.2.3 Statistical analysis

Considering the low speed range of water sprays and the statistic nature of PIV measurements, a *T-test*, implemented in MATLAB, has been performed to discriminate between the stochastic spray variability and the perturbation produced by the synthetic jet, Sepe [79]. For each operative condition two vector maps, corresponding to active synthetic jet and free water spray cases, have been estimated as the average on 300 trials. A point-by-point comparison of the maps has been performed through the T-test code on the single interrogation areas.

The T-test is based on the assumptions that each sample population X_i follows a normal distribution with mean value μ and variance σ^2 and the two sample populations should have the same variance. First, a Normal Probability Plot has been built in order to estimate if each set of experimental data follows a normal distribution. The experimental data were sorted in ascending order and for each sorted value the Cumulative Distribution Function (CDF) was evaluated through the following estimator:

$$\hat{F}(x_i) = \frac{i}{n+1} \quad (4.2)$$

where x_i is the i -th sorted value of sample X and n is the sample dimension. The Cartesian product $(x_i, \hat{F}(x_i))$ has been compared to the linearized analytical CDF distribution. The method of ordinary least squares has been used to approximate the experimental distribution to the analytical one. All the distributions whose correlation coefficient between the experimental values and the least squares line is over than 0.90 have been considered normal. Once the normal distribution of samples has been confirmed, a *F-test* has been performed for verifying the assumption that the two sample populations have the same variance. The well-known Fisher-Snedecor distribution relation has been used as test statistic:

$$\frac{S_1^2 \sigma_2^2}{S_2^2 \sigma_1^2} = Z_{n-1, m-1} \quad (4.3)$$

where S_1^2 and S_2^2 represent the unbiased sample variance of the aleatory variables X_1 and X_2 respectively, n and m are the sample dimensions. The

unbiased sample variance can be written as:

$$S^2 = \frac{\sum_{i=1}^n (X_{1i} - \bar{X}_1)^2 + \sum_{i=1}^m (X_{2i} - \bar{X}_2)^2}{n + m - 2} \quad (4.4)$$

where X_{1i} and X_{2i} are respectively the i -th aleatory variables of the sampling of the sample populations X_1 and X_2 , which determinate the mean sample aleatory variables \bar{X}_1 and \bar{X}_2 . The null hypothesis of equality of variances is considered true if the actual value is below 0.05. Once all the assumptions are verified, the T-test can be performed through the T-distribution, used as test statistic:

$$\frac{(\bar{X}_1 - \bar{X}_2) - (\mu_1 - \mu_2)}{S \sqrt{\frac{1}{n} + \frac{1}{m}}} = T_{n+m-2} \quad (4.5)$$

The same threshold as for the F-test has been set for the null hypothesis of equality of means. Hence, if the null hypothesis is not satisfied the means difference can be attributed to the synthetic jet effect. Repeating this analysis for a large number of points in the spray domain, it has been possible to distinguish the regions in which the synthetic jet is effective from others where the effect is not relevant.

4.3 Results and Discussion

The synthetic jet actuator has been designed in order to work in direct mode. For this reason it is important that the air moved by the actuator is strong enough to modify the particles trajectory by means of a direct impact with them. The momentum coefficient defined in Equation (4.1), is the ratio of the synthetic jet momentum to the spray momentum due to the air part only.

In this work a generalization of this definition is introduced in order to take into account the differences in density between water, used for spray, and air, working fluid of the SJ device. The re-defined momentum coefficient C_μ^* results to be:

$$C_\mu^* = \frac{\dot{m}_j \bar{U}_j}{(\dot{m}_a + \dot{m}_l) \bar{U}_s} \quad (4.6)$$

where U_j and U_s are the SJ and spray velocities in the impact region, \dot{m}_j is the synthetic jet mass flow rate, \dot{m}_a is the mass flow rate of the air spray component and \dot{m}_l is the mass flow rate of the liquid spray component. Note that the SJ velocities (U_j) have been computed using the classical law $U_j \sim 1/x$, being x the longitudinal distance from the SJ orifice; while the spray velocities (U_s) have been extracted directly from the PIV measurements in the cases without actuation. It is interesting to observe that when the spray is almost completely composed by air, such as in an air atomized one, the expression can be simplified, recovering the Equation (4.1), with the velocities considered in the impact zone.

For the present activity, the estimated values for the momentum coefficient, C_μ^* , both for injection pressure of 5 MPa and 10 MPa, are reported in Table 4.3.

	5 MPa	10 MPa
C_μ^* at $h = 0$ mm	0.44	0.037
C_μ^* at $h = 5$ mm	0.18	0.013
C_μ^* at $h = 10$ mm	0.059	0.0068

Table 4.3: Estimated values for the momentum coefficient, C_μ^* .

As expected, the C_μ^* values for the 10 MPa cases are always lower than 5 MPa measurements, representing the diminished effectiveness of the SJ on the spray. For the Cases 2 (10 MPa and 0 mm) and 5 (5 MPa and 10 mm) the momentum coefficient takes similar values, thus producing comparable effects on the spray droplets.

4.3.1 Spray velocity field

PIV velocity measurements together with the corresponding influence regions will be reported and discussed hereafter. Applying the previous statistical analysis on the velocity fields allowed the determination of the actual influence of the SJ actuator on the spray. In the following figures, the blue region represents the device influence area on the velocity magnitude, while the red one is the zone in which the jet effect is negligible. Moreover, the effectiveness of the device could be appreciated by making a comparison

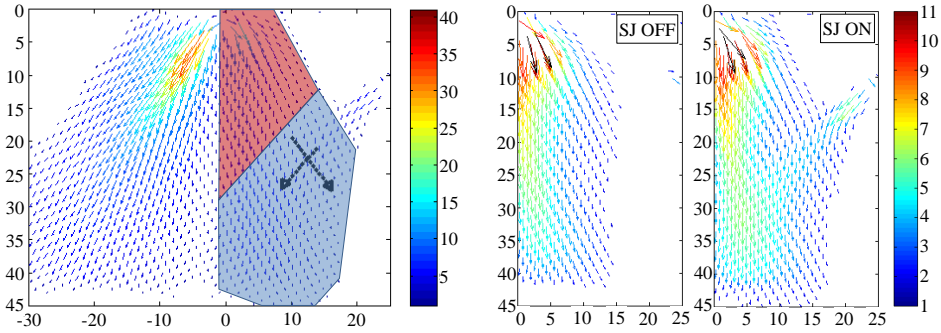


Figure 4.5: Case 1: Spray velocity field ($P_{inj} = 5$ MPa, $h = 0$ mm).

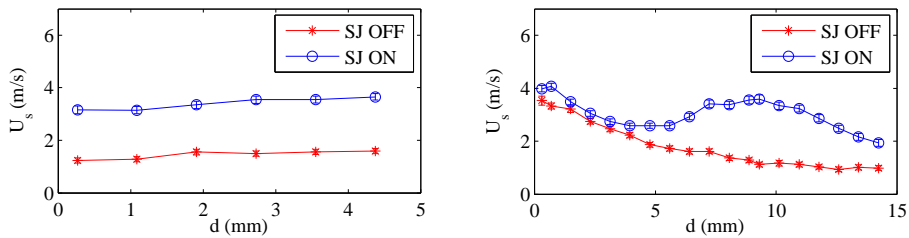


Figure 4.6: Velocity profiles (Case 1): longitudinal axis (left) and transverse axis (right).

between the zoomed right side of the domain, with and without actuation.

As regards the Case 1, in the left part of Figure 4.5 it is clearly visible how the SJ device modifies the spray velocity fields. Its main effect consists in the energization of all water droplets placed in the impact region between the spray and the synthetic jet. The right part, on the other hand, compares the velocity fields with and without actuation. The jet produced by the device is made visible due to the presence of water droplets in the injection chamber which, detached from the spray, have been dragged away by the air motion and can be considered as tracers.

The analysis is completed by representing the velocity profiles along two locally orthogonal axes (black arrows in the velocity field): the first one coincident with the synthetic jet longitudinal axis, the latter perpendicular to the former. For the longitudinal axis d represents the longitudinal distance measured starting from the spray edge, whereas for the transverse

axis d is measured along the spray edge, for a local line segment 15 mm long and symmetrical with respect to the SJ axis (where $d = 7.5\text{mm}$). For the Case 1, Figure 4.6 depicts how the SJ actuator improves constantly the droplets velocity of about 2 m/s along the SJ longitudinal axis, whereas the transverse velocity profiles show that the action of the synthetic jet is local, exhibiting a velocity increase only in the impact region (namely around $d = 7.5\text{ mm}$). In both directions the maximum increase in droplets velocity is about 100%.

The Case 2, representing the interaction for $P_{inj} = 10\text{ MPa}$ and $h = 0\text{ mm}$, is reported in Figures 4.7 and 4.8. It is interesting to notice a difference in the magnitude of the synthetic jet velocity between the 5 MPa and 10 MPa cases; this can be explained considering the higher atomization rate and the greater amount of water particles at 10 MPa near the synthetic jet orifice caused by the increased flow rate. This results in a higher amount of droplets in the region immediately around the synthetic jet orifice, where the air speed is generally higher, improving measurements accuracy. When injection pressure rises up (Figures 4.5 and 4.7), it is possible to note an overall increase in velocity magnitude for both cases, with and without actuation. More in detail, considering the velocity fields, the region of influence (blue one) becomes smaller, in accordance with the calculated C_{μ}^* coefficients (Table 4.3). As expected, at 10 MPa the droplets have higher momentum flux than for the case at 5 MPa and thus the modification of their motion is more difficult. At 10 MPa (Figure 4.8), indeed, the velocity enhancement lowers toward the water spray core, confirming the reduction of the SJ influence. Looking at the transverse axis, for both investigated pressures, a significant velocity gain has been found. This outcome is characterized by a local maximum located on the synthetic jet axis, while the velocity difference between the controlled and uncontrolled cases is almost negligible at a distance of about 5 mm from the center (borderline of the no-influence region).

The velocity vector fields at 5 and 10 MPa for $h = 5\text{ mm}$ are reported in Figures 4.9 and 4.11. As the injector is moved downward, the air flow impacts against the spray in a region closer to the nozzle. As expected, the higher water momentum flux induces a reduction of the air flow-water

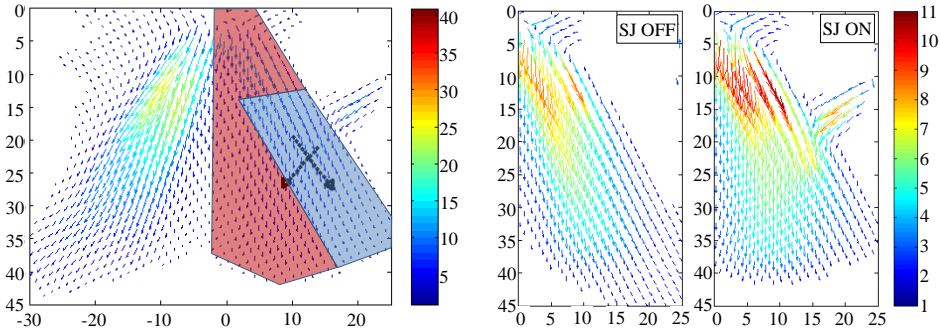


Figure 4.7: Case 2: Spray velocity field ($P_{inj} = 10$ MPa, $h = 0$ mm).

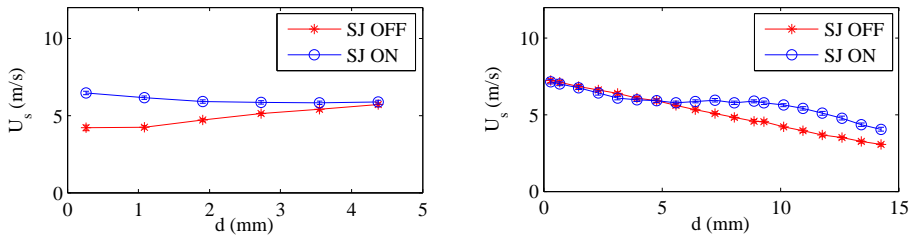


Figure 4.8: Velocity profiles (Case 2): longitudinal axis (left) and transverse axis (right).

spray interaction, both in terms of interaction region area and of velocity difference. Furthermore, note that at 5 MPa injection pressure the effect of the synthetic jet along its longitudinal axis resulted in a droplet velocity increase of about 1 m/s (Figure 4.10, left). At 10 MPa injection pressure, such an increase is almost negligible, with the velocity exhibiting only a slight difference (between on and off control cases) around the spray edge (from 1 mm to 2 mm), as shown in Figure 4.11, left. Looking at the cross axis profiles, as for the $h = 0$ mm case, a relatively small velocity increase is detected on the jet axis for injection pressure of 5 MPa (Figure 4.9, right), while the speed difference is almost negligible at 10 MPa (Figure 4.11, right). The difference in the water droplets velocity, between the 5 MPa and 10 MPa configurations, depends on the different way in which the jet approaches the spray. Due to the higher interaction at lower injection pressure, the synthetic jet seems to merge with the spray even upstream of the contact

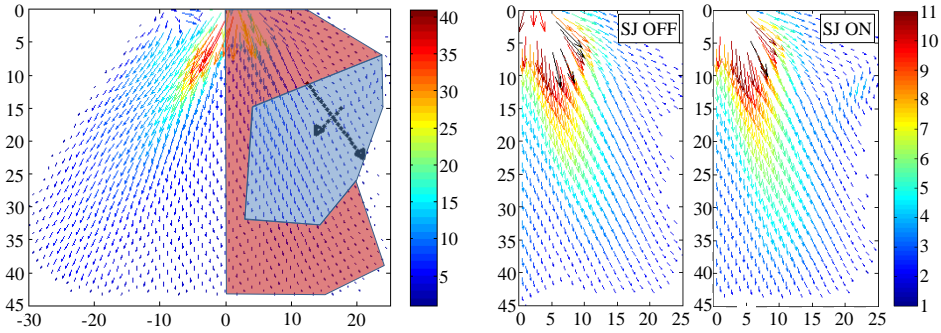


Figure 4.9: Case 3: Spray velocity field ($P_{inj} = 5$ MPa, $h = 5$ mm).

point and the result is a slight impact with a total energization; this allows a global velocity growth and an increase in spray diffusion. On the contrary, at higher injection pressure the impact is sharper because the jet is not able to influence the motion of the droplets, which follow their standard trajectory; therefore, the velocity increase is limited to the region near the impact point only.

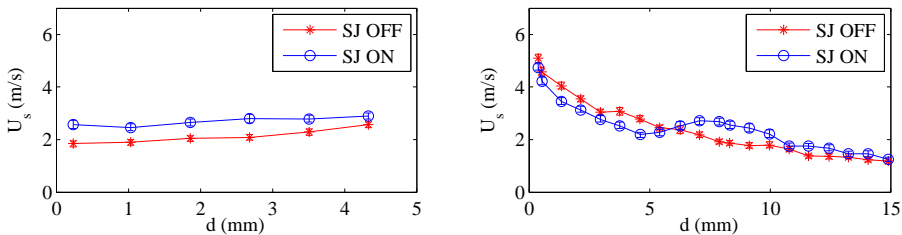


Figure 4.10: Velocity profiles (Case 3): longitudinal axis (left) and transverse axis (right).

The velocity vector fields at 5 MPa and 10 MPa for $h = 10$ mm are reported in Figures 4.13 and 4.15. Moving the injector to the lowest position results in a region of air-water impact immediately out of the nozzle hole. On the other hand the distance between synthetic jet orifice and spray is maximum, lowering the air speed in the region of impact. At 5 MPa the air flow-water spray interaction appears to be similar to the Case 3, both in terms of interaction region area and of velocity difference. Again, the effect

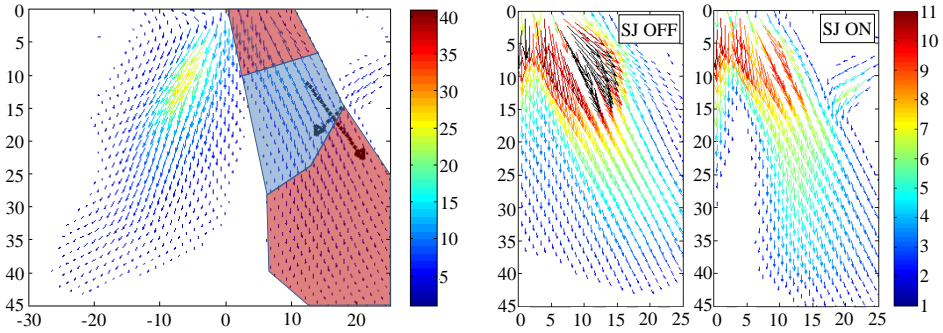


Figure 4.11: Case 4: Spray velocity field ($P_{inj} = 5 \text{ MPa}$, $h = 5 \text{ mm}$).

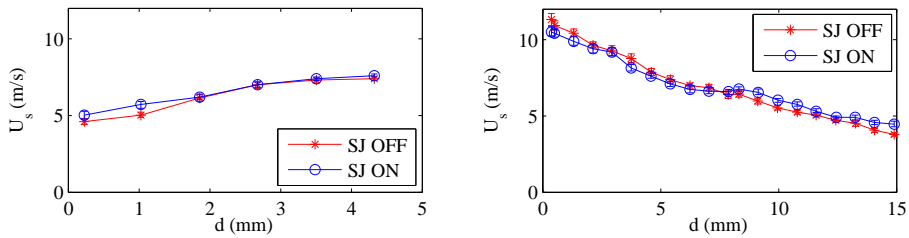


Figure 4.12: Velocity profiles (Case 4): longitudinal axis (left) and transverse axis (right).

of the synthetic jet along its longitudinal axis resulted in a droplet velocity increase of about 1 m/s (Figure 4.14, left). Increasing the injection pressure further increases the momentum flux and the effect of the synthetic jet is almost negligible, as shown in Figure 4.16. In this case, in fact, the region impact is immediately out of the nozzle hole, where the spray is compact and break up is still occurring. Moreover, the higher distance between the synthetic jet actuator and water spray produces a lower air velocity in the impact region and consequently decreases its influence.

4.3.2 Vorticity analysis

The effect of the SJ actuator on the water spray behavior has been further investigated by computing the out-of-plane component of the vorticity field (ω_z), Palumbo [80]. A vorticity analysis may be very useful to identify toroid coherent structures in the flow field, which are visualized as counter-rotating

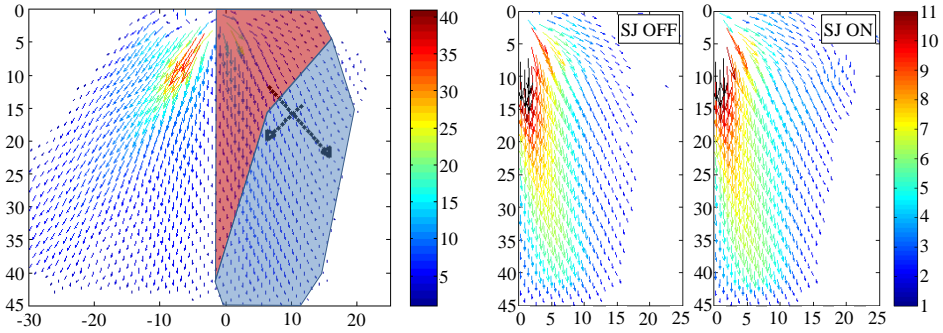


Figure 4.13: Case 5: Spray velocity field ($P_{inj} = 5$ MPa, $h = 10$ mm).

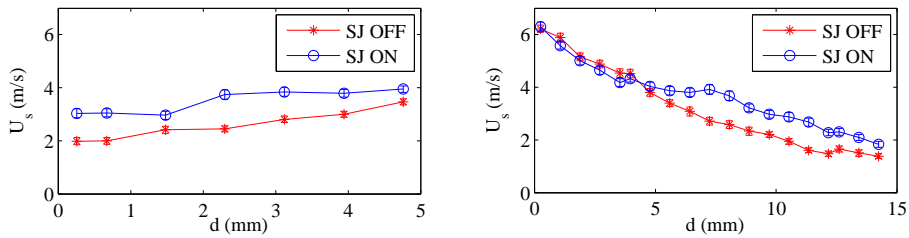


Figure 4.14: Velocity profiles (Case 5): longitudinal axis (left) and transverse axis (right).

vortices in a given plane cross section, and study the local effect of the synthetic jet on the spray within the impact region. The vorticity field has been evaluated using Dynamic Studio software of the Dantec Dynamics. In next Figures 4.17-4.24 a visualization of the velocity fields is presented along with the corresponding vorticity maps. Throughout all the maps shown in these figures the velocity values are reported in m/s , and the vorticity ones in $1/s$. Various actuation situations for two different injection pressures (5 MPa and 10 MPa), and two spray/jet relative locations ($h = 0$ mm and $h = 10$ mm) have been compared to the analogous cases without actuation.

For both the injection pressures considered in the present investigation, a high vorticity region close to the nozzle tip is evident; as the spray impacts on the surrounding air, the first droplets on the liquid jet boundaries leave the spray due to the shear stresses acting on the interface between the water and air. The breakup is occurring and spray quickly reduces its

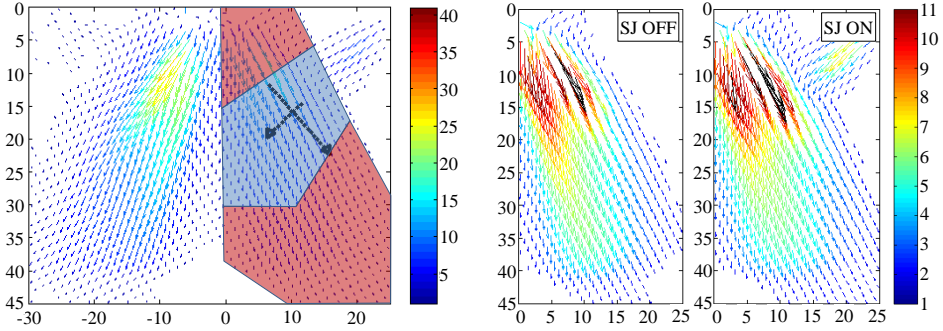


Figure 4.15: Case 6: Spray velocity field ($P_{inj} = 10$ MPa, $h = 10$ mm).

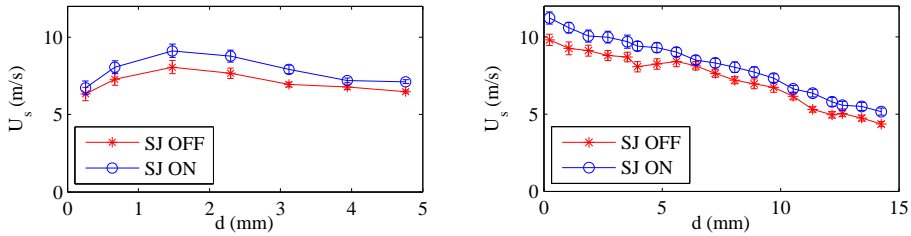


Figure 4.16: Velocity profiles (Case 6): longitudinal axis (left) and transverse axis (right).

momentum flux. At 5 MPa this region is located immediately outside the nozzle and sizes a few millimeters (Figure 4.17) . At 10 MPa the higher injection pressure induces a corresponding increase in momentum flux and the higher vorticity magnitude is extended to a region along the spray boundary, whose extension is about 15 mm (Figure 4.20). The nonuniform vorticity regions present at the top right corners of both figures are due to occasional disturbances in the chamber test.

Looking at the effect of the synthetic jet on the water spray, the vorticity analysis confirms the findings reported in the previous sections. Moving the injector downstream decreases the distance between SJ device and spray nozzle, leading to a softer impact of the synthetic jet onto the spray. This provides lower values of the vorticity magnitude in the impact zone, as is shown in Figures 4.18 and 4.19, which refer to the injection pressure of 5 MPa and to the cases of $h = 0$ mm and $h = 10$ mm, respectively. This

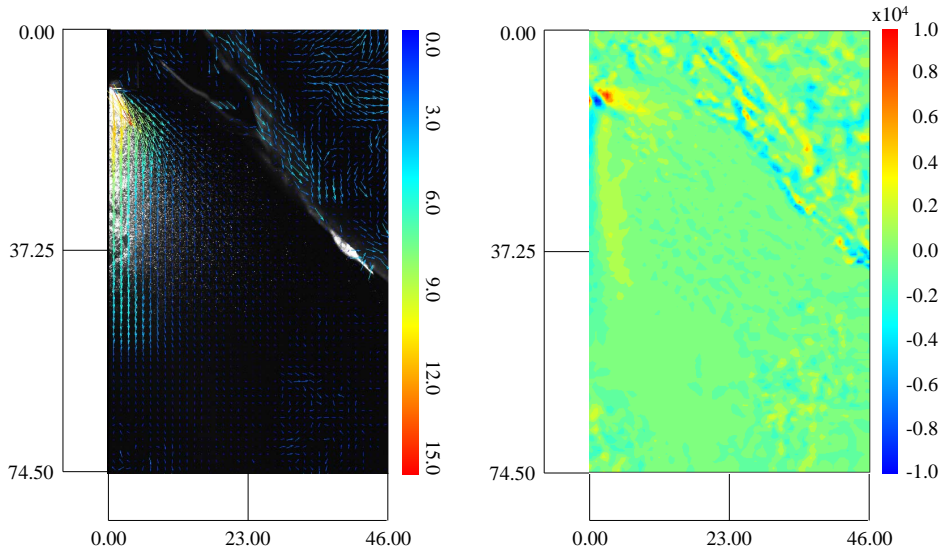


Figure 4.17: No SJ actuation, 5 MPa: velocity field (left), vorticity field (right).

occurrence is more clearly visible in Figures 4.21 and 4.22, which refer to the injection pressure of 10 MPa and to the cases of $h = 0\text{mm}$ and $h = 10\text{mm}$, respectively.

A zoom view of velocity and vorticity fields is reported in Figures 4.23 and 4.24 for the usual injection pressures and $h = 0\text{mm}$. The highest vorticity values are obtained for the higher pressure case, and also the interaction region is characterized by higher values of the vorticity. Due to the increased spray velocity the impact is sharper and the interaction zone is limited to a few millimeters. Even if the synthetic jet is not strong enough to influence the spray atomization, Figures 4.23 and 4.24 highlight a dilution effect in the region downstream of the impact as is argued by the strong light intensity reduction.

Moreover, looking at the zone close to the synthetic jet orifice, depending on the injection pressure, a different vorticity magnitude seems to be produced. However, this is not a physical effect, but it is related to the number of seeding droplets. For the higher pressure the seeding particles can reach a region closer to the orifice where the vorticity is higher. The

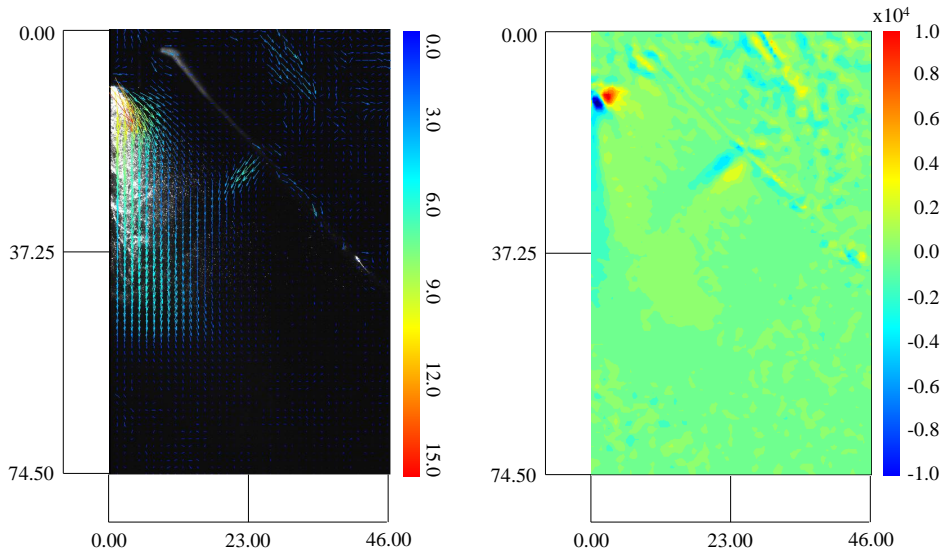


Figure 4.18: Case 1 (5 MPa, $h = 0\text{mm}$): velocity field (left), vorticity field (right).

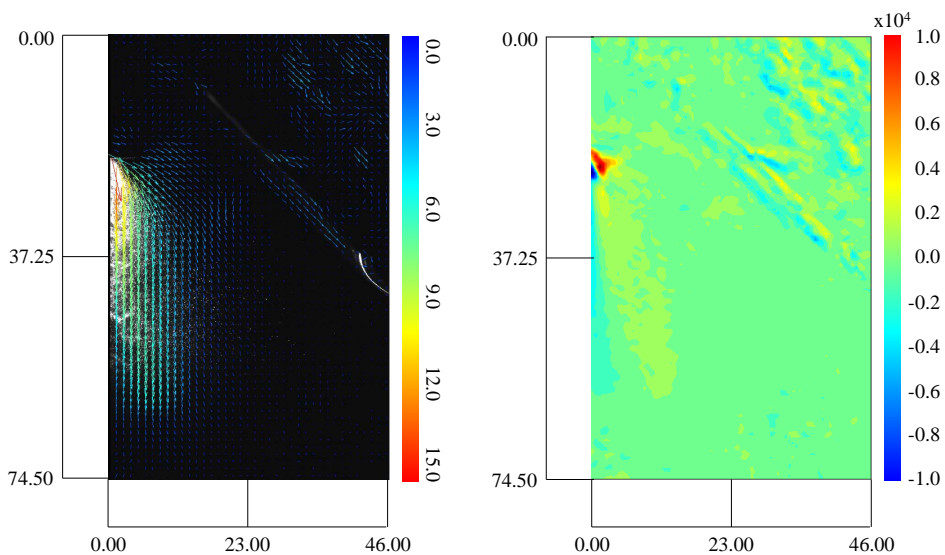


Figure 4.19: Case 5 (5 MPa, $h = 10\text{mm}$): velocity field (left), vorticity field (right).

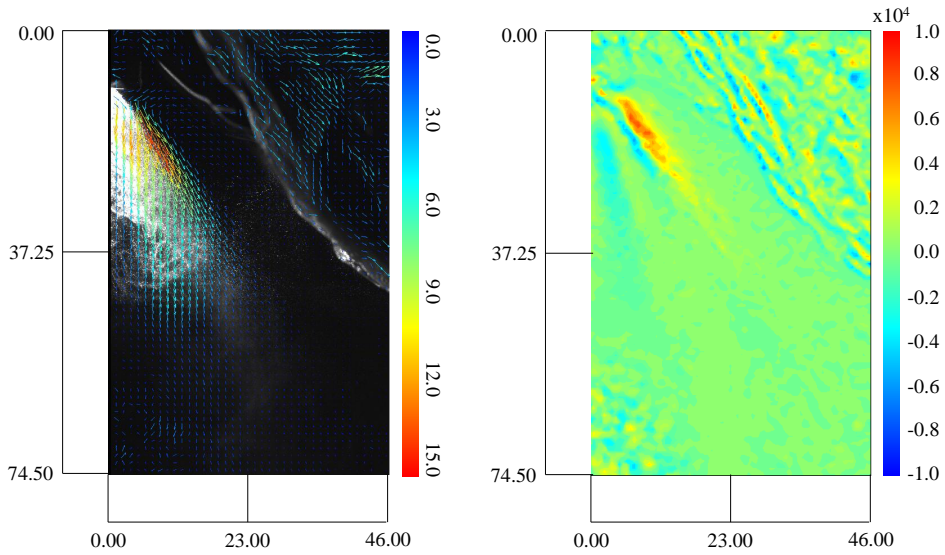


Figure 4.20: No SJ actuation, 10 MPa: velocity field (left), vorticity field (right).

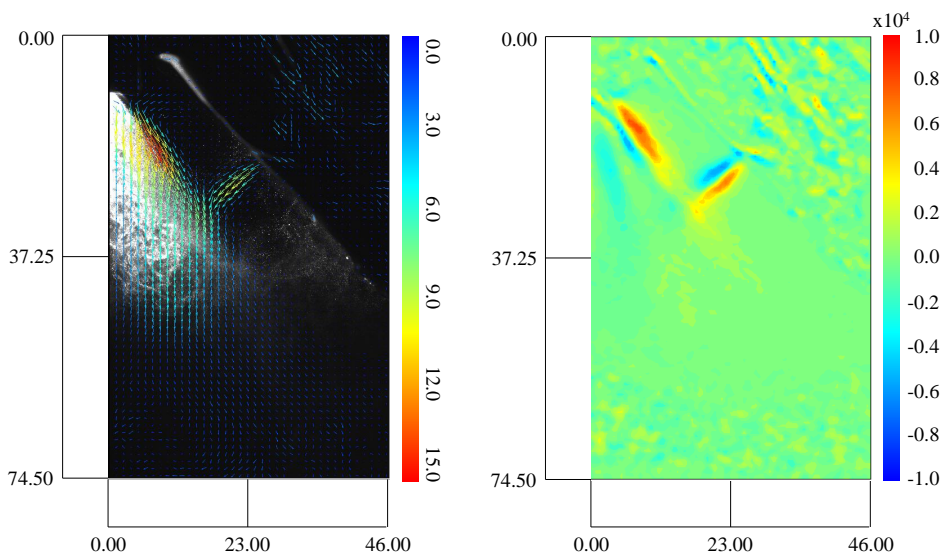


Figure 4.21: Case 2 (10 MPa, $h = 0\text{mm}$): velocity field (left), vorticity field (right).

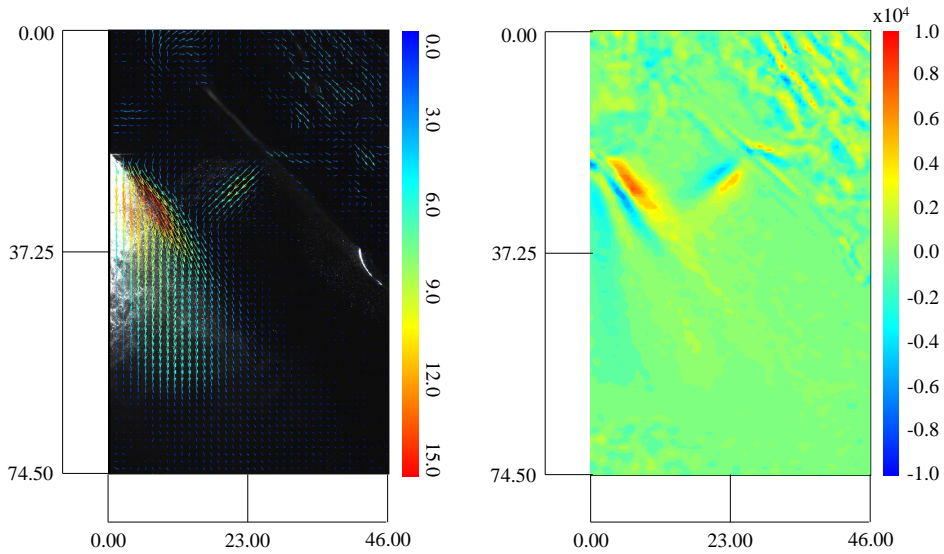


Figure 4.22: Case 6 (10 MPa, $h = 10\text{mm}$): velocity field (left), vorticity field (right).

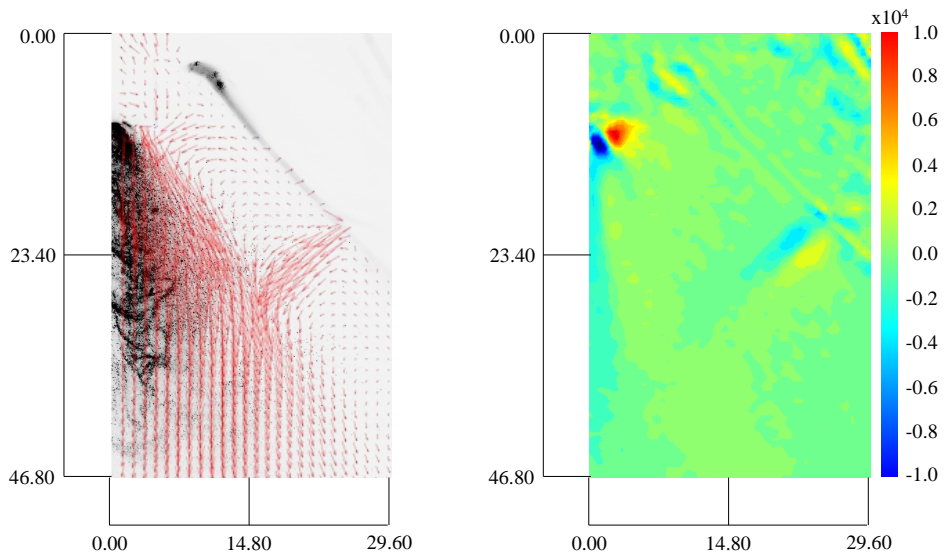


Figure 4.23: Case 1 (5 MPa, $h = 0\text{mm}$): velocity vector fields (left), vorticity field (right) in the impact region.

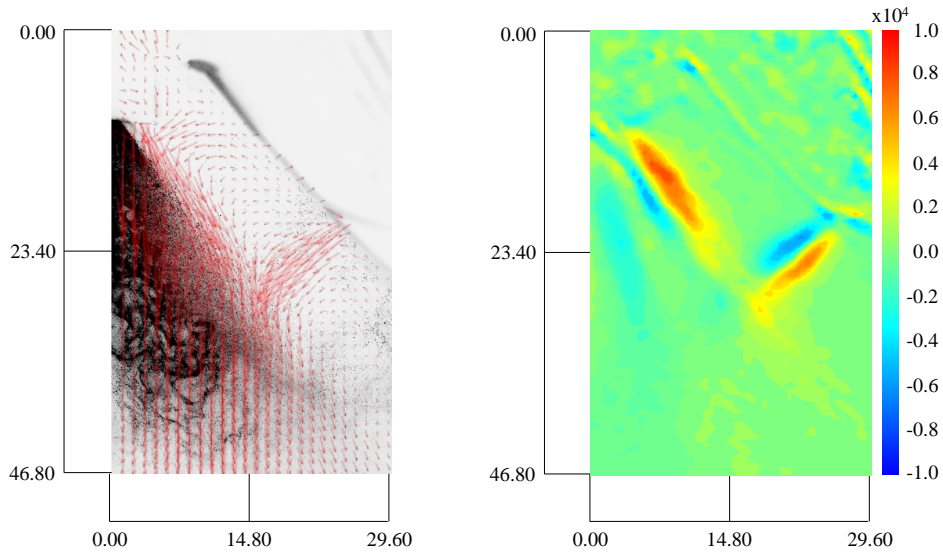


Figure 4.24: Case 2 (10 MPa, $h = 0$ mm): velocity vector fields (left), vorticity field (right) in the impact region.

same situation can be observed by changing the nozzle position: when the impact point is next to the orifice, there are more seeding particles and PIV results are more accurate in that zone.

List of Symbols - Part I

Roman symbols

A_o	orifice area
A_w	diaphragm/wall area
ADC	acoustic damping coefficient
c	air speed of sound
C_w	acoustic compliance of the diaphragm
C_μ	momentum coefficient
C_μ^*	modified momentum coefficient
C_H	Helmholtz stiffness
C_{wH}	coupling stiffness
C_{wtot}	total diaphragm stiffness
CF	coupling factor
\bar{D}_s	power dissipation due to the structural damping effects
\bar{D}_f	power dissipation due to the head loss at the orifice
d_a	effective acoustic piezoceramic coefficient
d_o	orifice diameter
d_{pc}	piezoceramic diameter
d_w	diaphragm diameter
E	energy
E_{pc}	Young's modulus of the piezoceramic
E_w	Young's modulus of the diaphragm shim
$e(t)$	effort
F	force
F_o	force amplitude
f	frequency
$f(t)$	flow
f_1	modified structural resonance frequency without damping
f_2	modified Helmholtz resonance frequency without damping

List of Symbols - Part I

f_H	Helmholtz resonance frequency
f_n	natural coupled frequency
f_w	diaphragm (structural) resonance frequency
\tilde{f}_w	frequency of the principal mode of vibration of a rigidly clamped disk
H	cavity height
I	current
K	head loss coefficient
k_a	air equivalent stiffness
k_w	diaphragm equivalent stiffness
\bar{L}	stroke length
\mathcal{L}_a	orifice air mass
\mathcal{L}_w	diaphragm air mass
l_e	effective length of the orifice
l_o	orifice length
m_a	mass of the air at the orifice
m_w	diaphragm mass
m_{wt}	diaphragm total mass
\bar{P}_e	electrodynamic power
\bar{P}_j	external Joule power
\bar{P}_l	kinetic power
\bar{P}_m	mechanical power
p	differential pressure
p_a	ambient pressure
p_i	cavity (internal) differential pressure
p_j	injection pressure
Q	volumetric flow rate
\mathcal{R}_a	fluidic damping factor
\mathcal{R}_w	structural damping factor
Re	Reynolds number
S	Stokes number
St	Strouhal number
t	time instant
th_{pc}	piezoceramic thickness
th_w	diaphragm thickness
x_w	diaphragm average displacement
U	instantaneous orifice jet-flow velocity
\bar{U}	velocity stroke length
U_e	cycle-averaged jet-flow velocity at saddle point
U_{inc}	incompressible velocity

U_o	momentum velocity
U_{max}	jet-flow velocity peak at orifice
U_s	spray velocity
V_{ac}	voltage amplitude
V_c	cavity volume
V_w	diaphragm average velocity
Z_c	cavity total impedance
Z_o	orifice total impedance
Z_w	diaphragm/wall total impedance

Greek symbols

$\overline{\Delta E}$	total energy variation
Δl_e	additive constant of the effective orifice length
Δx_w	average linear membrane displacement
ΔV	cavity volume variation
Φ_a	electroacoustic transduction coefficient
Φ_{V_w}	diaphragm velocity phase angle
Φ_U	jet velocity phase angle
γ	specific heats ratio
η	actuator (global) efficiency
η_e	electrodynamic transduction efficiency
η_k	kinetic efficiency
ν_w	Poisson's modulus of the diaphragm
ν_{pc}	Poisson's modulus of the piezoceramic
ρ_a	air density
ρ_w	diaphragm density
ω	$2\pi f$, circular frequency
$\omega_{1,2}$	$2\pi f_{1,2}$
ω_H	$2\pi f_H$
ω_n	$2\pi f_n$
ω_w	$2\pi f_w$
ω_{wc}	frequency of the pneumatic spring
ω_z	out-of-plane component vorticity field
ζ_w	diaphragm damping ratio

Sub- and Superscripts

H	Helmholtz
i	internal cavity
o	orifice
w	wall, diaphragm

Acronyms

AFC	Active Flow Control
CFD	Computational Fluid Dynamics
DBD	Dielectric Barrier Discharge
DNS	Direct Numerical Simulation
LEM	Lumped Element Model
LES	Large Eddy Simulation
MAV	Micro Air Vehicle
PIV	Particle Image Velocimetry
PDA	Phase Doppler Anemometry
PTV	Particle Tracking Velocimetry
RANS	Reynolds Averaged Navier-Stokes
SJ	Synthetic Jets
ZNMF	Zero-Net Mass-Flux

Part II

**Plasma Synthetic Jet
Actuators**

Chapter 5

Plasma synthetic jet actuators

5.1 Introduction

In the last few years, plasma synthetic jet actuators have gained much interest among the active flow control methods, thanks to their simplicity, very short response time, high velocities and lack of any moving parts. A PSJ actuator, or Sparkjet, is a device developed originally at the Johns Hopkins University (Grossmann et al. [23, 24]), at the beginning of the century, and soon it has become the object of study of several research groups (e.g. Narayanaswamy et al. [81] and Caruana et al. [82]).

As depicted in Figure 5.1, it is mainly composed of 2 or 3 electrodes embedded in a small cavity linked to the external environment through an orifice. The operating cycle begins with an electrical discharge between the electrodes, which sharply increases pressure and temperature inside the cavity. The high-pressure air exhausts through the orifice, converting the increased air internal energy into kinetic one. In the end, fresh air is drawn back inside the cavity, refilling the device for the next pulse. After a limited number of cycles the device reaches a periodic behavior, generating a so-called plasma synthetic jet.

Different numerical models have been developed to predict the behavior of the device. The first one was presented by Haack et al. [83], who divided

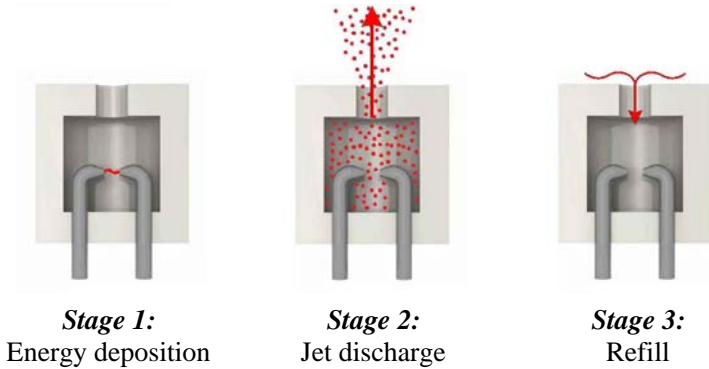


Figure 5.1: Different phases of the PSJ operating cycle.

the actuator operating cycle in three different stages: energy deposition, discharge and refresh. It was a one-dimensional analytical model based on isentropic behavior, unable to treat the refresh stage and limited to a single flow discharge. Another attempt was made by Anderson and Knight [84], who carried a one-dimensional analysis focused on the different parameters which can affect the actuator performances. A more detailed numerical investigation was carried out by Sary et al. [85], who solved the 2-D inviscid Euler equations by means of an explicit Roe scheme, coupled via a Joule heating source term to a second model to describe the arc discharge. They simulated the periodic behavior of the actuator, performing a parametric analysis by varying both the energy deposition and the cavity geometry. With the same basic work, Laurendeau et al. [86] used a LES approach to catch the transient development of a plasma synthetic jet and Chedeveigne et al. [87] studied the interaction of a micro-jet generated by a PSJ actuator with a high-Reynolds number isothermal flow. Recently, Zong et al. [88, 89] proposed a lumped-element model, corroborated with experimental measurements, in which heat dissipation terms are assumed to vary linearly with cavity temperature and the flow is considered isentropic or politropic.

PSJ actuators have been also experimentally characterized. The first measurements were taken at the Johns Hopkins University, where a large variety of actuators were tested for different operating and geometrical conditions, such as the orifice diameter, the trigger mechanism, the number of

orifices and the operating frequency, see Cybyk et al. [90] and Haack et al. [91]. Tests were conducted in quiescent and in supersonic flow fields (Emerick et al. [92]), controlling also the shock waves/turbulent boundary layer interaction on a compression ramp (Narayanaswamy et al. [93]). Reedy et al. [94] used both Schlieren imaging and Particle Image Velocimetry optical techniques to determine the maximum jet velocity. More recently, Belinger et al. [95, 96] carried out electrical and optical analyses on the electrical discharge and Caruana et al. [82] presented an experimental characterization of a PSJ device with and without crossflow, providing insights on the ability of actuators to reduce the separated flow region on a decelerating ramp and on a NACA-0015 airfoil. Finally, Zong et al. [97, 98] and Zhang et al. [99] provided further information about the influence of capacity energy, discharge location and geometrical parameters on the performance of PSJ actuators.

Following the research line of the lumped models, which are very useful for design and manufacturing practical purposes, in this chapter a novel physical model is presented, Chiatto and de Luca [100]. It is able to predict the time variation of all thermodynamic variables in the cavity as well as the jet velocity at the orifice, as functions of the operating frequency. It is worth noting that the present work can be considered as an extension of Zong's proposal, because the governing equations are fully gasdynamics based and are enforced on the whole control volume without the isentropic assumption. The correct simulation of the refill regime is guaranteed by the inertial term included in the unsteady Bernoulli's equation. Furthermore, the model has been validated first, through a comparison with data available in literature, and then with measurements obtained using a house-made PSJ actuator (Chapter 6).

5.2 Physical model

The PSJ device is modeled as a cylindrical geometry cavity, with height H and diameter D (the corresponding volume is V_c), and a cylindrical nozzle of length l and diameter d . All variables referring to the cavity are indicated with the subscript c , while those concerning the exit nozzle with subscript

e. A sketch of the actuator is reported in Figure 5.2.

The mean variables involved in the problem are the thermodynamic properties inside the cavity (ρ_c, T_c, p_c) and the thermo-fluid dynamic properties at nozzle exit (ρ_e, T_e, p_e, U) where ρ, T, p are air density, temperature and pressure, respectively, and U denotes the jet velocity at nozzle exit section. The governing equations are based on two main assumptions. First of all, the model is lumped, namely thermodynamic and transport properties are averaged in the whole cavity volume. Furthermore, according to Dufour et al. [101], the flow is considered as a mixture of gases in thermodynamic equilibrium (LTE hypothesis) with respect to the instantaneous values of pressure and temperature. In the present work, since pressure variations are relatively small, transport parameters are calculated with analytical expressions given by Capitelli et al. [102], in which all coefficients are given as function of the temperature only.

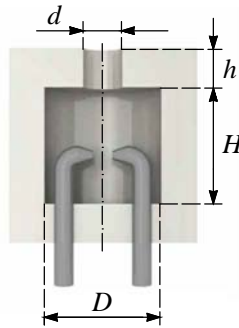


Figure 5.2: Sketch of the actuator with the geometric variables.

5.2.1 Energy deposition

The energy deposition is a very complex process which involves different stages, each characterized by its own efficiency, which is due to various electrical and physical effects that reduce the amount of energy transferred to the fluid in each discharge, Popkin et al. [103]. A first efficiency, η_a , is ratio of the arc energy, E_a , to the energy provided by the external dc power supply, E_{dc} ; this reduced conversion of energy is due to the parasitic resistances

and inductances of the circuit components (wires, diodes, capacitors). The efficiency η_a is a function of the electrodes distance and of the discharge current. Moreover, the arc discharge energy is not entirely transferred into the kinetic energy of the fluid, because a considerable part is dissipated by the radiative and conductive heat transfer mechanisms, Zong et al. [89]. Therefore it is necessary to introduce another efficiency η_f , which takes into account also the non-uniform heating effects of the arc discharge, and finally a total efficiency $\eta_{tot} = \eta_a \cdot \eta_f$ is considered. For actuators of the type considered here a typical value of η_{tot} is 0.35, which will be assumed hereafter in LEM calculations.

When the discharge time is very short, $T_d \approx 0 \mu s$, the energy deposition process can be considered instantaneous because, according to Belinger et al. [95, 96], the spark discharge occurs in only a few μs , providing an amount of energy of some mJ. Usually this occurs for a capacitor-based supply system, in which the discharge time is governed by the electrical characteristics of the capacitors within the circuit. In these conditions, the energy deposition takes place in such a short time that the heating process can be modeled as a constant mass transformation; because the cavity volume does not change during the whole cycle, this phase is modeled as a constant specific volume process.

In each cycle, after the energy discharge, the state variables can be easily calculated with the following equations system, in which the subscript i represents the condition before the arc formation process. For the boot cycle this condition coincides with the ambient one, while for a generic cycle, the thermodynamic initial condition coincides with that of the previous cycle:

$$\begin{cases} \rho_c = \rho_i \\ T_c = T_i + E_f / (M_{ci} c_v(T_i)) \\ p_c = \rho_i R(T_c) T_c \end{cases} \quad (5.1)$$

in which $R(T)$ is the air gas constant and it is temperature dependent because it includes compressibility effects, i.e. $R(T) = R_0 Z(T)$, with R_0 being the air gas constant at standard conditions. $E_f = \eta_{tot} \cdot E_{tot}$ is the effective amount of energy supplied to the fluid, M_{ci} is the air mass and c_v the constant volume specific heat.

5.2.2 Discharge and Refresh phases

Once the energy release has occurred, high-pressure fluid exhausts through the orifice, converting its increased internal energy into the kinetic one. This phase can be simulated as the discharge process of a reservoir connected to the external ambient by means of a relatively short nozzle, or orifice. The application of the mass conservation law to the system composed of the reservoir and the nozzle leads to the following relationship:

$$\frac{d\rho_c}{dt} = -\frac{\rho_e U A_e}{V_c} \quad (5.2)$$

with U indicating the exit velocity, A_e the orifice area, t the time.

The energy equation inside the whole cavity volume has to be enforced too:

$$\left[\rho_c \frac{d}{dt}(u_c) + u_c \frac{d}{dt}(\rho_c) \right] V_c + \rho_e \left(h_e + \frac{U^2}{2} \right) U A_e + \dot{Q} = 0 \quad (5.3)$$

where u and h are internal energy and thermodynamic enthalpy, respectively, and \dot{Q} is the total amount of heat power exchanged through the entire surface of the system, as will be discussed in more detail in the last part of this paragraph.

It is worth noting that Equation (5.3) is valid for $T_d \approx 0 \mu\text{s}$; however, when the discharge time is significantly longer, the energy deposition can not be considered a constant volume process anymore, because the ejection and the heating processes occur simultaneously. In this case, the energy deposition does not need to be modeled as an independent process, but it should be treated as a jet stage with both heat input (arc energy discharge) and output (heat losses through the actuator walls.) terms, Zong et al. [89]. By combining Equation (5.3) and Equation (5.1), it is possible to obtain:

$$\left[\rho_c \frac{d}{dt}(u_c) + u_c \frac{d}{dt}(\rho_c) \right] V_c + \rho_e \left(h_e + \frac{U^2}{2} \right) U A_e + \dot{Q} - \frac{E_f}{T_d} = 0 \quad (5.4)$$

The application of the compressible unsteady Bernoulli's equation, between a point inside the cavity (where the flow velocity is practically null)

and the exit section of the nozzle, yields a third equation for these phases:

$$u_c + \frac{p_c}{\rho_c} = u_e + \frac{p_e}{\rho_e} + l_e \frac{\partial U}{\partial t} + K \frac{|U|U}{2} \quad (5.5)$$

where K is the head loss coefficient, including entrance/exit losses at exit orifice; l_e is the modified effective length, representing the distance between the two points of application of Bernoulli's equation.

The choice of the values for the head loss coefficient and the effective length has been treated in various previous papers. For piezo-driven synthetic jets, usually these terms have been determined by making a best fitting between numerical and experimental data or by using some empirical expressions, see de Luca et al. [55]. Due to the lack of literature works on this topic for PSJ actuators, in the present chapter the previous quantities have been considered as fitting parameters and their values have been determined by matching the results of the lumped model with numerical simulations made with OpenFOAM computer code; more details will be reported in paragraph 5.3.1.

Another convenient equation for the flow along the nozzle is the classic isentropic relationship linking the thermodynamic properties inside the cavity to those at the orifice exit:

$$T_c = T_e \frac{c_p(T_e)}{c_p(T_c)} \left[1 + \frac{\gamma(T_e) - 1}{2} M_e^2 \right] \quad (5.6)$$

with γ being the specific heats ratio, which in the present case of real gas is considered as a function of the temperature.

The exit flow condition, namely choked or unchoked flow, selects the equation required to close the problem. The establishment of a condition or the other one depends on the critical ratio of the cavity pressure to the exit pressure, i.e.

$$\frac{p_c}{p_e} \Big|_{cr} = \left(\frac{\bar{\gamma} + 1}{2} \right)^{\frac{\bar{\gamma}}{\bar{\gamma}-1}} \quad (5.7)$$

where $\bar{\gamma}$ is the mean value between the two states (i.e., cavity and exit section) involved. If the pressure ratio, after the energy deposition, is greater than or equals the one computed with Equation (5.7), the flow is choked,

otherwise an unchoked regime is assumed.

For choked flow, the nozzle exit condition is that the exit Mach number is sonic:

$$M_e = \frac{U}{\sqrt{\gamma(T_e)R(T_e)T_e}} = 1 \quad (5.8)$$

On the other hand, if the flow is unchoked, the Kutta condition is imposed:

$$p_e = p_a \quad (5.9)$$

where p_a denotes the external ambient pressure.

In conclusion, the model is constituted by three ordinary differential equations, Equations (5.2), (5.3), (5.5)), and a non-linear algebraic relation Equation (5.6), that should be particularized for the exit conditions, Equation (5.8) or Equation (5.9). The procedure carried out to obtain the governing equations and their summary is reported in Appendix A.

Heat transfer

The total heat power \dot{Q} , included in the cavity energy balance (Equation (5.3)), is considered as the sum of two terms: the first due to the external natural convection mechanism, while the second due to the radiative heat transfer.

$$\dot{Q} = \dot{Q}_{conv} + Q_{rad} = h_{conv} S_{conv} (T_c - T_a) + \varepsilon \sigma S_{rad} (T_c^4 - T_a^4) \quad (5.10)$$

where S_{conv} and S_{rad} are the exchange surface and the relevant surface of emission, respectively, h_{conv} is the convective heat transfer coefficient (equal to $50 \text{ Wm}^{-2}\text{K}^{-1}$, according to Sary et al. [85]), T_a is the external ambient temperature, ε is the emissivity coefficient (in the case of ceramic material it is equal to about 0.8) and σ is the Stefan-Boltzmann constant. Note that here the cavity wall is supposed to constitute a vanishing thermal resistance, which is validated by the occurrence of a very small Biot number.

5.3 LEM Results

In all test cases, the flow has been initialized at rest ($U = 0$ m/s) and standard ambient thermodynamic conditions ($T_a = 288$ K and $p_a = 101325$ Pa). It should be emphasized that for all the operating conditions considered in the present chapter the air jet issues in the external ambient in unchoked flow regime.

5.3.1 Multidimensional CFD Simulation Set-up

As mentioned in the previous section, the head loss coefficient, K , and the effective orifice length, l_e , have been considered as fitting parameters and their values have been determined by matching the results of the lumped model with detailed multidimensional CFD simulations obtained with OpenFOAM computer code. This is an open-source CFD toolbox with GNU license which nowadays is widely used for a large variety of thermo-fluid-dynamics problems, [104, 105]). The amount of energy supplied to the fluid for each cycle is $E_d = 7$ mJ; the grid developed for the computations is fully structured; it consists of a wedge shaped thin slice, with a 5° opening angle, having the longitudinal sharp edge on the symmetry axis. A representation of the mesh is presented in Figure 5.3 depicting the actuator and the external environment (where the jet issues and the mixing layer develops), which is modeled with 46040 cells. The computational domain is $60 d$ long and $30 d$ wide in radial direction.

The boundary conditions here enforced are of no-slip at the solid walls and inlet/outlet at the permeable control surfaces; symmetric flow is enforced on the symmetry axis. A nonlinear mixed boundary condition has been imposed on the temperature at cavity walls to account for convective and radiative heat fluxes towards the external ambient; for each boundary cell, in the general case, it reads:

$$-\lambda \frac{\partial T}{\partial n} \Big|_w = h_{conv} (T_w - T_a) + \varepsilon \sigma (T_w^4 - T_a^4) \quad (5.11)$$

where n is the unit vector normal to the wall, oriented outward, ε is the surface emissivity coefficient, σ is the Stefan-Boltzmann constant and λ is the

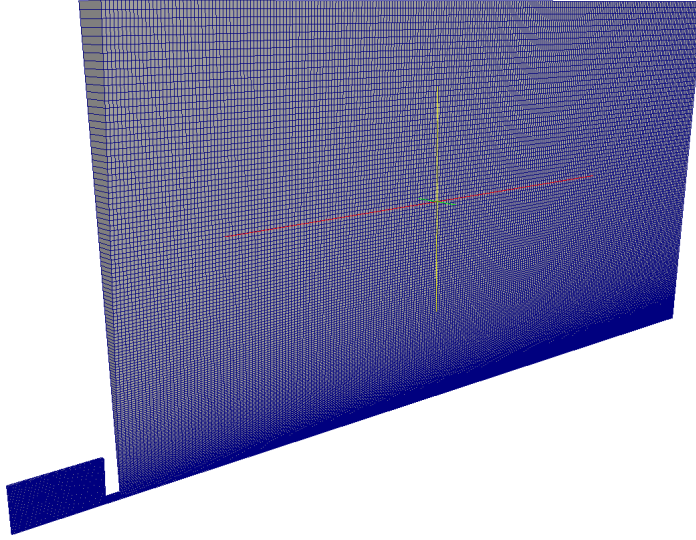


Figure 5.3: Mesh representation for the wedge used in the numerical simulation.

thermal conductivity of the air. It has to be noticed again that it is assumed a vanishing thermal resistance of the cavity wall. The transport variables are evaluated with the JANAF tables, and viscosity coefficient with the Sutherland's law. The energy deposition has been considered instantaneous, and it is abruptly transferred to the whole cavity volume. Typical integration time step is about $1 \mu s$, which is perfectly suitable to detect high frequency time oscillations of the field quantities.

Figure 5.4 depicts the time trend of the major thermo-fluid-dynamic quantities, such as jet exit velocity, mean cavity pressure, temperature and mass, monitored during the start-up first cycle. Data of Figure 5.4 (left) shows that the initial energy discharge produces a sudden increase of pressure (from the ambient value) which forces the air to exit from the orifice in a few microseconds; the jet velocity, in fact, reaches its maximum about $30 \mu s$ after the discharge, then it decreases rapidly fluctuating slightly around zero. Moreover, during this cycle the jets expels about 10% of its initial mass, while the cavity average temperature, after the steep rise caused by the electrical discharge, at first decreases sharply due to the enthalpy con-

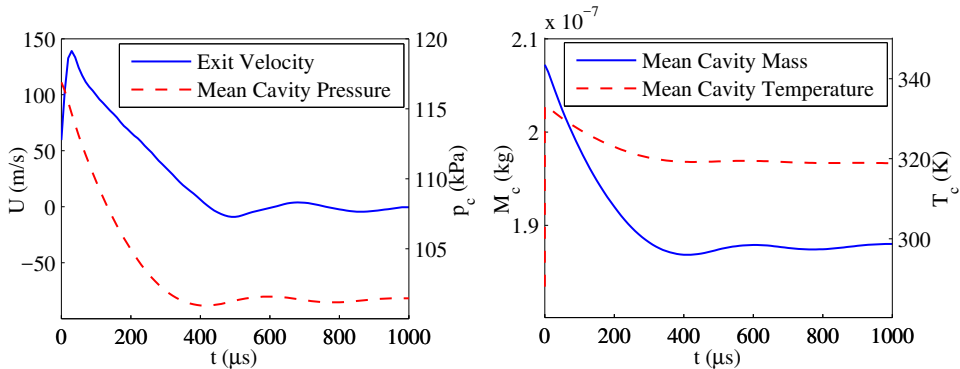


Figure 5.4: Time variation of thermo-fluid-dynamic quantities during the start-up cycle computed with OpenFOAM. (left) Jet exit velocity and mean cavity pressure; (right) mean cavity mass and temperature.

vective exchange induced by the issuing fluid flow, then more slowly driven by heat transfer effects, as shown in Figure 5.4 (right).

5.3.2 LEM calibration and analysis of single cycle

The lumped-element governing equations have been implemented in *Matlab* code and integrated with a Runge-Kutta method (*ode45*). According to de Luca et al. [55, 60], the effective orifice length has been evaluated as: $l_e/d = l/d + \Delta l_e$, setting $\Delta l_e = 1.5$ and $K = 1.78$, making a best fit with the CFD numerical results. These values have been assumed throughout in the computations hereafter presented. Note that for these simulations a zero discharge time ($T_d \approx 0 \mu$ s) has been assumed.

Figure 5.5 shows a very good agreement between lumped-element model and CFD simulation results, with particular emphasis on the start-up first cycle of operation. More in detail, LEM predicts a higher amplitude of oscillation after the initial peak, which is particularly evident for the jet velocity temporal evolution. Furthermore, the LEM model estimates a lower peak jet velocity and a slightly higher amount of mass expelled during the first cycle. The agreement of pressure evolution seems better and generally the period of the oscillations is well predicted.

One cycle only is not enough to generate a synthetic jet, in the sense

that the system needs a certain number of initial cycles before to reach the quasi-periodic operation regime. However, the analysis of the first cycle not only is crucial to calibrate the LEM code, but it provides some important details of the system response.

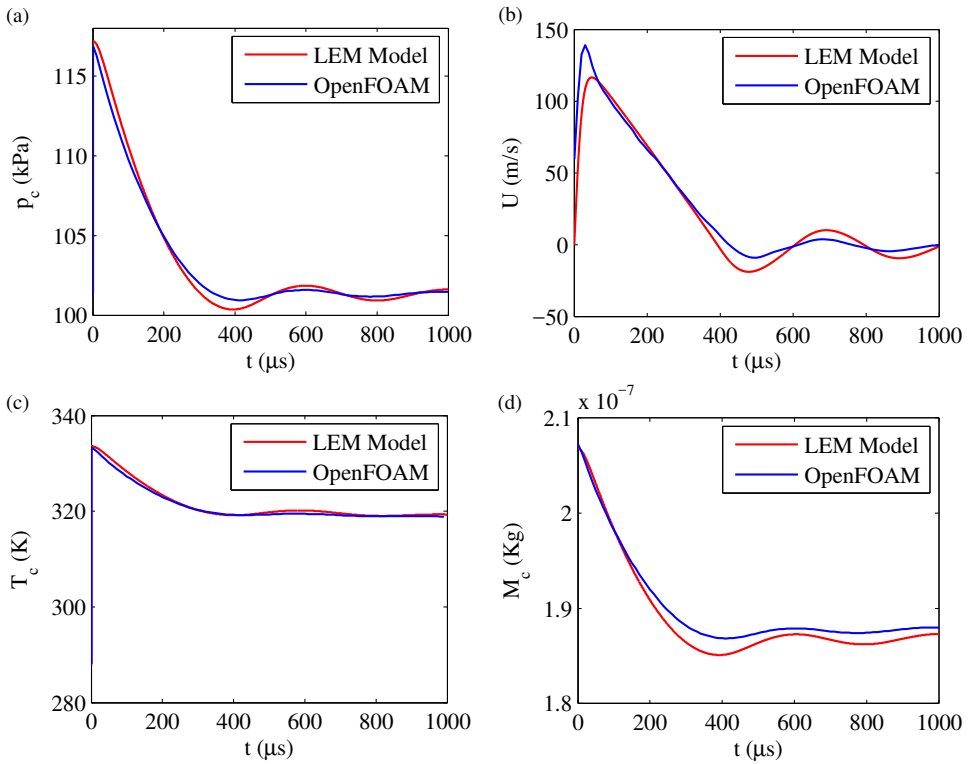


Figure 5.5: Comparison of results of LEM model (red) and OpenFOAM code (blue). (a) Mean cavity pressure, (b) exit velocity, (c) mean cavity temperature and (d) mean cavity mass.

In the time interval between two subsequent discharge pulses, the device seems to behave like a Helmholtz resonator, as also observed by Caruana et al. [106]. In this case the oscillating mass is represented by the air inside the exit orifice and oscillations are caused by the stiffness of the air contained in the cavity. This occurrence has been already found during the operation of piezo-driven synthetic jet actuators, which is characterized by two natural frequencies: the membrane first-mode structural one and

the Helmholtz one, as deeply analyzed in Chapter 2. In the absence of mechanical moving parts, which is the case of plasma jet devices, however, the only Helmholtz natural frequency is expected, that can be written as:

$$f_H = \frac{1}{2\pi} \sqrt{\frac{\gamma(T_c) A_e^2 p_c / V_c}{\bar{\rho} l A_e}} = \frac{1}{2\pi} \sqrt{\frac{k_a}{M_a}} \quad (5.12)$$

where $\bar{\rho} = (\rho_c + \rho_e)/2$, whereas k_a and M_a are, respectively, the equivalent stiffness of the air inside the cavity and the effective mass of the air at the orifice. Note that in the previous equation all thermodynamic variables are time-dependent, and accordingly the computed frequency varies till the synthetic jet is completely formed and the quasi-periodic regime is fully established. In general, the spread between the frequencies computed with Equation (5.12), f_H , and the values yielded by the LEM code, f_{LEM} , is within $1 \div 2\%$ for each discharge. For the first cycle, for example, these values are $f_H = 2447$ and $f_{LEM} = 2423$ Hz with an error lower than 1%.

5.3.3 Analysis of periodic behavior

The periodic behavior of the actuator has been simulated providing periodically to the fluid a fixed amount of energy, $E_d = 7$ mJ, with an actuation frequency of 1 kHz. The evolution of the main thermo-fluid-dynamic parameters, computed over the first 25 cycles, is represented in Figure 5.6.

Overall, the evolution is characterized by an initial transitional phase, with significant changes from the initial values; then, after about 20 ms, a repetitive quasi-periodic regime is reached, leading to the formation of a truly developed synthetic jet (namely, zero-net mass flow rate per cycle). After start-up, the cavity mass globally decreases, while the fluid within becomes increasingly hot, reaching temperatures higher than 800 K. Note that heat transfer effects constitute the leading terms during the refill regime, affecting the slope of the mass time trend during the refill regimes. When the fluid gets hotter, heat fluxes increase, promoting mass suction and thus the synthetic jet formation. The velocity reaches a peak of 180 m/s oscillating around small negative values. Similarly, the cavity pressure fluctuates around a value slightly lower than the ambient pressure with over-pressures

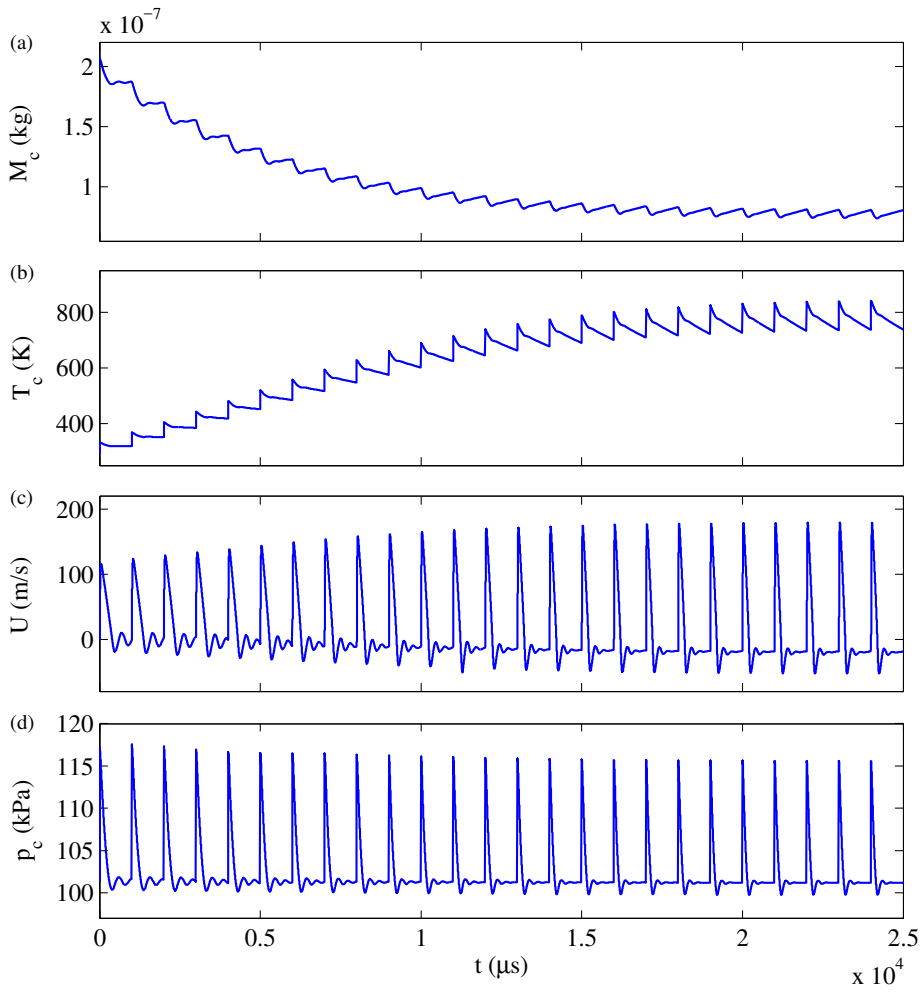


Figure 5.6: Evolution of the main thermo-fluid-dynamic parameters of the actuator over the first 25 cycles.

close to 16 kPa.

It is interesting to observe again the presence of high frequency oscillations between two subsequent energy depositions. As temperature tends to increase and density to reduce, the relationship (5.12) of the Helmholtz natural frequency predicts higher values during the operation mode; this is exactly what is underlined especially in Figure 5.6 (c) and (d), referring to jet exit velocity and cavity pressure.

5.3.4 Frequency response

The variation of the maximum peak velocity U_{max} with discharge frequency f is reported in Figure 5.7. The curve is computed considering 100 operating cycles for each frequency in order to reach the periodic behaviour of the device, taking the maximum peak velocity at the last cycle.

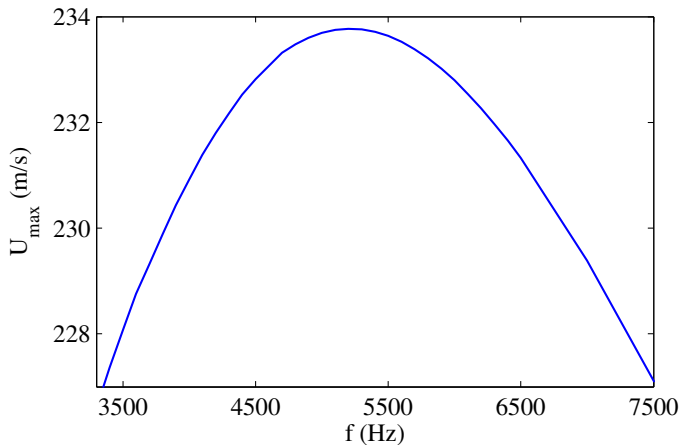


Figure 5.7: Variation of maximum peak velocity with discharge frequency.

It is worth noting that the curve exhibits a maximum around 3400 Hz, but it is not straightforward to predict theoretically this value because, as pointed out in the previous section, the Helmholtz natural frequency varies with the thermodynamic quantities, which in turn depend on the actuation frequency. Observe that the PSJ actuator frequency response appears quite different from that of piezo-driven actuators, see for instance Figure 2.11, exhibiting often very high velocity values even at relatively low frequencies.

It should be noted that, in spite of the relatively wide scale employed to represent the maximum peak velocity U_{max} , generally speaking the device frequency response is rather flat.

5.4 Comparison with literature models

Once calibrated the LEM code, its performances have been compared also with data retrieved by other literature models. The first comparison has been made with two different works of Zong et al. [88, 98], who proposed first, an analytical model in which the three stages of the device are described by using isentropic or politropic thermodynamic relationships, and then they computed the peak jet front velocity and its duration time starting from Schlieren images. The second one refers to the paper of Sary et al. [85], who solved the 2-D inviscid Euler equations by means of an explicit Roe scheme, coupled with an electric circuit model to consider the energy deposition between the electrodes.

5.4.1 Comparison with Zong's work

The work of Zong et al. [88] it is very interesting because these authors reported also experimental data. The device considered has geometric variables equal to: $D = 4$ mm, $H = 7$ mm and $d = 1$ mm. The amount of energy discharge is 5 mJ and the actuation frequency is 1 kHz. Figure 5.8 illustrates a comparison for cavity mass, temperature, pressure and jet exit velocity, with blue plots being the present model and the red ones those of the reference work.

Both models converge to similar periodic solutions, although some discrepancies arise during the initial phase. Furthermore, as can be seen especially in velocity and pressure trends, Zong's model predicts lower Helmholtz frequencies than the current model, which closely agrees with the theoretical prediction of Equation (5.12). More details about this difference can be appreciated in Figure 5.9, where the evolution of the exit velocity during 24th and 25th actuation cycles is reported.

The Helmholtz natural frequency computed with the Equation (5.12), when the device has reached a periodic behavior, is $f_H = 4768$ Hz, the

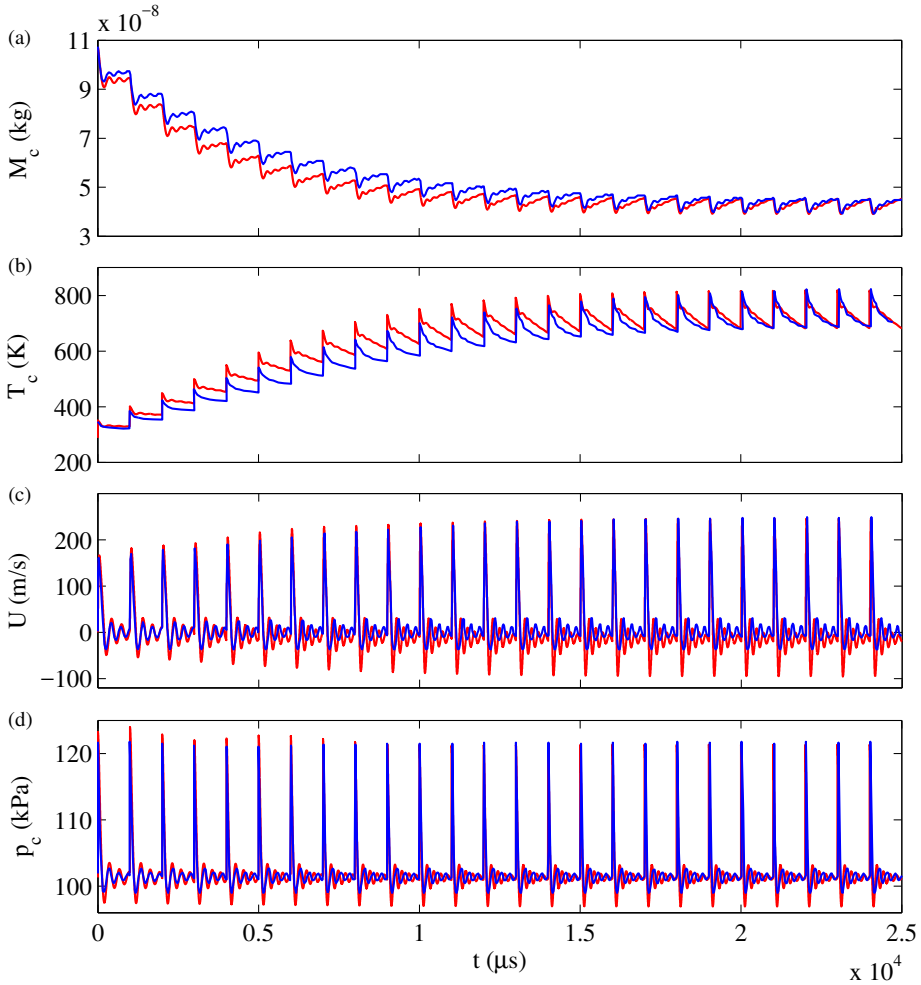


Figure 5.8: Evolution of main thermodynamic quantities over the first 25 cycles. Present model in red, Zong et al. [88] model in blue.

frequency predicted by the current model is $f_{LEM} = 4859$ Hz and the frequency determined by Zong et al. is about 3800 Hz. The corresponding spread values are, respectively, about 4% for the current model and about 18% for Zong’s evaluation.

Another important difference is linked to the heat transfer process. Since this process is the leading effect in the refill regime, the use of a “linear” heat transfer model leads to a different recharge velocity and affects the

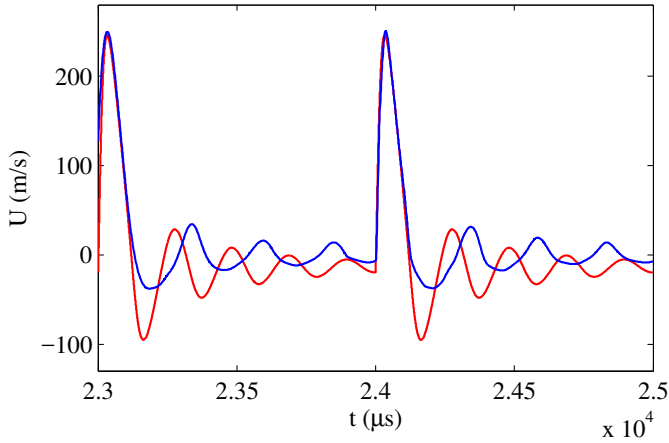


Figure 5.9: Evolution of the exit velocity for 24th and 25th actuation cycles. Present model in red, Zong et al. [88] model in blue.

time required to achieve the periodic behavior. This is clearly visible in the cavity mass evolution during the start-up phase. Note that overall solutions are quite similar because the amount of energy considered during the deposition stage leads to relatively low working temperatures. A greater amount of energy discharge would lead to a major deviation from the perfect gas behavior, producing different results between the two models in the quasi-periodic regime.

The variations of maximum cavity temperature, $T_{c,max}$, with actuation frequency has been also considered. Figure 5.10 illustrates the Zong's model results (blue line), as well as the estimated (through a "linear" heat transfer modeling) experimental values of the same authors (dashed black line), while the numerical solution of the present model is represented by the continuous red line. It is interesting to observe how the present LEM solution fits the experimental data better than the Zong's model itself. This discrepancy probably lies in some simplified assumptions of the Zong's model, such as linear heat transfer mechanism and constant transport quantities.

Another comparison has been carried out in the framework of a second work of Zong et al. [98]. They computed the peak jet front velocity and its duration time starting from Schlieren images. They used a capacitor-

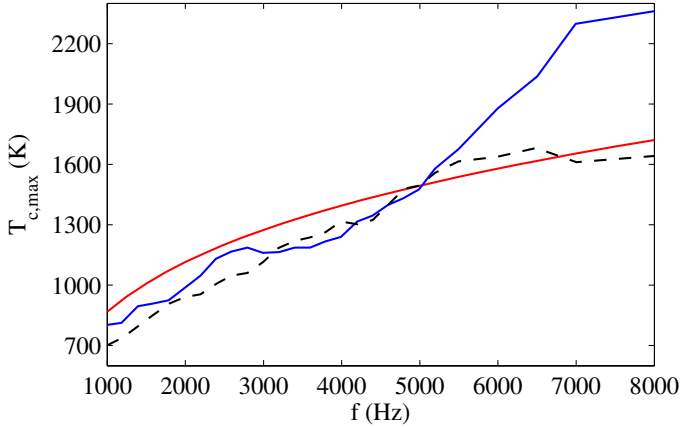


Figure 5.10: Variation of maximum cavity temperature with discharge frequency. Present model is in red, Zong et al. [88] in blue (analytical) and in black (experimental).

based supply system, varying the initial capacitor voltage and changing the electrodes distance, affecting in this way the total discharge efficiency, η_{tot} .

The basic idea of this validation process is that the peak jet front velocity, in the first operating instants, coincides with the velocity at the orifice and that the total discharge efficiency does not change for different initial capacitor voltages. Under these circumstances, an optimization process has been carried out to obtain the head loss coefficient, the effective length, the discharge efficiency for different electrodes distances.

The results, for the same values of $K = 1.35$ and $\Delta l_e = 0.23$ (with $l/d = 0.67$), are presented in Figures 5.11 and 5.12. It is interesting to note how the model is able to predict quite well both values with an error almost lower than the 10% and within the measurements uncertainty.

5.4.2 Comparison with Sary's work

To complete the validation of the present LEM code, the time trends of the basic actuation quantities have been compared to two-dimensional CFD simulations carried out by Sary et al. [85]. The geometric parameters of this actuator are: $D = 4$ mm, $H = 4$ mm and $d = 1$ mm. The amount of

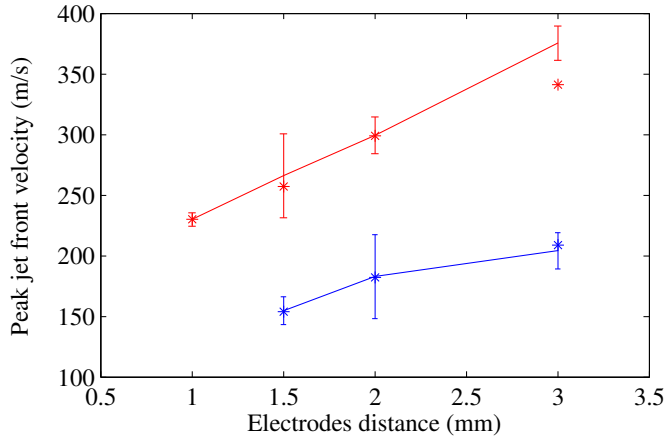


Figure 5.11: Maximum peak velocity with respect the electrodes distance for different initial capacitor voltages. Blue solid line is for $V=1000$ V, red one for $V=1500$ V, Zong et al. [98]. Star markers refer to the present model.

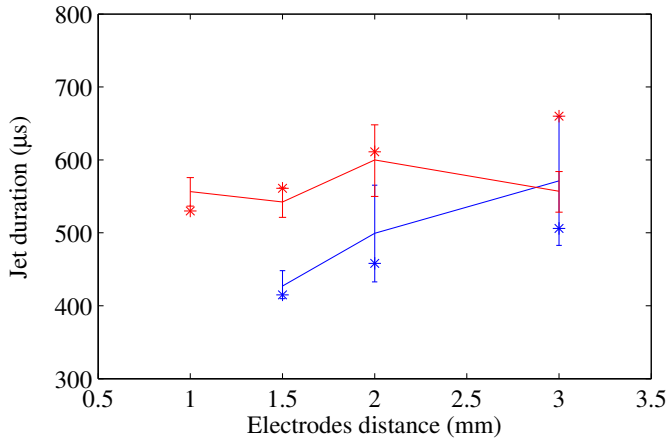


Figure 5.12: Jet discharge duration with respect the electrodes distance for different initial capacitor voltages. Blue solid line is for $V=1000$ V, red one for $V=1500$ V, Zong et al. [98]. Star markers refer to the present model.

energy is 7 mJ and the actuation frequency is 1 kHz. This last comparison is presented in Figure 5.13. Overall the agreement among the results appears very satisfactory, especially as far as the asymptotic quasi-periodic regime

is concerned.

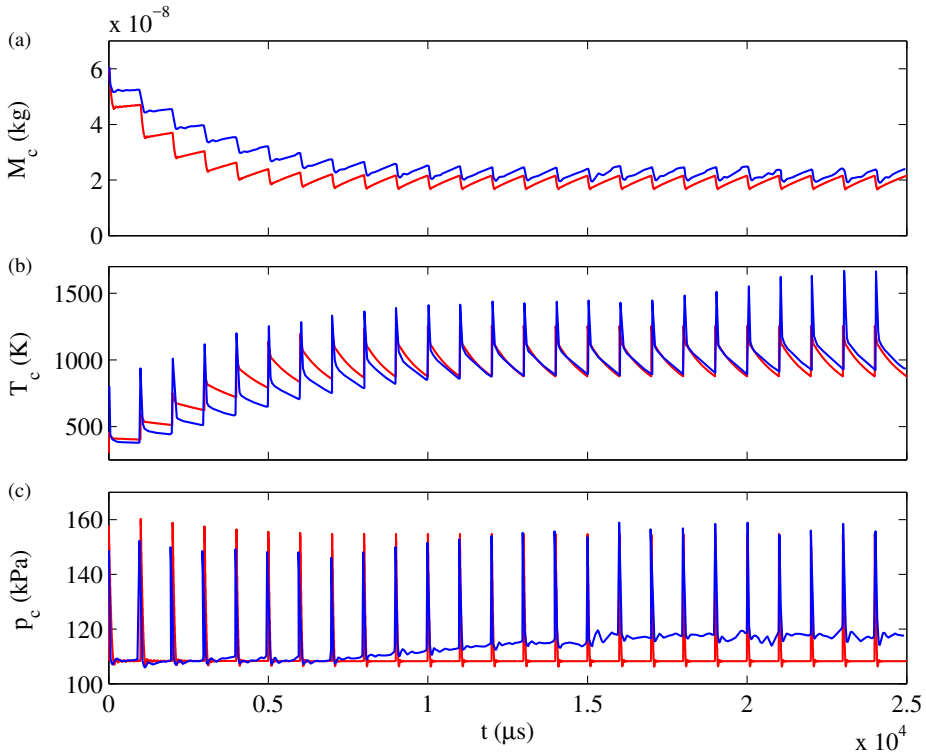


Figure 5.13: Evolution of thermodynamic parameters over the first 25 cycles. Present model is in red, Sary et al. [85] computations are in blue.

The LEM model is able to follow the mean cavity air mass trend with an error less than 10% once the periodic behavior is reached. Also the pressure evolution is well predicted, even though the Sary’s simulation predicts slightly higher values during the suction phase. The major difference lies in the peak cavity temperature which seems to be underestimated in the LEM model. The reasons of this discrepancy are at present unknown; the energy deposition process and the heat transfer mechanisms are likely the major sources of disagreement.

Chapter 6

PSJ experimental characterization

6.1 PSJ actuator

The lumped-element model, presented in Chapter 5, has been validated with experimental data obtained using a house-made PSJ actuator. The device has been completely designed and assembled in the facilities of the University of Naples. It is mainly composed of a two-part case built in MACOR, with two tungsten electrodes, and a dedicated power supply system. The coupling between the case parts (named bottom and top parts, respectively) is guaranteed by a gas-tight tread, Figure 6.1.



Figure 6.1: Picture of the main parts of the actuator. Bottom part on the left, top part on the right.

6.1.1 House-made PSJ actuator

The device has a cylindrical geometry, entirely contained in the lower part, with an orifice of 1 mm. All geometrical quantities of the actuator are reported in Table 6.1, while its technical drawings are presented in Appendix B. The electrodes, with a diameter of 1 mm and at a distance of 1.5 mm, are located in the bottom part via through holes and blocked with a non-conductive bond, making replacement extremely easy. Figure 6.2 presents a CAD reconstruction of the actuator, with a detail about the electrodes location.

Cavity diameter	6 mm
Cavity height	6 mm
Orifice diameter	1 mm
Orifice length	2 mm
Electrodes diameter	1 mm
Electrodes distance	1.5 mm

Table 6.1: Actuator geometrical variables.

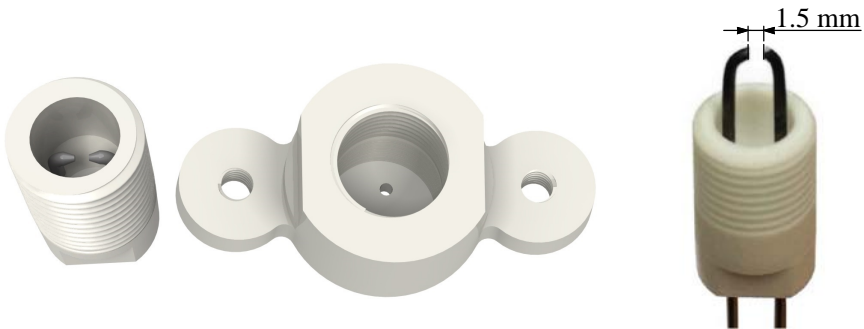


Figure 6.2: CAD reconstruction of the house-made PSJ actuator (left), detail of the electrodes location (right).

6.1.2 Power supply system

The power supply system makes use of a trigger transformer, in the so-called *pseudo-series mode* (Popkin [107]), to trigger the spark discharge. The system has been developed in collaboration with Heraeus spa, Noblelight Division, and it represents a compact system which allows many adjustments from a single device. The entire system is mainly constituted of a high-voltage *trigger device* and an external supply system (*sustain device*), which provides electrical power to the first one, as depicted in Figure 6.3.

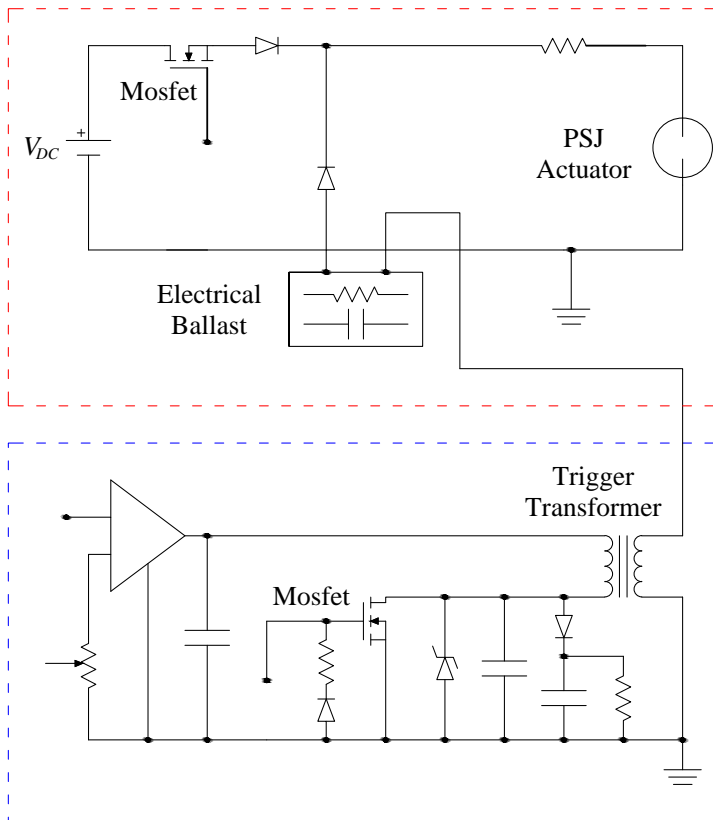


Figure 6.3: The power supply system: the red box contains the sustain circuit, while the blue the trigger one.

To explain its working principles, it is convenient to introduce two sub-

circuits, Zong et al. [89]:

- The *trigger circuit* is mainly composed of an internal DC power supply, a flyback circuit and a trigger transformer. The DC power supply provides a 24 V adjustable voltage, which, through the flyback converter, is led up to values of $150 \div 400$ V. When switched on, the capacitors inside the circuit begin to discharge across the trigger transformer (with a ratio of 1 : 30) that quickly (in a few μs) raises the voltage between the electrodes. If the peak trigger voltage is higher than the air breakdown voltage between the electrodes a trigger spark is formed, Fridman et al. [108].
- The *sustain circuit* is represented by an external DC power supply (TDK-Lambda Gen-600), whose discharge time is controlled by a Mosfet transistor, a mixer and an electrical ballast. The power supply can provide a voltage up to 600 V, which by itself it is not able to produce a spark between the electrodes. The mixer has the role to combine the electrical outputs of the trigger and the sustain circuits; while the electrical ballast provides a protection to the system.

Figures 6.4 represent a front view of the power supply system, where the top box contains the trigger circuit and the bottom one the sustain circuit. It is possible to observe all the commands available together with several LED display. Moreover, Figures 6.5 shows the internal part of the trigger circuit. It is interesting to note the presence of the trigger transform in the top central part and the mixer in the right part, closed in a metal cage.

6.1.3 Operating Cycle

The operating cycle starts with a high-voltage trigger pulse to produce a channel between the electrodes, that reduces the breakdown voltage below the electrodes voltage provided by the sustain circuit; so, when the Mosfet is turned on an electrical arc is formed inside the cavity. The purpose of the trigger spark is to momentarily reduce the local breakdown voltage between the anode and the cathode and to define the actuation frequency; whereas, the amount of energy provided to the fluid in each cycle can be controlled



Figure 6.4: Front view of the power supply system. The top box contains the trigger circuit, the bottom one includes the sustain circuit.

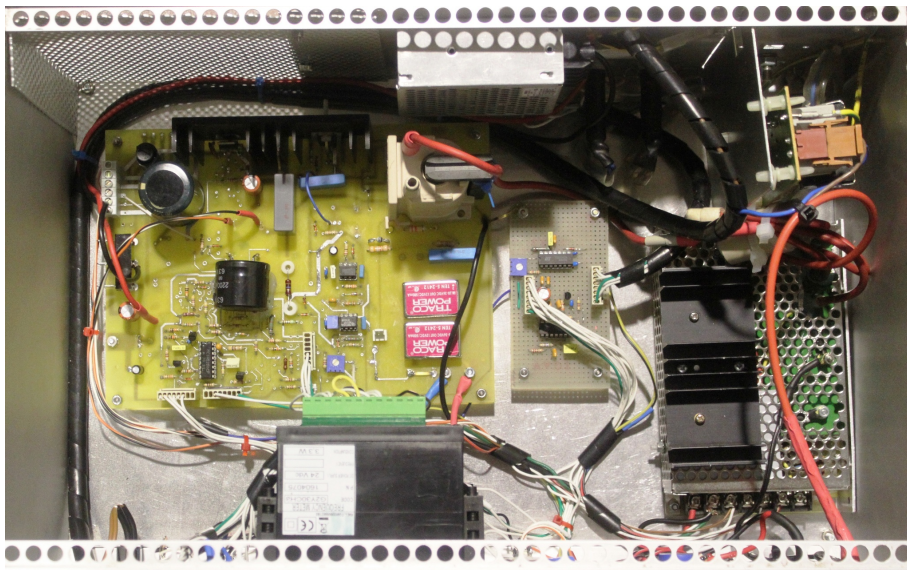


Figure 6.5: The power supply system: the red box contains the sustain circuit, while the blue the trigger one.

with the external power supply, by varying the sustain voltage, or through the Mosfet transistor, by changing the duration of the discharge.

Figure 6.6 represents an example of the electrical signals provided by the system. In this case, a discharge frequency, $f = 1000$ has been chosen Hz, with a duty cycle of 40%, corresponding to a discharge time equal to $T_d = 400 \mu\text{s}$. The duration of the trigger signal is always equal to $5 \mu\text{s}$, defining the lower limit of the discharge time. It is important to remember that the exit signal is a mixture of the previous ones with values, to the net of the electrical losses (η_a), equal to the sum of both signals.

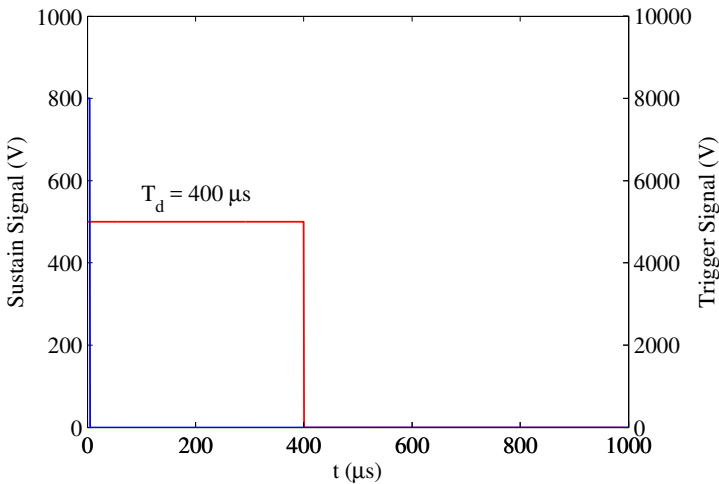


Figure 6.6: PSJ signals. Blue line represents the trigger signal, red line the sustain one.

The electrical supply system allows the variation of the trigger voltage in a range from 1.5 to 12 kV and to choose the actuation frequency from 1 up to 1000 Hz. It is also possible to select the Mosfet operating duty cycle (namely the sustain discharge duration) from 0 to 90%, divided in three operating intervals (short, mid and long period). All the settings can be defined directly from the front panel of the trigger device or by external inputs. Furthermore, the device is provided with two internal oscilloscopes to verify the signals shapes; the applied voltage and the discharge current can be measured with a high voltage and a current probe respectively. Based

on these values, the discharge energy per pulse is computed as:

$$E_a = \int_0^{T_d} V_{arc}(t) \cdot i(t) dt \quad (6.1)$$

where $V_{arc}(t)$ and $i(t)$ are the voltage and the instantaneous current of the discharge respectively.

During the experimental campaign, the PSJ actuator has been mounted on a dedicated structure, equipped with two cross tables to align all the elements. Figure 6.7 presents a very interesting comparison of the device operating electrical phases. The first row reports the actuator bottom part only; the second one, instead, shows the whole device. Starting from the left, it is possible to examine the device in the turned off condition, than during the trigger mode phase and, finally, during the operating regime. Note that without the top part both electrical arcs are clearly visible, with the sustain one being more intense. In some cases it is possible to note a bifurcation of the electrical arc discharges during its working mode. On the other hand, putting the cup on the device, the high-voltage trigger discharges are barely appreciable and, due to their short duration, the energy supplied to the fluid is negligible; on the other hand, in operating conditions the energy discharges are clearly visible leading to the PSJ formation.

6.2 Experimental measurements

6.2.1 Pitot tube

The PSJ total pressure has been measured with a house-made Pitot tube placed 1 diameter downstream of the nozzle exit, Figure 6.8, with a 0.6 mm external and a 0.4 mm internal diameter, connected with a Mouser sensor pressure transducer (range: ± 5 in H_2O , accuracy: 0.25 %), whose output signal has been acquired with a data-acquisition system (USB Instruments DS1M12 or “Stingray”). The time-averaged total pressure is computed by averaging the signal acquired for 10 s.

Due to its very small size, the Pitot tube measurements might be affected by viscous effects, invalidating the Bernoulli equation. The deviation of stagnation pressure from Bernoulli pressure was first experimentally

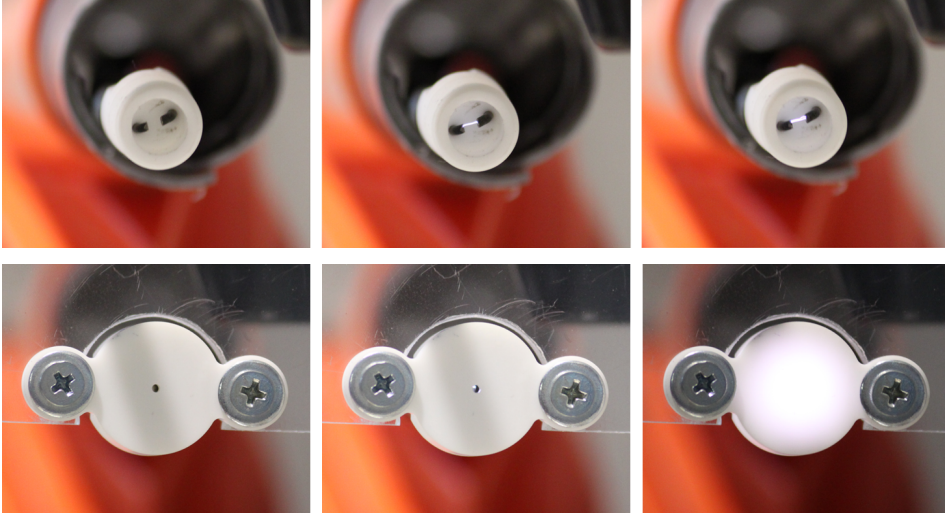


Figure 6.7: Actuator operating electrical phases. Device bottom part only (top row) and whole device (bottom row).

demonstrated by Barker [109] (known as Barker effect) and theoretically and experimentally estimated by Homann [110] for a cylinder and a sphere geometry (Homann correction). Recently, Boetcher et al. [111] resumed the problem providing a specific threshold for which the Bernoulli equation fails. For a blunt faced tube this threshold is defined by the Reynolds number based on the external tube diameter:

$$Re_{threshold} \cong 65 \quad (6.2)$$

For the present measurements the Reynolds number is $\cong 400$, definitively higher than the threshold defined by Equation 6.2.

In this experimental campaign the actuator has been tested for relatively small energy depositions, hence the classic Bernoulli equation at the orifice exit can be assumed to be valid. The measure of the actuator external temperature with a FLIR SC6000 Series Infrared Camera has allowed a good estimation of the actual air density, and eventually of the jet velocity, with a uncertainty estimation of about 6%, computed with the standard procedures of literature.

Typical jet velocity profiles in the radial direction are reported in Fig-



Figure 6.8: PSJ actuator with the Pitot probe.

ure 6.9; the measurements have been acquired with a fixed frequency of 500 Hz and a duty cycle of 10%. As for continuous jets or piezo-driven synthetic jets, the plasma jet exhibits bell-shaped velocity profiles; note also the spreading effect of the jet already visible at the very short axial distance here considered. In the range of deposited energy values of the present test conditions, the peak velocity seems to increase almost linearly. For these cases the temperatures measured with the infrared camera are in the range of $85\text{--}165^\circ\text{C}$, a typical image acquired with the infrared camera is presented in Figure 6.10. In the case of MACOR (ceramic material) the emissivity coefficient has been considered equal to 0.8.

6.2.2 Hot-wire Anemometer

A Dantec's MiniCTA hot-wire anemometer has been used to complete the experimental campaign. This anemometer is an analogue instrument designed for measuring velocity in gases; it works on the basis of convective heat transfer from a heated sensor to the surrounding fluid, relating the heat transfer to the fluid velocity, [112]. The system makes use of a miniature wire probe, straight (55P11), whose characteristics are reported in Table

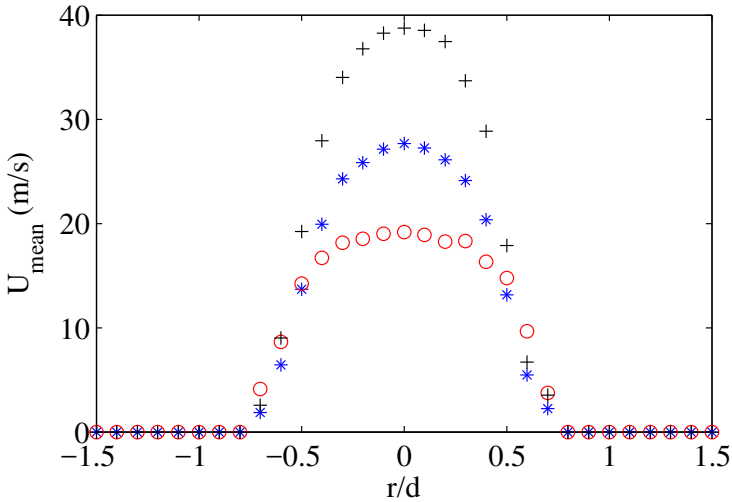


Figure 6.9: Velocity profiles in the radial direction for different energy discharges. Blue markers are the results for $E_d = 1.2$ mJ, red ones for $E_d = 2.1$ mJ and black ones for $E_d = 3.4$ mJ.

6.2.

A Hot-wire anemometer requires a calibration process to establish a relation between the CTA output and the flow velocity by exposing the probe to a set of known velocities, U and then recording the voltage, E . A curve fit through the points (E, U) represents the transfer function to be used when converting data records from voltages into velocities. In this case, the calibration process has been carried out measuring the downstream velocity of a converging nozzle with a Pitot probe, creating a transfer function in the form of a 4th polynomial in E , Equation 6.3. Figure 6.11 reports the calibration curve and the Table 6.3 contains the coefficients of the (E, U) relation.

$$U = p_1 E^4 + p_2 E^3 + p_3 E^2 + p_4 E + p_5 \quad (6.3)$$

Once the calibration curve is available, it is possible to start the experimental measurements, taking special attention to the jet temperature. In fact, when the measurements are carried out in a flow field with a different

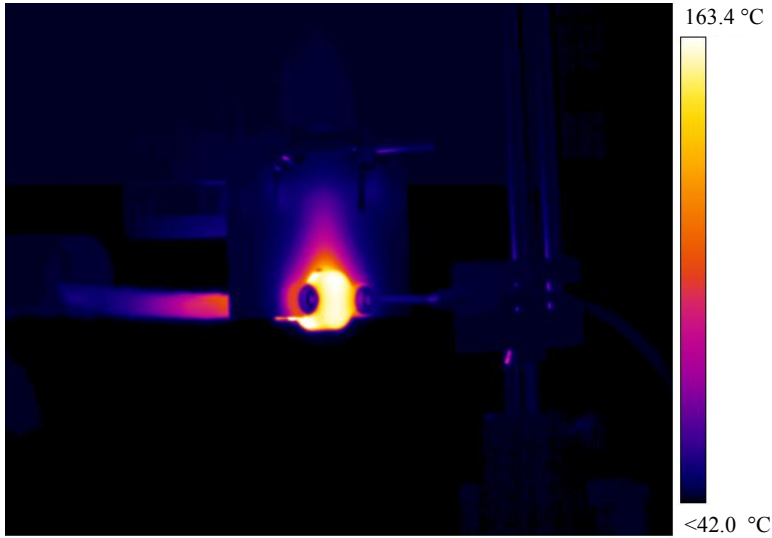


Figure 6.10: Temperature field acquired with the Flir SC6000 infrared camera ($f = 500$ Hz, duty cycle of 5 %).

temperature than that of the calibration process, corrections are required. In this case, the acquired voltage E_a has been corrected by means of the known values for the wire temperature, $T_w = 300\text{ }^\circ\text{C}$, the calibration temperature, $T_0 = 21\text{ }^\circ\text{C}$ and the temperature, T_a during acquisitions, 6.4.

$$E_{corr} = \left(\frac{T_w - T_0}{T_w - T_a} \right)^{0.5} E_a \quad (6.4)$$

The fluid temperature close to the orifice has been estimated through measurements of the infrared cameras, while the mean temperature profile along the downstream direction throughout a Chromel-Alumel thermocouple (type K). Note that, as done for the Pitot measurements, also in this case the device has been tested for relatively small energy deposition, for not reaching temperatures higher than that of the probe.

The Hot-wire probe has been placed at a distance of 1 mm, Figure 6.12 acquiring the signal with a frequency of 10 KHz. The measurements are reported in the next section.

Wire material	Tungsten
Wire diameter	5 μm
Wire length	1.25 mm
Sensor resistance	3.30 Ω
Sensor lead resistance	0.50 Ω
Cable resistance	0.60 Ω
Wire temperature	300 K
Electrodes distance	3.30 Ω
Operating resistance	6.39 Ω
Total resistance	7.49 Ω
Overheat ratio	0.94 Ω

Table 6.2: Hot-wire probe (55P11) characteristics.

p_1	2.812e-09
p_2	-7.993e-06
p_3	0.008547
p_4	-4.015
p_5	694.9

Table 6.3: Coefficients of the (E, U) calibration curve.

6.2.3 Tuning of the lumped model

Once the total pressure and velocity measurements have been acquired, it has been possible to tune the lumped model with the experimental results: the basic idea was to carry out a best-fit between the experimental data and the LEM computations of the time-averaged total pressure and velocity, assuming the total efficiency of the device as the fitting parameter. For LEM data, the time-averaged total pressure and velocity have been computed considering the ejection phase only, Zong et al. [88], and employing the classical gasdynamics relationship to relate the flow conditions at the exit orifice to the ones at the measurement axial location. In the end, the best fitting procedure has yielded the value of $\eta_{tot} = 0.45$.

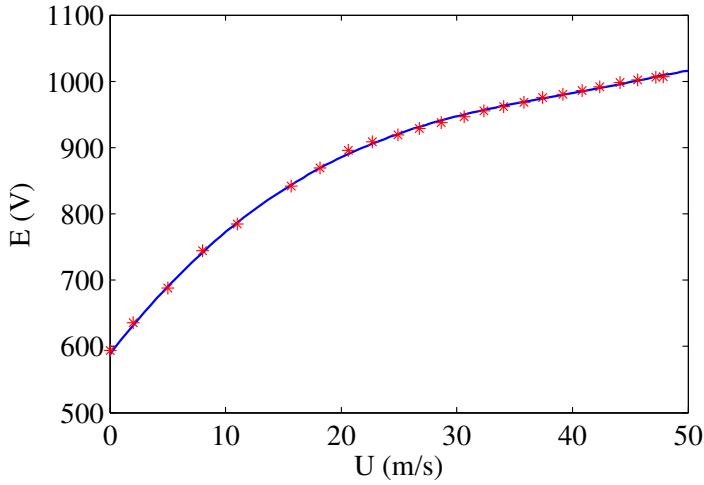


Figure 6.11: Calibration Curve, (E, U) .

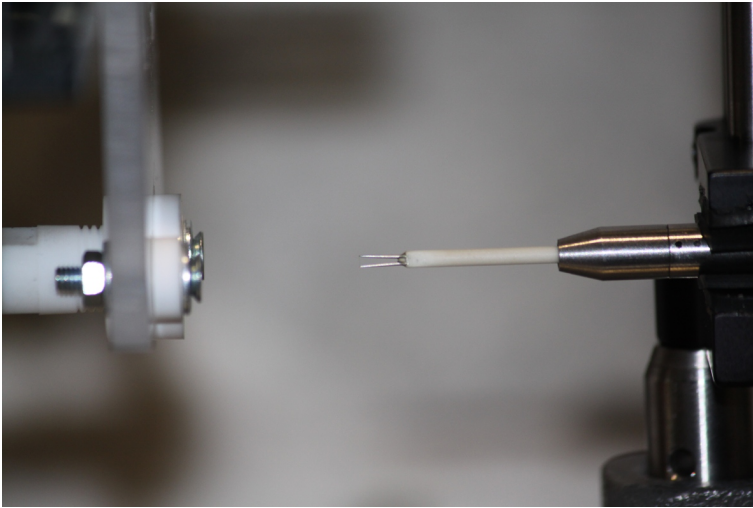


Figure 6.12: PSJ actuator with the Hot-wire anemometer probe.

Figure 6.13 presents a comparison between the experimental and numerical jet mean velocity, obtained using the total pressure data. The LEM model seems to be able to predict, with a good accuracy, the jet mean velocity as a function of actuation frequency and discharged energy. In addition, it is worth noting that, except for very low discharged energy values, the

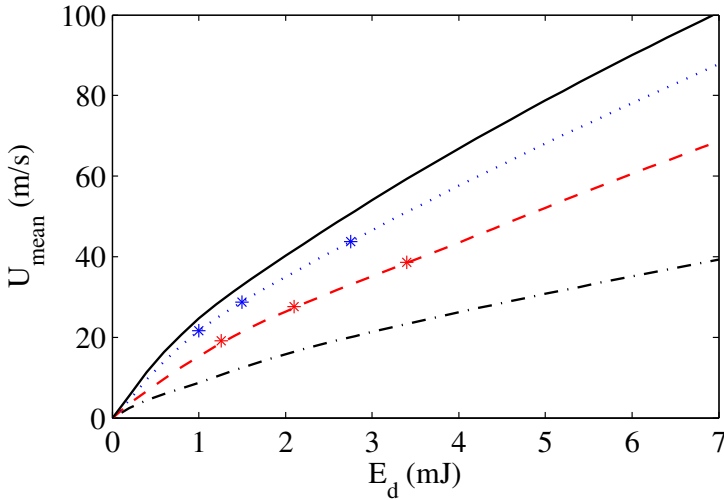


Figure 6.13: Variation of the mean jet velocity (Pitot tube measurements) with energy discharges for different actuation frequency. Black solid line refers to $f = 1000$ Hz, blue dotted line to $f = 750$ Hz, red dashed line $f = 500$ Hz, black dash-dot line to $f = 250$ Hz. Star markers represent experimental data.

variation with the energy is almost linear; it is also evident that increasing in actuation frequency produces increasingly higher jet velocities.

At the same way, it has been possible to compute the a comparison between the experimental and numerical jet mean velocity, obtained using the Hot-wire velocity measurements, Figure 6.14. Data have been acquired for different duty cycle values, namely 5 %, 10 %, and 15 %, for an actuation frequency of $f = 500$ Hz. It is very interesting to observe that increasing the duty cycle, namely the energy discharge time, produces increasingly higher jet velocities, because the amount of energy supplied to the fluid for each discharge process is higher.

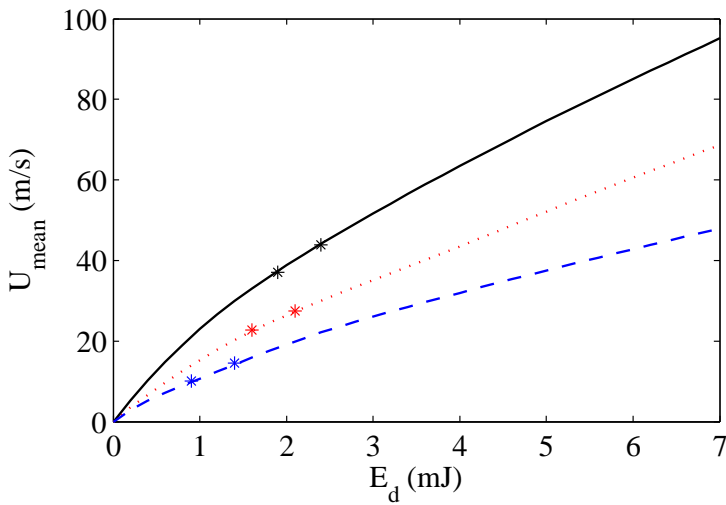


Figure 6.14: Variation of the mean jet velocity (Hot-wire measurements) with energy discharges for different duty cycle (DC) values. Black solid line refers to $DC = 5\%$, red dotted line to $DC = 10\%$ and blue dashed line to $DC = 15\%$. Star markers represent experimental data.

List of Symbols - Part II

Roman symbols

A	cross-sectional area, m^2
D	cavity diameter, m
d	orifice diameter, m
H	cavity height, m
h	specific enthalpy, $J \cdot kg^{-1}$
h_{conv}	convective heat transfer coefficient, $W/(m^2 \cdot K)$
E_a	arc energy discharge, J
E_{dc}	external power supply energy, J
E_f	effective energy supplied to the fluid, J
f	actuation frequency, Hz
f_H	Helmholtz frequency, Hz
i	instantaneous current, A
K	head loss coefficient
l	length of the nozzle, m
l_e	effective nozzle length, m
M	Mach number
p	fluid pressure, Pa
\dot{Q}	heat power, W
R	air gas constant, $J/(kg \cdot K)$
R_0	air gas constant at standard conditions, $J/(kg \cdot K)$
S	exchange surface, m^2
T	fluid temperature, K
U	jet velocity exit, m/s
U_{max}	maximum peak velocity, m/s
u	specific internal energy, $J \cdot kg^{-1}$

V	volume, m^3
V_{arc}	arc discharge voltage, V
V_{dc}	sustain voltage, V
Z	compressibility factor

Greek symbols

ε	emissivity coefficient
γ	specific heats ratio
η_a	arc discharge efficiency
η_f	heating efficiency
η_{tot}	total efficiency
λ	thermal conductivity of the air, $W/(m \cdot K)$
ρ	fluid density, kg/m^3
σ	Stefan-Boltzmann constant, $W/(m^2 \cdot K^4)$

Sub- and Superscripts

a	ambient conditions
c	variables inside the cavity
$conv$	convective heat transfer
e	variables at the nozzle exit
H	Helmholtz
i	initial conditions
rad	radiative heat transfer
w	variables at the wall

Acronyms

CFD	Computational Fluid Dynamics
LEM	Lumped Element Model
PSJ	Plasma Synthetic Jet

Chapter 7

Conclusions and future work

In this work innovative lumped element models, able to predict the behavior of piezo-driven synthetic jet and plasma synthetic jet actuators, have been presented. The design, the manufacturing and the characterization procedures of several prototypes, used to validate the LEMs, have been deeply investigated. Finally, as an additional task, various applications both in automotive and aerospace fields have been taken into account.

Piezo-driven synthetic jet actuators

As regards the piezo-driven synthetic jet actuators, a comprehensive review, covering the development and the evolution of LEM modeling for the design and the performance evaluation of synthetic jet actuators, has been presented. This provides an overview on the topic and it may be used as a practical guide for the design and the manufacturing of devices with desired specifications; it analyzes the actuator performance by varying typical geometric parameters and facing the different nature (and the intrinsic links) of existing literature LEMs models. The innovative contribution can be found not only in the referenced co-authored papers but also on the new formulations and further insights that have been presented.

In particular, a deeply comparison of the two basic LEM approaches, the one fully based on the fluid dynamics equations, and the other one obtained within the so-called equivalent electric circuit framework, has been presented, identifying all relations between their quantities. A complete dimensionless analysis has been reported, leading to the nondimensional forms

of the governing equations which are related to the behavior of a two coupled mechanical and acoustic oscillators, the diaphragm and the Helmholtz one. Overall, the dimensionless analysis along with the analytical formulas describing the stationary-periodic jet response, allowed the recognition of the set of dimensionless parameters governing the operation of the device. Moreover, an investigation of the major device performances (basically the frequency response in terms of jet velocity), as functions of the main parameters that influence the oscillators coupling, the supply voltage and the effective orifice length, has been carried out. Finally, a study of efficiency of SJ actuators, based on a physical model directly related to the energy equations of the two coupled oscillators, has been achieved. For all the cases here considered, for the aim of providing useful and practical design and manufacturing information, specific attention has been paid to emphasize the role played by the nondimensional governing parameters, in particular the degree of coupling of the two oscillators.

A very interesting application of the piezo-driven SJ technology, which has been investigated during this work, regards the manipulation of a continuous water spray. This analysis can have considerable outcomes in the automotive sector. More in details, PIV results have shown that the synthetic jet interacts with the spray locally, energizing the region downstream of the impact and producing higher velocity droplets. This effect tends to reduce increasing the injection pressure, in agreement with the estimated momentum coefficients, due to a high droplets momentum values, which makes their motion alteration more difficult. Moving downward the injector, the air flow impacts against the spray in a region closer to the nozzle. The higher water momentum flux induces a reduction of the air flow-water spray interaction, both in terms of interaction region size and velocity difference. The study has also taken advantage of the analysis of the vorticity pattern introduced into the spray field by the typical vortex structures produced by the synthetic jet, as this issues from the actuator orifice.

Plasma synthetic jet actuators

Another very important goal of this work regards the development of a second LEM mathematical model for plasma synthetic jet actuator. This latter, fully based on gasdynamics governing equations, is able to predict

the time variation of the thermodynamic variables inside the cavity, as well as the air jet velocity at the orifice. It includes both radiative and convective heat transfer detailed mechanisms at the walls of the control surfaces, and can predict both choked and unchoked orifice flow regimes. CFD axisymmetric numerical simulations, carried out with OpenFOAM code, has allowed a preliminary calibration of the lumped model.

An interesting theoretical new result lies in the finding that the device behaves like a Helmholtz resonator, that justifies the presence of high frequency oscillations observed in the time interval between two subsequent discharge pulses. The Helmholtz natural frequency evaluated by the lumped-element modeling, which is a function of the operating conditions because it depends on thermodynamics variables, agrees very closely with analytical predictions. This constitutes a further theoretical validation of the present model.

During a parallel experimental investigation, a home-designed and manufactured PSJ actuator, composed of two parts in Macor and two electrodes with a distance of 1.5 mm , has been experimentally tested for different frequencies and energy discharges. A specific house-made Pitot tube and a Hot-wire anemometer have allowed to obtain the velocity profiles along the jet radial direction and to perform a tuning of the lumped model with experimental data, where the total device efficiency has been assumed as a fitting parameter. The best fitting value is $\eta_{tot} = 0.45$.

Future work

An interesting extension of the model for piezo-driven synthetic jet actuators is related to a two-orifices device with a single cavity. A multi-orifice configuration is generally used for heat transfer problems, to improve the cooling capacity of the actuator, or for flow control applications in which size problems are relevant. In this case the Helmholtz frequency should scale as $\approx \sqrt{2}$, where 2 is related to the number of the orifices. A physical model, able to predict the frequency response of a such actuator, is very useful for these kind of applications, helping the designer to predict the dynamic response of the actuator in relatively quick way and with reasonable fidelity and accuracy.

As regards the manipulation of a continuous water spray with a SJ device, results have shown that the synthetic jet interacts with the spray locally, energizing the region downstream of the impact and producing higher velocity droplets. A new design of the device and the experimental mock-up is required. In fact, increasing the momentum coefficient, namely the velocity produced by the SJ actuator, together with an improvement of the overall set-up, would affect globally the spray behavior, producing a spray vectoring and changing the size and distribution of droplets.

Finally, regarding the PSJ devices, a remarkable amount of work is now available. The analysis of this device has just begun. A first step to improve the lumped model is related to the determination of some parameters (head loss coefficient, k , and the effective length of the orifice, l_e) directly from the experimental measurements. This requires, however, instantaneous temperature measurements to correct the Hot-wire data. Furthermore, a deep analysis of the actuator performances can be started changing the geometrical and electrical quantities, by making a comparison between numerical and experimental data. Further investigations of the energy deposition process, shedding light on the different aspects of this stage, appear mandatory to characterize the efficiency of these devices. Finally, an application of this technology is related to the control of a flow over a wing surface, studying the enhancement of the corresponding aerodynamic forces.

Appendices

Appendix A

PSJ governing equations

The model is constituted by three ordinary differential equations (Equations (5.2), (5.3), (5.5)), and a non-linear algebraic relation (Equation (5.6)), that should be particularized for the exit conditions (Equation (5.8) or Equation (5.9)).

Summary of choked equations

In the case of choked flow Equations (5.2), (5.4), (5.5) and (5.6) are combined with Equation (5.8), to recast the system of equations in the following convenient form:

$$\frac{d\rho_c}{dt} = -\frac{A_e}{V_c} U \rho_c \left[\frac{c_p(T_c)}{c_p(T_e)} \frac{2}{\gamma(T_e) + 1} \right]^{\frac{1}{\bar{\gamma}-1}} \quad (\text{A.1})$$

$$\frac{\partial U}{\partial t} = \frac{1}{l_e} \left(c_p(T_c)T_c - c_p(T_e)T_e - K \frac{|U|U}{2} \right) \quad (\text{A.2})$$

$$\begin{aligned} \frac{dT_c}{dt} = & \frac{1}{\rho_c c_v(T_c) V_c} \left[\frac{E_f}{T_d} - \dot{Q} - c_v(T_c)T_c \frac{d\rho_c}{dt} V_c - \rho_c \left(\frac{c_p(T_c)}{c_p(T_e)} \frac{2}{\gamma(T_e) + 1} \right)^{\frac{1}{\bar{\gamma}-1}} \right. \\ & \left. A_e \left(c_p(T_e)T_e + \frac{U^2}{2} \right) U \right] = 0 \end{aligned} \quad (\text{A.3})$$

$$T_e = T_c \frac{c_p(T_c)}{c_p(T_e)} \left[\frac{2}{\gamma(T_e) + 1} \right] \quad (\text{A.4})$$

Summary of unchoked equations

When the energy discharge is not powerful enough to cause an increase of cavity pressure greater than its critical value, the flow issues through the orifice in unchoked regime. In this condition the system of equations is conveniently handled in the following way:

$$\frac{d\rho_c}{dt} = -\frac{A_e}{V_c} U \rho_c^{\frac{\bar{\gamma}-1}{\bar{\gamma}}} \left[\frac{p_a}{T_c R(T_e)} \right]^{\frac{1}{\bar{\gamma}}} \quad (\text{A.5})$$

$$\frac{\partial U}{\partial t} = \frac{1}{l_e} \left(c_p(T_c)T_c - c_p(T_e)T_e - K \frac{|U|U}{2} \right) \quad (\text{A.6})$$

$$\begin{aligned} \frac{dT_c}{dt} = & \frac{1}{\rho_c c_v(T_c) V_c} \left[\frac{E_f}{T_d} - \dot{Q} - c_v(T_c) T_c \frac{d\rho_c}{dt} V_c - A_e U \cdot \right. \\ & \left. \left(c_p(T_e)T_e + \frac{U^2}{2} \right) \rho_c^{\frac{\bar{\gamma}-1}{\bar{\gamma}}} \left(\frac{p_a}{T_c R(T_e)} \right)^{\frac{1}{\bar{\gamma}}} \right] = 0 \end{aligned} \quad (\text{A.7})$$

$$T_e = T_c^{1/\bar{\gamma}} \cdot \left[\frac{p_a}{\rho_c R(T_e)} \right]^{\frac{\bar{\gamma}-1}{\bar{\gamma}}} \quad (\text{A.8})$$

Appendix B

Technical drawings

This appendix is dedicated to the technical drawings of the PSJ actuator.

The scale is 1 : 1 and all the measurements are in millimeters. For both parts (bottom and top parts) are reported:

- isometric view;
- front view;
- top view;
- A-A and B-B sections.

Isometric View

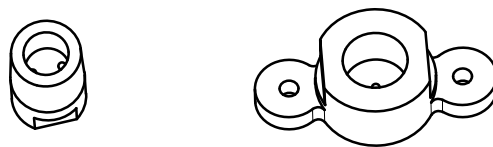


Figure B.1: Technical drawing: isometric view. Bottom part (left), top part (right).

Front View

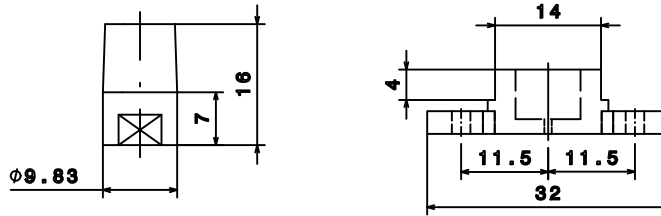


Figure B.2: Technical drawing: front view. Bottom part (left), top part (right).

Top View

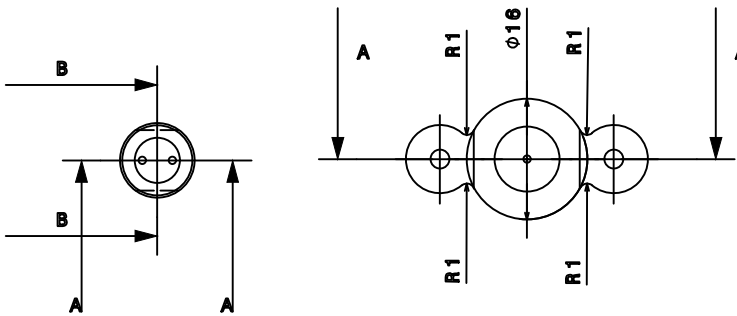


Figure B.3: Technical drawing: top view. Bottom part (left), top part (right).

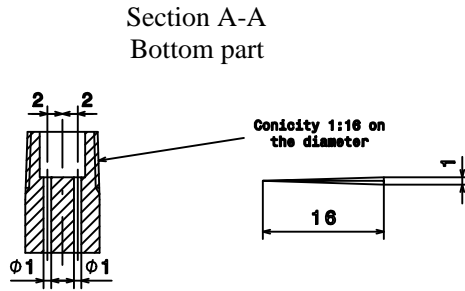


Figure B.4: Technical drawing: section A-A of the bottom part.

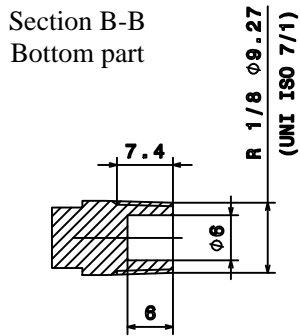


Figure B.5: Technical drawing: section B-B of the bottom part.

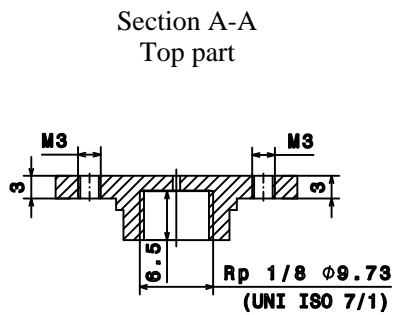


Figure B.6: Technical drawing: section A-A of the top part.

References

- [1] E. Moreau. Airflow control by non-thermal plasma actuators. *Journal of Physics D: Applied Physics*, 40(3):605–636, 2007.
- [2] M. Gad-el Hak. *Flow Control: Passive, Active, and Reactive Flow Management*. Cambridge University Press; 1 edition, 2000.
- [3] J.C. Lin. Review of research on low-profile vortex generators to control boundary-layer separation. *Progress in Aerospace Sciences*, 38(4-5):389–420, 2002.
- [4] R. García-Mayoral and J. Jiménez. Drag reduction by riblets. *Philosophical Transactions of the Royal Society A: Mathematical, Physical and Engineering Sciences*, 369(1940):1412–1427, 2011.
- [5] L.N. Cattafesta III and Sheplak M. Actuators for active flow control. *Annu. Rev. Fluid Mech.*, 43:247–272, 2010.
- [6] D.G. MacMynowski and Williams D.R. *Flow Control Terminology*, volume 683 of *Progress in Astronautics and Aeronautics*, chapter 3, pages 59–71. AIAA, 2011.
- [7] R. Dadfar, O. Semeraro, A. Hanifi, and D.S. Henningson. Output feedback control of blasius flow with leading edge using plasma actuator. *AIAA Journal*, 51(9):2192–2207, 2013.
- [8] A. Glezer and M. Amitay. Synthetic jets. *Annu. Rev. Fluid Mech.*, 34:503–529, 2002.

- [9] J.C. Magill and K.R. McManus. Exploring the feasibility of pulsed jet separation control for aircraft configurations. *Journal of Aircraft*, 38(1):48–56, 2001.
- [10] P. Joseph, X. Amandolèse, and J.-L. Aider. Drag reduction on the 25° slant angle ahmed reference body using pulsed jets. *Experiments in Fluids*, 52(5):1169–1185, 2012.
- [11] R. Becker, R. King, R. Petz, and W. Nitsche. Adaptive closed-loop separation control on a high-lift configuration using extremum seeking. *AIAA Journal*, 45(6):1382–1392, 2007.
- [12] J.J. Choi, A.M. Annaswamy, H. Lou, and F.S. Alvi. Active control of supersonic impingement tones using steady and pulsed microjets. *Exp Fluids*, 41(6):841–855, 2006.
- [13] G. Raman and K. Srinivasan. The powered resonance tube: From hartmann’s discovery to current active flow control applications. *Progress in Aerospace Sciences*, 45(4-5):97–123, 2009.
- [14] C.G. Matalanis, B.-Y. Min, P.O. Bowles, S. Jee, B.E. Wake, T.M. Crittenden, G. Woo, and A. Glezer. Combustion-powered actuation for dynamic-stall suppression: High-mach simulations and low-mach experiments. *AIAA Journal*, 53(8):2151–2163, 2015.
- [15] S. Raghu. Fluidic oscillators for flow control. *Experiments in Fluids*, 54(2), 2013.
- [16] Schubauer G.B. and Skramstad H.K. *Laminar-boundary-layer oscillations and transition on a flat plate*, 1948.
- [17] E.P. DeMauro, H. Dell’Orso, S. Zaremski, C.M. Leong, and M. Amitay. Control of laminar separation bubble on naca 0009 airfoil using electroactive polymers. *AIAA Journal*, 53(8):2270–2279, 2015.
- [18] E. Moreau, L. Léger, and G. Touchard. Effect of a dc surface-corona discharge on a flat plate boundary layer for air flow velocity up to 25 m/s. *Journal of Electrostatics*, 64(3-4):215–225, 2006.

-
- [19] F. Massines, N. Gherardi, N. Naudé, and P. Ségur. Recent advances in the understanding of homogeneous dielectric barrier discharges. *EPJ Applied Physics*, 47(2):22805p1–22805p10, 2009.
- [20] J. Kriegseis, B. Simon, and S. Grundmann. Towards in-flight applications? a review on dielectric barrier discharge-based boundary-layer control. *Applied Mechanics Reviews*, 68(2), 2016.
- [21] E. Moreau, R. Sosa, and G. Artana. Electric wind produced by surface plasma actuators: A new dielectric barrier discharge based on a three-electrode geometry. *Journal of Physics D: Applied Physics*, 41(11), 2008.
- [22] K. Yugulis, S. Hansford, J.W. Gregory, and M. Samimy. Control of high subsonic cavity flow using plasma actuators. *AIAA Journal*, 52(7):1542–1554, 2014.
- [23] K. R. Grossman, B. Z. Cybyk, and D. M. VanWie. Sparkjet actuators for flow control. In *41st Aerospace Sciences Meeting and Exhibit. Reno. Nevada*, pages 1–9, 2003.
- [24] B. Z. Cybyk, J. T. Wilkerson, and K. R. Grossman. Performance characteristics of the sparkjet flow control actuator. In *2nd AIAA Flow Control Conference. Portland. Oregon*, pages 1–9, 2004.
- [25] B.L. Smith and A. Glezer. Jet vectoring using synthetic jets. *J. Fluid Mech.*, 458:1–34, 2002.
- [26] A. Glezer. Some aspects of aerodynamic flow control using synthetic-jet actuation. *Phil. Trans. R. Soc. A*, 369:1476–1494, 2010.
- [27] T. Van Buren, C.M. Leong, and E. Whalen. Impact of orifice orientation on a finite-span synthetic jet interaction with a crossflow. *Physics of Fluids*, 28:(037106) 1–20, 2016.
- [28] H. Wang and S. Menon. Fuel-air mixing enhancement by synthetic microjets. *AIAA Journal*, 39:2308–2319, 2010.

- [29] D.A. Tamburello and M. Amitay. Active manipulation of a particle-laden jet. *International Journal of Multiphase Flow*, 34(9):829–851, 2008.
- [30] A. Pavlova and M. Amitay. Electronic cooling using synthetic jet impingement. *Physics of Fluids*, 128:897–907, 2006.
- [31] Chaudhari M., B. Puranik, and A. Agrawal. Heat transfer characteristics of synthetic jet impingement cooling. *Int. J. Heat and Mass Transfer*, 53:1057–1069, 2010.
- [32] A.A. Pavlova, K. Otani, and M. Amitay. Active control of sprays using a single synthetic jet actuator. *Int J. Heat and Fluid Flow*, 29:131–148, 2007.
- [33] L. Marchitto, G. Valentino, M. Chiatto, and L. de Luca. Experimental characterization of spray water controlled by a synthetic jet. In *Proceedings of 18th International Symposium on the Application of Laser and Imaging Techniques to Fluid Mechanics, 4-7 July, Lisbon, Portugal*, pages 1–13, 2016.
- [34] T.J. Finley and K. Mohseni. Micro pulsatile jets for thrust optimization. In *IMECE2004, 2004 ASME International Mechanical Engineering Congress and Exposition November 13-20, 2004, Anaheim, California USA*, pages 1–9, 2004.
- [35] B.A. Parviz, K. Najafi, M.O. Muller, L.P. Bernal, and P.D. Washabaugh. Electrostatically driven synthetic microjet arrays as a propulsion method for micro flight. part i: principles of operation, modeling, and simulation. *Microsystem Technologies*, 11:1214–1222, 2005.
- [36] K. Otani, J. Moore, W Gressick, and M Amitay. Active yaw control of a ducted fan-based mav using synthetic jets. *Int. Journal of Flow Control*, 1:29–42, 2009.
- [37] C.S. Greco, A. Ianiro, T. Astarita, and G. Cardone. On the near field of single and twin circular synthetic air jets. *International Journal of Heat and Fluid Flow*, 44:41–52, 2013.

-
- [38] B.L. Smith and A. Glezer. The formation and the evolution of synthetic jets. *Physics of Fluids*, 10:2281–2297, 1998.
- [39] J.E. Cater and J. Soria. The evolution of round zero-net-mass-flux jets. *J. Fluid Mech.*, 472:167–200, 2002.
- [40] K. Mohseni and R. Mittal. *Synthetic Jets: Fundamentals and Applications*. CRC Press - Taylor & Francis Group LCC, 2015.
- [41] C. L. Rumsey, T. B. Gatski, W. L. Sellers III, V. N. Vatsa, and S. A. Viken. Summary of the 2004 computational fluid dynamics validation workshop on synthetic jets. *AIAA Journal*, 44:194–207, 2006.
- [42] J. Dandois, E. Garnier, and P. Sagaut. Numerical simulation of active separation control by a synthetic jet. *J. Fluid Mech.*, 574:25–58, 2007.
- [43] S. Lardeau and M. A. Leschziner. The interaction of round synthetic jets with a turbulent boundary layer separating from a rounded ramp. *J. Fluid Mech.*, 683:172–211, 2011.
- [44] D.C. McCormick. Boundary layer separation control with directed synthetic jets. In *Proceedings of 38th Aero-space Sciences Meeting and Exhibit, 10-13 January, Reno, Nevada*, pages 1–10, 2000.
- [45] S.A.N Prasad. *Two-Port Electroacoustic Model of Piezoelectric Composite Circular Plate*. M.S. Thesis, 2002.
- [46] Q. Gallas, R. Holman, T. Nishida, B. Carroll, M. Sheplak, and L. Cattafesta III. Lumped element modeling of piezoelectric-driven synthetic jet actuators. *AIAA Journal*, 41:240–247, 2003.
- [47] S.A.N. Prasad, Q. Gallas, , S. Horowitz, and B. Homeijer. Analytical electroacoustic model of a piezoelectric composite circular plate. *AIAA Journal*, 41:240–247, 2006.
- [48] T. Persoons. General reduced-order model to design and operate synthetic jet actuators. *AIAA Journal*, 50:916–927, 2012.
- [49] H. Tang and S. Zhong. Lumped element modelling of synthetic jet actuators. *Aerospace Science and Technology*, 13:331–339, 2009.

- [50] J.S. Agashe, D.P. Arnold, and L.N. Cattafesta III. Development of compact electrodynamic zero-net mass-flux actuators. In *Proceedings of the 47th AIAA Aerospace Sciences Meeting Including The New Horizons Forum and Aerospace Exposition, 5-8 January, Orlando, Florida*, pages 1–19, 2009.
- [51] S.G. Sawant, M. Oyarzun, M. Sheplak, , L.N. Cattafesta III, and Arnold D.P. Modeling of electrodynamic zero-net mass-flux actuators. *AIAA Journal*, 50:1347–1359, 2012.
- [52] Z. Luo, Z. Xia, and B. Liu. New generation of synthetic jet actuators. *AIAA Journal*, 44:2418–2419, 2006.
- [53] S. Arunajatesan, M. Oyarzun, M. Palaviccini, and L.N. Cattafesta III. Modeling of zero-net mass-flux actuators for feedback flow control. In *Proceedings of the 47th AIAA Aerospace Sciences Meeting Including The New Horizons Forum and Aerospace Exposition, 5-8 January, Orlando, Florida*, pages 1–12, 2009.
- [54] R.N. Sharma. Fluid-dynamic-based analytical model for synthetic jet actuation. *AIAA Journal*, 45:1841–1847, 2007.
- [55] L. de Luca, M. Girfoglio, and G. Coppola. Modeling and experimental validation of the frequency response of synthetic jet actuators. *AIAA Journal*, 52:1733–1748, 2014.
- [56] R. Rathnasingham and K.S. Breuer. Coupled fluid-structure characteristics of actuators for flow control. *AIAA Journal*, 35:832–837, 1997.
- [57] L.E. Kinsler, A.R. Frey, A.B. Coppens, and J.V. Sanders. *Fundamentals of acoustics, 4th edition*. Wiley, 2000.
- [58] G. Krishnan and K. Mobseni. Axisymmetric synthetic jets: An experimental and theoretical examination. *AIAA Journal*, 47(10):2273–2283, 2009.

-
- [59] L.D. Gomes, W. J. Crowther, and N.J. Wood. Towards a practical piezoceramic diaphragm based synthetic jet actuator – effect of chamber and orifice depth on actuator peak velocity. In *Proceedings of 3rd AIAA Flow control conference, 5-8 June, San Francisco, California, 2006*.
- [60] L. de Luca, M. Girfoglio, M. Chiatto, and G. Coppola. Scaling properties of resonant cavities driven by pie-zo-electric actuators. *Sensors and Actuators A: Physical*, 247:465–474, 2016.
- [61] S.D. Senturia. *Microsystem Design*. Kluwer Academic Publishers, 2001.
- [62] M. Girfoglio, C.S. Greco, M. Chiatto, and L. de Luca. Modelling of efficiency of synthetic jet actuators. *Sensors and Actuators A: Physical*, 233:512–521, 2015.
- [63] R.J. Moffat. Describing the uncertainties in experimental results. *Experimental Thermal and Fluid Science*, 1(1):3–17, 1988.
- [64] P. Gil and P. Strzelczyk. Performance and efficiency of loudspeaker driven synthetic jet actuator. *Experimental Thermal and Fluid Science*, 76:163–174, 2016.
- [65] G. Kooijman and O. Ouweltjes. Finite difference time domain electroacoustic model for synthetic jet actuators including nonlinear flow resistance. *Journal of the Acoustical Society of America*, 125(4):1911–1918, 2009.
- [66] W. J. Crowther and L.T. Gomes. An evaluation of the mass and power scaling of synthetic jet actuator flow control technology for civil transport aircraft applications. In *Proceedings of Institution of Mechanical Engineer Part I: Systems and Control Engineering*, volume 222, pages 357–372, 2008.
- [67] R. Li, R. Sharma, and M. Arik. Energy conversion efficiency of synthetic jets. In *ASME 2011 Pacific Rim Technical Conference and Exhibition on Packaging and Integration of Electronic and Photonic*

Systems, American Society of Mechanical Engineers. July 6-8, Portland, Oregon, 2011.

- [68] F. Zhao, M.-C. Lai, and D.L. Harrington. Automotive spark-ignited direct-injection gasoline engines. *Progress in Energy and Combustion Science*, 25(5):437–562, 1999.
- [69] M.M. Alhazmy and Y.S.H. Najjar. Augmentation of gas turbine performance using air coolers. *Applied Thermal Engineering*, 24(2-3):415–429, 2004.
- [70] G. Grant, J. Brenton, and D. Drysdale. Fire suppression by water sprays. *Progress in Energy and Combustion Science*, 26(2):79–130, 2000.
- [71] K.P. Sudheer and R.K. Panda. Digital image processing for determining drop sizes from irrigation spray nozzles. *Agricultural Water Management*, 45(2):159–167, 2000.
- [72] A. Hascalik, U. Çaydaş, and H. Gürün. Effect of traverse speed on abrasive waterjet machining of ti-6al-4v alloy. *Materials and Design*, 28(6):1953–1957, 2007.
- [73] C.S. Lee and S.W. Park. An experimental and numerical study on fuel atomization characteristics of high-pressure diesel injection sprays. *Fuel*, 81(18):2417–2423, 2002.
- [74] Byong-Seok Kim, Wook Hyeon Yoon, Sung Hyup Ryu, and Ji Soo Ha. Effect of the injector nozzle hole diameter and number on the spray characteristics and the combustion performance in medium-speed diesel marine engines. Technical report, SAE Technical Paper, 2005.
- [75] P.G. Aleiferis, J. Serras-Pereira, Z. van Romunde, J. Caine, and M. Wirth. Mechanisms of spray formation and combustion from a multi-hole injector with e85 and gasoline. *Combustion and Flame*, 157(4):735–756, 2010.

-
- [76] S. Pothos and E.K. Longmire. Control of a particle-laden jet using a piezo-electric actuator. In *Proceedings of 11th International Symposium on Applications of Laser Techniques to Fluid Mechanics, 8-11 July, Lisbon*, pages 1–12, 2002.
- [77] W Bachalo, E Bachalo, J Hanscom, and S Sankar. An investigation of spray interaction with large-scale eddies. In *31st Aerospace Sciences Meeting*, page 696, 1993.
- [78] Difei Wang, Ahmad Ganji, Chad Sipperley, and Chris Edwards. Effects of nozzle geometry and ambient pressure on the characteristics of a modulated spray. In *37th Aerospace Sciences Meeting and Exhibit*, page 366, 1999.
- [79] V. Sepe. Optical investigation of a water spray controlled by a synthetic jet device. In *Master's Degree Thesis*, 2016.
- [80] A. Palumbo. Effect of a synthetic jet actuator on a continuous water spray behaviour. In *Master's Degree Thesis*, 2016.
- [81] V. Narayanaswamy, L.L. Raja, and N.T. Clemens. Characterization of a high-frequency pulsed-plasma jet actuator for supersonic flow control. *AIAA Journal*, 48(2):297–305, 2010.
- [82] D. Caruana, F. Rogier, G. Dufour, and C. Gleyzes. The plasma synthetic jet actuator. physics. modeling and flow control application and separation. *Journal AerospaceLab*, 06-10:1–13, 2013.
- [83] S. J. Haack, T. Taylor, J. Emhoff, and B. Cybyk. Development of an analytical sparkjet model. In *5th Flow Control Conference. Chicago. Illinois*, pages 1–10, 2010.
- [84] K.V. Anderson and D.D. Knight. Plasma jet for flight control. *AIAA Journal*, 50(9):1855–1872, 2012.
- [85] G. Sary, G. Dufour, F. Rogier, and K. Kourtzanidis. Modeling and parametric study of a plasma synthetic jet for flow control. *AIAA Journal*, 52:1591–1603, 2014.

- [86] F. Laurendeau, F. Chedevergne, and G. Casalis. Transient ejection phase modeling of a plasma synthetic. *Physics of Fluids*, 26:125101, 2014.
- [87] F. Chedevergne, O. Leon, V. Bodoc, and D. Caruana. Experimental and numerical response of a high-reynolds-number $m = 0.6$ jet to a plasma synthetic jet actuator. *International Journal of Heat and Fluid Flow*, 56:1–15, 2015.
- [88] H. Zong, Y. Wu, Y. Li, H. Song, Z. Zhang, and M. Jia. Analytic model and frequency characteristics of plasma synthetic jet actuator. *Physics of Fluids*, 27:1–21, 2015.
- [89] H. Zong, Y. Wu, H. Song, and M. Jia. Efficiency characteristic of plasma synthetic jet actuator driven by pulsed direct-current discharge. *AIAA Journal*, 54(11):3409–3420, 2016.
- [90] B. Z. Cybyk, D. H. Simon, , and H. B. Land. Experimental characterization of a supersonic flow control actuator. In *44th AIAA Aerospace Sciences Meeting and Exhibit*, 2006.
- [91] S.J. Haack, H.B. Land, B. Cybyk, H.S. Ko, and J. Katz. Characterization of a high-speed flow control actuator using digital speckle tomography and piv. In *4th AIAA Flow Control Conference*, 2008.
- [92] T. Emerick, M.Y. Ali, C. Foster, F.S. Alvi, and S. Popkin. Sparkjet characterizations in quiescent and supersonic flowfields. *Experiments in Fluids*, 55(12):1–21, 2014.
- [93] V. Narayanaswamy, L.L. Raja, and N.T. Clemens. Control of unsteadiness of a shock wave/turbulent boundary layer interaction by using a pulsed-plasma-jet actuator. *Physics of Fluids*, 24(7), 2012.
- [94] T.M. Reedy, N.V. Kale, J.C. Dutton, and G.S. Elliott. Experimental characterization of a pulsed plasma jet. *AIAA Journal*, 51(8):2027–2031, 2013.
- [95] A. Belinger, P. Hardy, P. Barricau, J. P. Cambronner, and D. Caruana. Influence of the energy dissipation rate in the discharge of a plasma

- synthetic jet actuator. *Journal of Physics D: Applied Physics*, 44:1–12, 2011.
- [96] A. Belinger, N. Naudé, J. P. Cambronne, and D. Caruana. Plasma synthetic jet actuator electrical and optical analysis of the discharge. *Journal of Physics D: Applied Physics*, 47:1–11, 2014.
- [97] H.-H. Zong, W. Cui, Y. Wu, Z.-B. Zhang, H. Liang, M. Jia, and Y.-H. Li. Influence of capacitor energy on performance of a three-electrode plasma synthetic jet actuator. *Sensors and Actuators, A: Physical*, 222:114–121, 2015.
- [98] H.-H. Zong, Y. Wu, M. Jia, H.-M. Song, H. Liang, Y.-H. Li, and Z.-B. Zhang. Influence of geometrical parameters on performance of plasma synthetic jet actuator. *Journal of Physics D: Applied Physics*, 49(2), 2015.
- [99] Z. Zhang, Y. Wu, M. Jia, H. Zong, W. Cui, H. Liang, and Y. Li. Influence of the discharge location on the performance of a three-electrode plasma synthetic jet actuator. *Sensors and Actuators, A: Physical*, 235:71–79, 2015.
- [100] M. Chiatto and L. de Luca. Numerical and experimental frequency response of plasma synthetic jet actuators. *AIAA Paper, AIAA 2017-1884*, pages 1–16, 2017.
- [101] G. Dufour, P. Hardy, G. Quint, and F. Rogier. Physics and models for plasma synthetic jets. *International Journal of Aerodynamics*, 3:47–70, 2013.
- [102] M. Capitelli, G. Colonna, C. Gorse, and A. D’Angola. Transport properties of high temperature air in local thermodynamic equilibrium. *The European Physical Journal D*, 11:279–289, 2010.
- [103] S.H. Popkin, B.Z. Cybyk, C.H. Foster, and F.S. Alvi. Experimental estimation of sparkjet efficiency. *AIAA Journal*, 54(6):1831–1845, 2016.

- [104] OPENFOAM, The open source CFD Toolbox. *User Guide*. OPENFOAM Foundation, 2012.
- [105] OPENFOAM, The open source CFD Toolbox. *Programmer's Guide*. OPENFOAM Foundation, 2013.
- [106] D. Caruana, P. Barricau, P. Hardy, J.P. Cambronner, and A. Belinger. The "plasma synthetic jet" actuator. aero-thermodynamic characterization and first flow control applications. In *47th AIAA Aerospace Sciences Meeting including the New Horizons Forum and Aerospace Exposition*, 2009.
- [107] *One-Dimensional Analytical Model Development of a Plasma-based Actuator*, 2014. University of Maryland.
- [108] A. Fridman, A. Chirokov, and A. Gutsol. Non-thermal atmospheric pressure discharges. *Journal of Physics D: Applied Physics*, 38(2):R1–R24, 2005.
- [109] M. Barker. On the use of very small pitot-tubes for measuring wind velocity. *Proceedings of the Royal Society A*, 101:435–445, 1922.
- [110] F. Homann. Effect of high viscosity on the flow around a cylinder and around a sphere. Technical report, NACA, 1952. Technical Memorandum 1334.
- [111] S.K.S. Boetcher and E.M. Sparrow. Limitations of the standard bernoulli equation method for evaluating pitot/impact tube data. *International Journal of Heat and Mass Transfer*, 50(3-4):782–788, 2007.
- [112] F.E. Jørgensen. *How to measure turbulence with hot-wire anemometers - a practical guide*. Dantec Dynamics, 2002.

Acknowledgments

Once again I find myself to thank all the people who helped and supported me during an important period of my life.

I would like to express my gratitude to Prof. Luigi de Luca for giving me the opportunity to undertake this adventure, choosing the working topic perfectly in tune with my skills.

Thanks to all the Professors of the X floor, for their wide willingness and sincere interest. I really appreciated the advices of Professor Carlomagno and the time spent with Tommaso and Gennaro.

Thanks to all my new friends, met during this period, for making days easier. Each of you has provided an important piece to complete this path. I will never forget the moments spent together at the X floor and in the laboratory.

Thanks to my family. Thanks to my father Giannino, my mother Pina e my sister Miriam. You have always supported me in any way in all my decisions.

Thanks to my beloved Margherita. In my times of need, I had you there to steer me in the right direction and to support me with all your strength. I am so lucky to have you by my side.